The Dissertation Committee for Suyong Jung
certifies that this is the approved version of the following dissertation:

Spin and Charge Transport through Carbon Based Systems

Committee:

Zhen Yao, Supervisor

Alejandro de Lozanne

Allan H. MacDonald

Maxim Tsoi

Li Shi

Spin and Charge Transport through Carbon Based Systems

by

Suyong Jung, B.S.

Dissertation

Presented to the Faculty of the Graduate School of

The University of Texas at Austin

in Partial Fulfillment

of the Requirements

for the Degree of

Doctor of Philosophy

The University of Texas at Austin

August 2007

To my beloved family

Acknowledgments

I believe that my Ph. D. work has never been realized without the help and encouragements from others for the past six years in Austin. I would like to acknowledge many people, whom I have met in my Ph. D journey here. Most of all, I would like to appreciate my thesis advisor Dr. Zhen Yao. I thank him for offering me a chance to see and experience how experimental work can be realized. I am also indebted to him for his impartial opinions on the past and ongoing discussions. His advice and guidance have been a driving force to continue my Ph. D studies. I would like to thank Prof. Mahn-Soo Choi for his immeasurable supports. I wish to thank Prof. Allan H. MacDonald, Prof. Alex de Lozanne, Prof. Maxim Tsoi and Prof. Li Shi for serving on my thesis committee. I would like to thank Kang Luo and Dong-Hun Chae for sailing together through the last five years in the name of Dr. Yao group members. I would like to express gratitude to many other colleagues and friends who share with me the most exciting time in my life here in Austin. Finally, I want to say to my father, mother, brother, father-in-law, mother-in-law and my wife, Jiyoun that I love you all very much. Without your loves and supports, there would not be me after all.

Suyong Jung

The University of Texas at Austin
August 2007

Spin and Charge Transport through Carbon Based Systems

Publication No. ______________________

Suyong Jung, Ph.D.
The University of Texas at Austin, 2007

Supervisor: Zhen Yao

In this thesis, we investigate spin-dependent transport through ferromagnet-contacted single-walled carbon nanotubes (SWCNTs), in which charge transport shows the Fabry-Perot (FP) interference effect, the Kondo effect and the Coulomb blockade effect at low temperatures. Hysteric magnetoresistance (MR) is observed in all three transport regimes, which can be controlled by both the external magnetic field and the gate voltage. The MR in the FP interference regime can be well understood by a model considering the intrinsic electronic structure of SWCNTs and the quantum interference effect. In the strongly interacting Kondo regime, the Kondo effect is not suppressed by the presence of nearby ferromagnetism. Several observed MR features including the non-splitted zero-bias Kondo peak and positive MR switching can be explained by the strong Kondo effect and weak ferromagnetism in the leads. In the Coulomb blockade regime, several effects that can be associated with the magneto-Coulomb effect have been observed, and isolated spin accumulation and transport through the SWCNT quantum dot have been realized by a four-probe non-local measurements.

We also studied charge transport behavior through organic semiconductor pentacene thin film transistors (OTFTs) in the limit of single- or a few molecular layers of pentacene films. The charge transport in these devices can be well explained by the multiple trapping and release model. The structural disorders induced by the physical and chemical causes, such as grain boundaries, interactions with gate insulator, metal contacts and ambient conditions can be responsible for the localized trap states in the ultrathin layer OTFTs, which are further confirmed by the electric force microscopy (EFM) measurements.

Contents

List of Tables

List of Figures

Chapter 1

Introduction

1.1 Motivation

In modern electronics, the controllability of electron charges has reached where only thousands or hundreds of them are considered as a basic unit of device information. Even more, researchers can now willingly manipulate single electron charges in highly correlated condensed matter systems. Because of the minuscule scale that modern technologies and science handle, understanding electron behavior in those systems needs the information of quantum physics, since electron charge quantization and the interactions between electrons simply cannot be ignored. As for the other side of electron charges, electron spins have also been intensively investigated, and successfully utilized in modern technologies, especially in data storage. Therefore, it is quite natural that there has been tremendous interest in spin-dependnet electronics, often referred to "spintronics", in which the coupling between electron charges and spins is exploited for information storage and communication [1]. Similar to electronic devices, the spintronic devices are following the same pace of miniaturization. Thus investigating spin-dependent transport in mesoscopic or nanoscale structures is of particular importance.

Among several candidates for studying spin-dependent transport behavior, carbon-based materials, especially single-walled carbon nanotubes (SWCNTs) have been known for one of the promising candidates. Firstly, electron spins are expected to transport through SWCNTs without losing spin-coherence by spin-dephasing effect such as spin-orbit coupling. Secondly, electronic transports in metallic SWCNTs are ballistic. Lastly, SWCNTs are so far the cleanest conductors, in which electronic properties of SWCNTs are well established by various quantum transport phenomena [2]. Surprisingly, however, spin-dependent transport in this system has remained largely unexplored [3, 4].

Here we will discuss experimental studies of spin transport in ferromagnet-contacted SWCNTs, which exhibit several interesting quantum transport phenomena, such as the Fabry-Perot interference effect, the Kondo effect, and the Coulomb blockade effect. Ferromagnetic electrodes are utilized to generate and detect spin information, and both a gate electrode and an external magnetic field are used to control spin transport in SWCNTs. It has been found that spin-dependent transport in SWCNTs is highly correlated with the corresponding charge transport behavior.

We will also discuss the charge transport behavior in another carbon-based system, organic semiconductors, in the second part of the thesis. The charge transport through organic semiconductor is studied to address the key elements in deciding the charge flows in the organic thin film transistors (OTFTs). In OTFTs, most charged carriers are limited to a few organic molecular layers near the organic-gate insulator interface [5, 6]. Thus a few layers of organic pentacene films are explored as the ideal system to understand the effects of the interactions of organic materials with gate insulating layer as well as ambient conditions, grain boundaries, and metal contacts. Electric force microscopy has also been performed to complement the charge transport measurements.

1.2 Thesis Outline

This thesis is mainly comprised of two parts. The first part of this thesis is dedicated to spin transport study through an individual SWCNT, and the second to charge transport study through ultrathin organic semiconductor pentance films.

In Chapter 2, we will present the basic charge transport behavior in SWCNTs at low temperatures, and the basic concepts of spin-dependent transport and spin field-effect transistors. Previous efforts on the realization of spin transport through SWCNTs are also presented. In Chapter 3, the experimental details on the fabrication of ferromagnet-contacted SWCNTs devices will be described.

The magnetoresistance observed in these devices will be discussed in Chapter 4 for the Fabry-Perot interference regime, and Chapter 5 for the Kondo regime. The magneto-Coulomb effect in two-probe SWCNT spin devices will be discussed in Chapter 6, and the non-local spin transport through a SWCNT quantum dot in the Coulomb blockade regime will be presented in Chapter 7.

The basic concepts of organic field-effect transistors and the experimental realizations of ultrathin pentacene field-effect transistors will be presented in Chapter 8 and Chapter 9, respectively. Charge transport through single- and double-layer pentacene OTFTs will be presented in Chapter 10, and the direct observation of charge transport through OTFTs with an EFM will be presented in Chapter 11. This thesis will be closed with a brief summary in Chapter 12.

Chapter 2

Introduction to Charge and Spin Transport through Single-Walled Carbon Nanotubes

2.1 Carbon Nanoutbes

Background for carbon nanotubes

In 1991, Iijima discovered a new form of carbon atoms [7], whose structure was composed of several coaxial tubes of graphite sheet displaying a needlelike one-dimensional structure, as shown in the transmission electron microscopy (TEM) image of Fig. 2.1 (a). Because of its multiple shell structure, this form of carbon was referred to as multi-walled carbon nanotubes (MWCNTs). Single-walled carbon nanotubes (SWCNTs) were later discovered by Iijima *et al.* [8] and Bethune *et al.* [9], independently in 1993. Figure 2.1 (b) shows a representative TEM image of a SWCNT.

Because of the strong covalent bonds between constituent carbon atoms, carbon nanotubes show extraordinary mechanical properties. For instance, the Young's

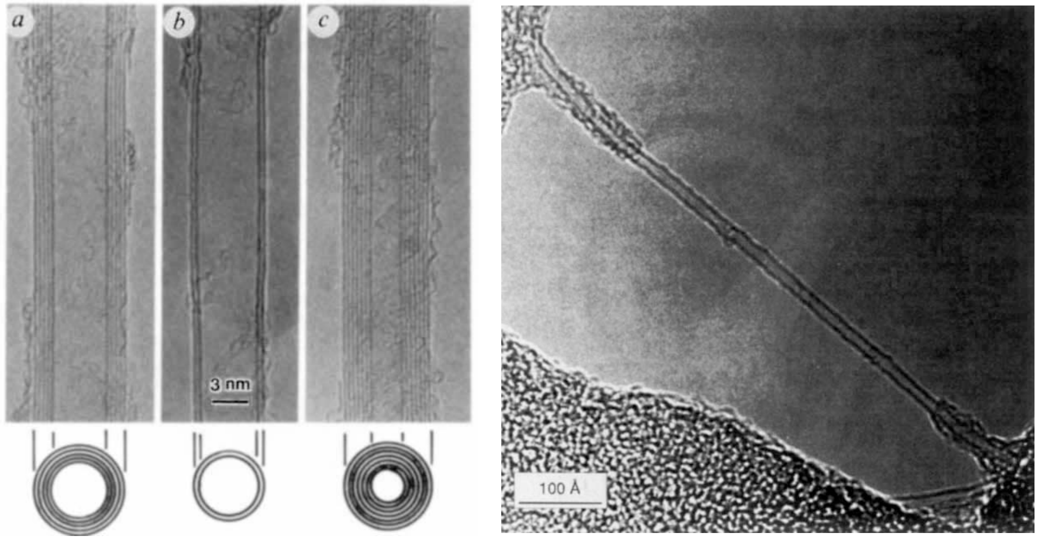

Figure 2.1: TEM images of multi-walled and single-walled carbon nanotubes. (from Ref. [7, 9])

modulus of carbon nanotubes is estimated to be ~ 1 TPa [10], two orders of magnitude higher than the most hardened steel. In addition, SWCNTs also exhibit exceptional electronic properties. From band structure calculations, SWCNTs are expected to show either metallic or semiconducting behavior, depending on their atomic structure [11]. Electrons traveling through metallic SWCNTs show ballistic behavior, and the Luttinger liquid feature in one-dimensional system due to electron-electron interactions has been observed [12]. In addition, SWCNTs with additional constrictions by the metal contacts show zero-dimensional quantum dot (QD) behavior at low temperatures.

Considering their exotic mechanical and electronic properties, it is not difficult to imagine there has been intensive research into possible applications of carbon nanotubes. For instance, carbon nanotubes have been used in field-emission displays [13], chemical and biological sensors [14, 15], lithium batteries [16] and nanotweezers [17]. Furthermore, field-effect transistor (FET) effect was observed in semiconduct-

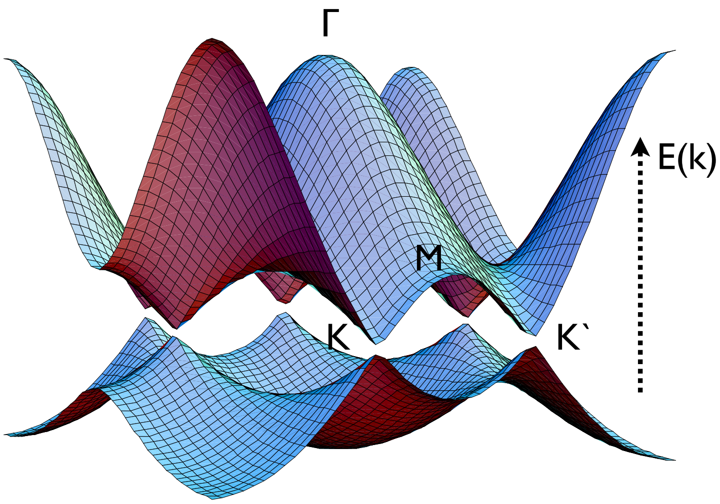

Figure 2.2: The band structure of graphene. The Fermi-energy level is located at the six degeneracy points (K, K′) where valence and conduction bands meet.

ing carbon nanotubes [18], and the mobility has been found to be exceedingly high compared to conventional silicon-based transistors [19]. In addition, several fascinating geometric combinations of FETs have been explored, such as p-n [20] and p-n-p junctions [21]. The rectifying behavior is also manifested in nanotube-nanotube molecular junctions [22].

Electronic structure of single-walled carbon nanotubes

In this thesis, we focus on the spin-dependent transport behavior observed in ferromagnet-contacted SWCNTs. The spin transport through SWCNTs is found to be highly correlated with its corresponding charge transport behavior. Therefore, it is necessary to understand the charge transport through SWCNTs first. The electronic structure of carbon nanotubes is based on the electronic structure of graphene. In essence, one can obtain the band structure of SWCNTs by taking the dispersion relation of the graphene, and imposing a boundary condition around the circumfer-

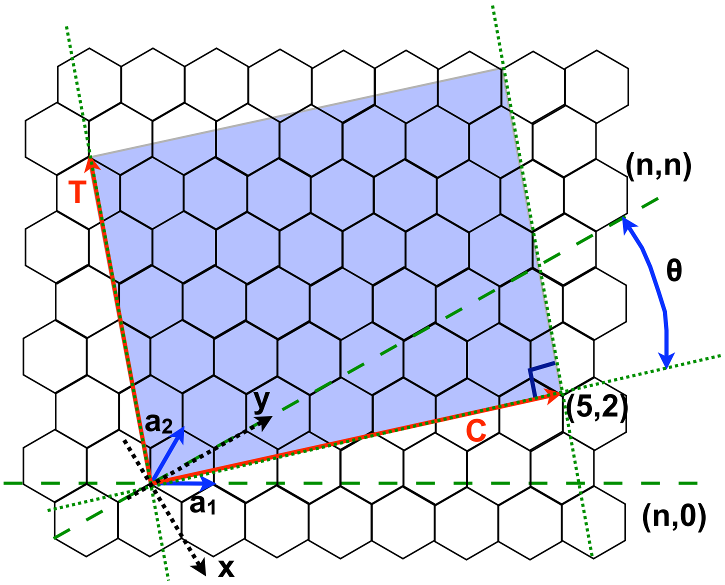

Figure 2.3: A schematic diagram for the construction of SWCNTs out of a two-dimensional graphene sheet.

ence.

The energy dispersion relation of the graphene sheet calculated from the tight-binding approximation is plotted in Fig. 2.2 [23]. The upper half of the energy band is referred to as π^*-bonding (anti-bonding) and the lower half is called π-bonding (bonding band). Since there are two π electrons per graphene unit cell, the lower half π-bonding is fully occupied, and the other π^*-bonding is completely unoccupied at zero temperature. Since there is no available density of states at the Fermi energy, the two-dimensional graphene is expected to be semi-metallic.

SWCNTs are formed by rolling up the graphene sheet into a seamless cylinder, as illustrated in Fig. 2.3 [24, 25]. The direction in which the graphene sheet is rolled is determined by the chiral vector $\mathbf{C}$, which can written by a linear combination of graphene unit vectors $\mathbf{a}_1$ and $\mathbf{a}_2$, i.e., $\mathbf{C} = n\mathbf{a}_1 + m\mathbf{a}_2$, where n and m are integers. Basically, $\mathbf{C}$ defines two lattice points that are connected when the

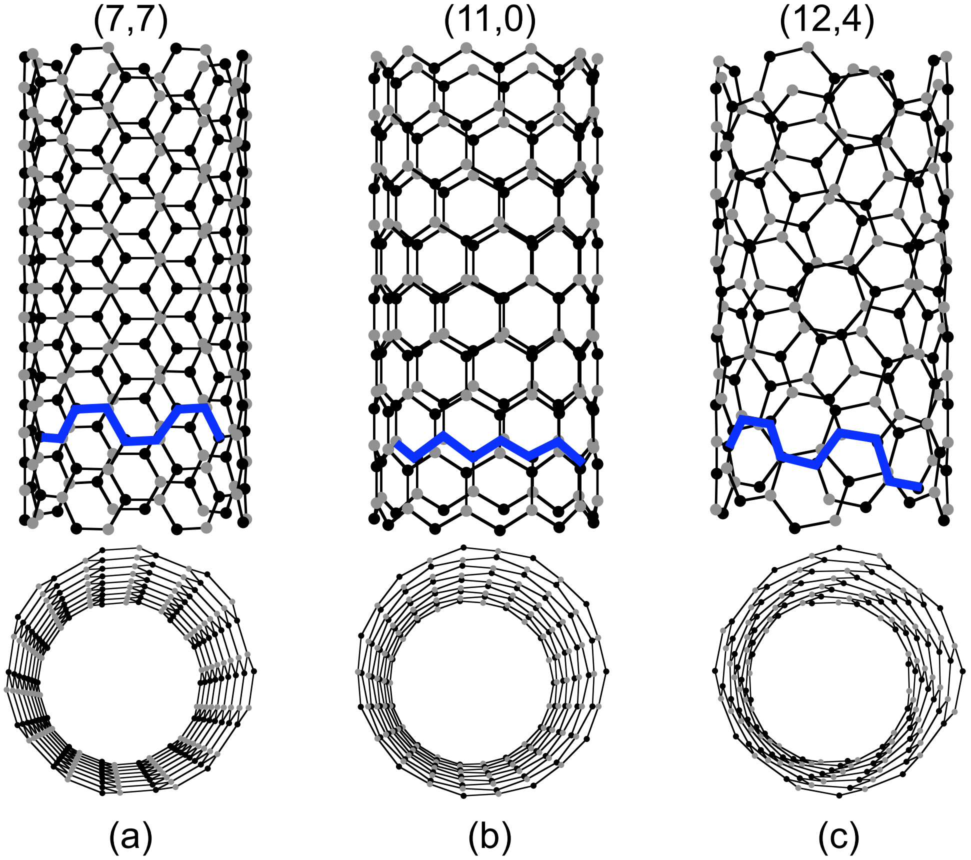

Figure 2.4: The structure of (a) (7,7) armchair, (b) (11,0) ziazag, and (c) (12,4) chiral SWCNTs.

graphene sheet is rolled into a tube. The resultant nanotube is referred as an (n,m) SWCNT. Geometrically, three types of SWCNTs are possible: (i) armchair, (ii) zigzag and (iii) chiral tubes. SWCNTs formed by the tube indices (n,n) and $\theta = 30^\circ$ are called armchair tubes. When the tube index is (n,0) and $\theta = 0^\circ$, the SWCNTs are called zigzag tubes. SWCNTs other than armchair and zigzag tubes are called chiral tubes. Therefore, the angle for chiral tubes is in the range of $0^\circ < \theta < 30^\circ$. Examples of the structures of the three different kinds of SWCNTs viewed from the top and side are displayed in Fig. 2.4.

The electronic band structure of SWCNTs can be calculated from the disper-

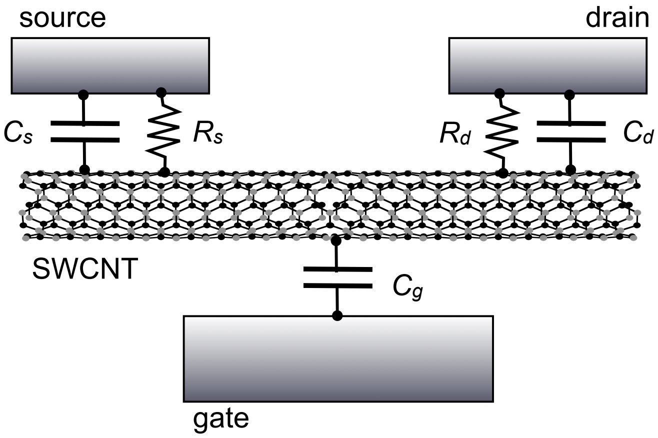

Figure 2.5: Schematic diagram of the three-probe SWCNT transistor.

sion relation of the two-dimensional graphene sheet by imposing a periodic boundary condition. It has been well known that SWCNTs can be categorized into metallic or semiconducting tubes depending on whether the allowed wave vectors cross the degeneracy points (K,K′) in the band diagram of graphene. If the SWCNT indices (n,m) satisfying $n - m = 3j$, where j is an integer, the SWCNT is expected be metallic. The SWCNTs satisfying $n - m \neq 3j$ are expected to show semiconducting behavior. For example, among the SWCNTs illustrated in Fig. 2.4, (7,7) armchair tube is metallic, and both zigzag (11,0) and chiral (12,4) tubes are semiconducting. Basically all armchair SWCNTs are metallic, and some of zigzag and chiral SWCNTs are metallic and others are semiconducting tubes.

2.2 Charge Transport in Single-Walled Carbon Nanotubes

In order to explore charge transport properties through SWCNTs, a conventional three-probe transistor geometry including source, drain, and gate electrodes has been commonly utilized, where the electronic states in SWCNTs can be controlled through capacitive coupling by the gate electrode, as shown in Fig. 2.5. By controlling the gate and bias voltages, and monitoring the current through the SWCNT, we can observe several interesting quantum electronic transport properties of SWCNTs, such as single electron charging effect [26], quantum interference effect [27], and Kondo physics [28].

In our spin-dependent transport measurements, we have also adopted the three-probe geometry. Since we are interested in spin transport through SWCNTs, source and drain electrodes are made out of ferromagnetic films to manipulate electron spins. Even though source and drain electrodes are fabricated with ferromagnetic electrodes, the charge transport through SWCNTs is similar to that in normal metal contacted SWCNT devices [4, 29]. As mentioned before, the spin-dependent transport through SWCNTs cannot be understood without the knowledge of charge transport mechanism in SWCNTs. Thus, we will briefly discuss several charge transport behaviors observed in SWCNT devices in the following sections.

2.2.1 Charge Transport at Low Temperature

At low temperature, Coulomb charging is dominating the charge transport in SWCNTs. The Coulomb charging energy to add one additional electron is determined by the total capacitance of the SWCNT device, $C_\Sigma = C_s + C_d + C_g$, where $E_c = e^2/C_\Sigma$. Here the C_s and C_d are capacitances of the source and drain electrodes to the SWCNT, and C_g is the gate electrode capacitance. The number of electrons in the SWCNT device remains unchanged, unless additional energy which is greater than E_c is supplied to the system, and this phenomenon is called the Coulomb blockade.

In order to observe the Coulomb charging effect, the charging energy E_c should be greater than the thermal energy k_BT, otherwise, thermally excited electrons can move into and out of the SWCNT device freely. Additional condition for observing the Coulomb blockade effect can be obtained from the energy uncertainty relationship, i.e., $\Delta E \cdot \Delta t > h$, where $\Delta E \sim e^2/C_\Sigma$, and Δt is the time for electrons to transfer into and out of the QDs, $\Delta t \sim R_t C_\Sigma$. Thus, the tunneling resistance R_t should satisfy the following condition in order for electrons to be well defined in the SWCNT devices :

$$\frac{e^2}{C_\Sigma} \cdot R_t C_\Sigma > h \quad \longrightarrow \quad R_t > \frac{h}{e^2} = R_Q = 25.8\ \mathrm{k\Omega}. \tag{2.1}$$

R_t is measured as the contact resistance of the SWCNT devices. Thus in the regime where $E_c > k_B T$ and $R_t > R_Q$, the charge transport through the SWCNT is controlled by the Coulomb blockade effect.

In SWCNT devices, the source and drain metal contacts often impose an additional constriction on the electronic structure of the SWCNT. The wave vector k along the longitudinal axis is determined by the boundary condition $kL = i\pi$, where i is an integer, and L is the length of SWCNT segment. Accordingly, there are additional quantized energy states in the SWCNTs energy bands, and the spacing between the levels, ΔE, is approximated by [23]

$$\Delta E \approx \left[\frac{\partial E(k)}{\partial k}\right]_{E=E_F} \frac{\Delta k}{2} \approx \frac{h v_F}{4L} \approx \frac{1\ \mathrm{meV}}{L\ \mu\mathrm{m}}, \tag{2.2}$$

where $v_F = 8.0 \times 10^5$ m/s is the Fermi-velocity in carbon nanotubes, and h is the Plank constant. The factor of two comes from the $K - K'$ orbital degeneracy in metallic SWCNT. When the orbital degeneracy is lifted, ΔE is increased by a factor of two, $\Delta E = h v_F/2L$. These discrete quantized energy states of the SWCNTs are reminiscent of those in zero-dimensional quantum dot (QD) structures. Thus, SWCNTs with finite length L behave like QDs at sufficiently low temperatures [26].

2.2.2 Coulomb Blockade Effect

Basic Concepts and Theories

When the metal contacts to SWCNT QDs are opaque enough, the first-order sequential tunneling becomes the dominant charge transport mechanism, and the transport through the SWCNT QD is determined by the Coulomb charging energy, E_c, and the electronic energy level spacing of the SWCNT, ΔE.

When N electrons reside in the QD, the total Coulomb energy is $U(N) = \sum_{i=1}^{N} E_i + (Ne)^2/2C_{\sum}$, where, E_i is the highest chemical potential of the quantized energy levels of the QDs when i electrons fill the dot. After an additional electron is added to the QD, the energy increases to $U(N+1) = \sum_{i=1}^{N+1} E_i + \big((N+1)e\big)^2/2C_{\sum}$. From these, we can define the electrochemical potential of the QD :

$$\mu_N = U(N) - U(N-1) = E_N + \frac{e^2}{C_{\sum}}\left(N - \frac{1}{2}\right) - eV_{dot}. \tag{2.3}$$

The electrochemical potential μ_N is the minimum energy required to add an N-*th* electron to the QD, and the additional term eV_{dot}, which accounts for the capacitive couplings of the source, drain and gate electrodes to the QD, is added. In all of our measurements, the drain electrode is grounded, so V_{dot} can be expressed by a function of gate and bias (source) voltages :

$$V_{dot} = \frac{1}{C_{\sum}}\left(C_s V_s + C_d V_d + C_g V_g\right) = \frac{C_s}{C_{\sum}} V_s + \frac{C_g}{C_{\sum}} V_g, \tag{2.4}$$

As shown in Fig. 2.6 (a), the electron can flow (on-state) through the QD as long as μ_N is in the window of $eV_S = \mu_d - \mu_s$. Under this condition, the number of electrons on the dot is alternating between $N-1$ and N. However, if μ_{N+1} is higher than μ_d, and μ_N is lower than μ_s, there are no available states for electrons to tunnel into. In this case, the current through the QD is blocked (off-state), and

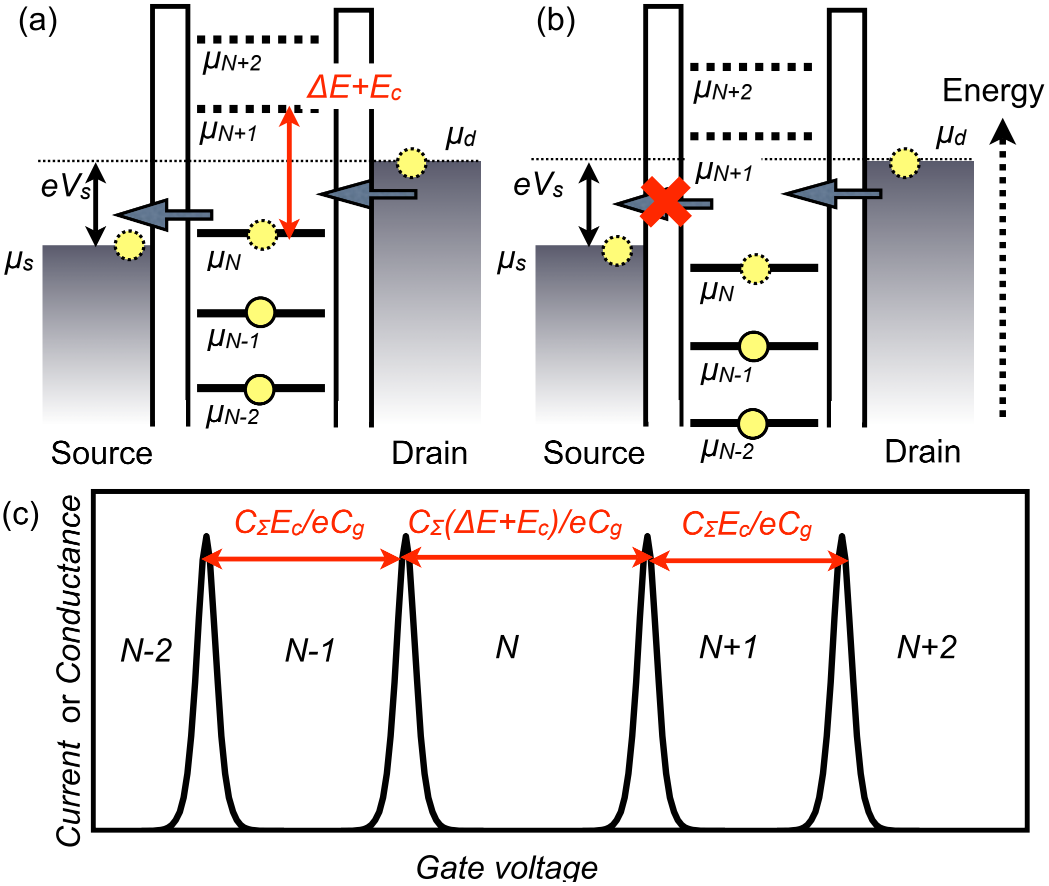

Figure 2.6: Electron transport in a SWCNT QD. (a) The electron number in the dot is oscillating between N and $N-1$ (on-state) (b) The electron number in the dot is fixed at N (off-state), and the current is blocked. (c) The current or conductance oscillation as a function of gate voltage. The four consecutive Coulomb oscillations are labeled with the number of electrons in the dot.

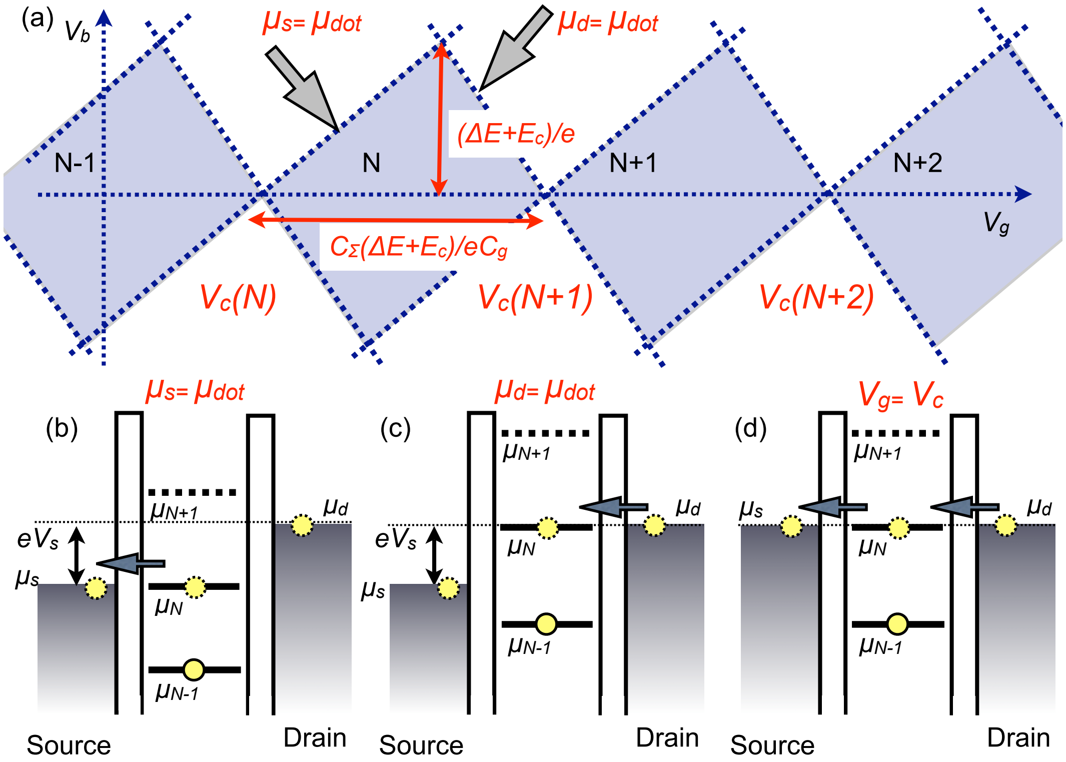

Figure 2.7: (a) A schematic diagram of the two-dimensioal current or conductance mapping as a function of bias and gate voltages. The regimes where the current is blocked are marked by a blue shaded area, and the number of electrons is labeled in Coulomb diamonds. The energy diagrams depicting when the current starts flowing (b) at $\mu_s = \mu_{dot}$, (c) $\mu_d = \mu_{dot}$, and (d) $\mu_s = \mu_d = \mu_{dot}$.

the number of electrons in the QD is fixed at N.

One of the characteristic features of the Coulomb blockade effect in current-voltage ($I - V$) measurements is the Coulomb oscillations, as shown in Fig. 2.6 (c). In a small bias voltage, $eV_s \simeq 0$ V, μ_N is controlled by the gate voltage. When the μ_N is aligned to the Fermi level of the source and drain electrodes ($\mu_s = \mu_d \simeq 0$), the current is flowing through the QD. In case that μ_N is not aligned to $\mu_s = \mu_d \simeq 0$, the current is blocked. Thus, the on- and off-state is alternating as varying the gate voltage, and the spacing between adjacent Coulomb peaks is determined by the quantum energy level of the QD, ΔE, and Coulomb charging energy, E_c. Note that ΔE can be zero, when two consecutive electrons are added to the same spin-dengerate level or if there are additional degeneracies present. Since every electrons added to the QD is required E_c, the ΔE and E_c can be separated by monitoring several consecutive Coulomb oscillations.

The Coulomb blockade effect can be also manifested as diamond shaped features in the two-dimensional differential conductance plot as varying both the bias and gate voltages, as illustrated in Fig. 2.7 (a). The region where the current is blocked is indicated by the blue shaded areas, and the boundaries where the current starts to flow are marked with blue dotted lines. Once the chemical potential of the dot is aligned to that of one of electrodes, as illustrated in Fig. 2.7 (b) and (c), current starts flowing. After simple derivation, we can obtain the source and gate voltage relations for the boundaries of the Coulomb blockade diamonds :

$$\begin{aligned} V_s &= \frac{C_g}{C_g + C_d}\left(V_g - V_c(N)\right) \quad , \quad (\mu_d = \mu_{dot}) \\ V_s &= -\frac{C_g}{C_s}\left(V_g - V_c(N)\right) \quad , \quad (\mu_s = \mu_{dot}), \end{aligned} \tag{2.5}$$

where $V_c(N)$ is the gate voltage where the degeneracy point meets at zero bias $V_s = 0$. Figures 2.7 (b) and (c) illustrate the cases of $\mu_s = \mu_{dot}$ and $\mu_d = \mu_{dot}$, respectively. From the calculated slopes for each case, we can determine the capacitance ratio of the QD. In addition, the bias voltage at which two linear graphs as described by Eq. (2.5) intersect, is related to the ΔE and E_c.

2.2.3 Kondo Effect

Charge transport in the Coulomb blockade regime is based on the sequential tunneling mechanism as shown in the previous section. This first order tunneling event is only allowed when the chemical potential of the dot, μ_N, is between those of the

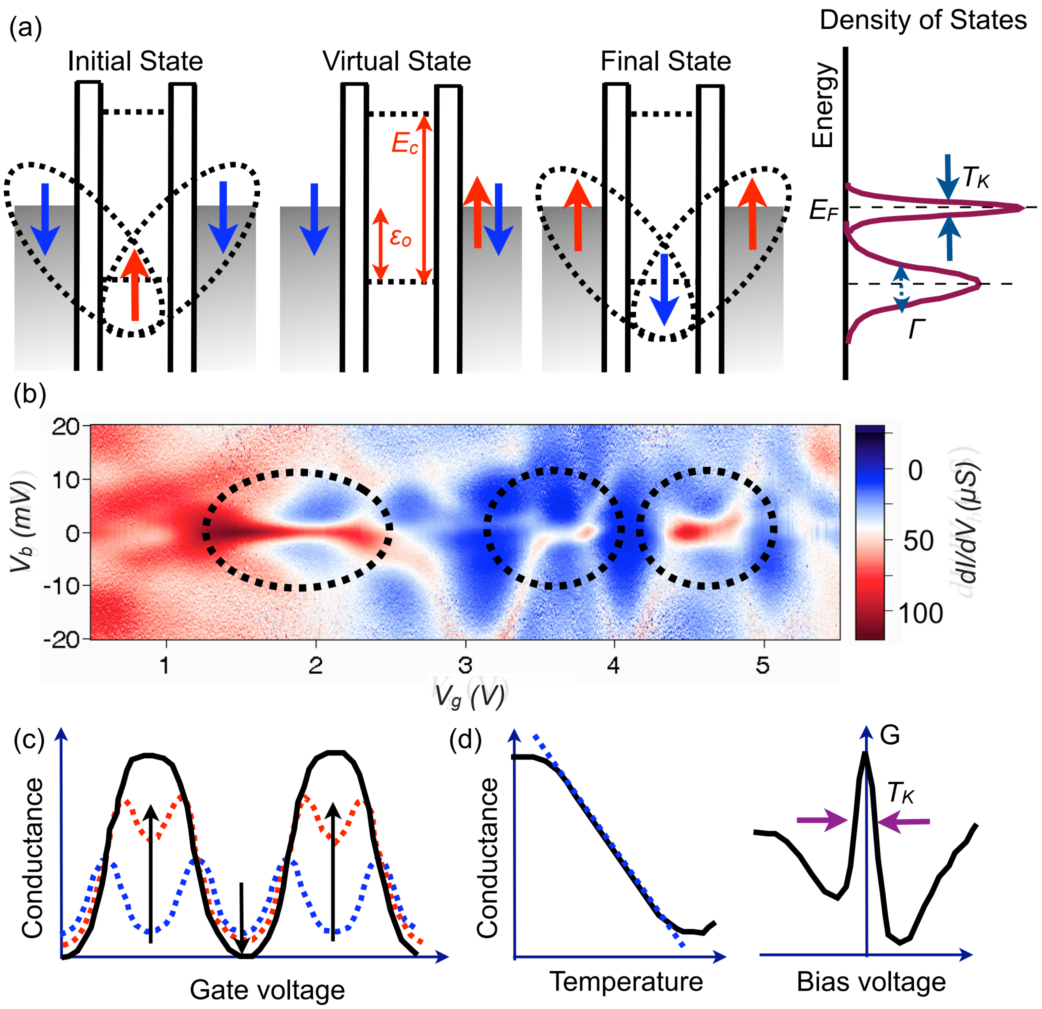

Figure 2.8: Kondo effects in a QD. (a) The spin-exchanged charge transport results in the additional density of states aligned to the Fermi energy of the metal electrodes. (b) Two-dimensional conductance plot showing the zero bias Kondo resonance peaks inside the Coulomb blocakde regions. (c) Conductance oscillations as a function of gate voltage without (dotted blue line) and with Kondo effect (solid black line). (d) Conductance as a function of temperature. (e) Kondo resonance as a function of bias voltage.

source and drain electrodes. This description is quite accurate for the QDs with high contact resistance ($R_t \gg R_Q$). When the contact resistance R_t is comparable to quantum resistance R_Q, however, the strength of the Coulomb blockade effect diminishes and higher tunneling events emerge, which causes quantum fluctuations of electrons in the dot. Among various higher order tunneling events, the Kondo effect is one of the most acknowledged and studied quantum transport phenomena in zero-demensional QD systems.

Because of the higher order tunneling processes, the unpaired spin-up electron in the QD can tunnel off to the metal electrodes, leaving the dot energetically unfavorable 'virtual' state for a short time. This is allowed by virtue of Heisenberg's energy-time uncertainty principle, as long as another electron tunnels into the dot within the time scale $\Delta t \sim h/E$. Thus, the vacant state in the QD is immediately filled with the spin-down electron, and the net spin of the QD is reversed accordingly. In this process, the spin on the dot and the conduction electron spins in the metal electrodes are no longer separated, and they form a coherently entangled spin-singlet state. Because of this spin-flip process, additional density of states is formed at the Fermi energy of the metal electrodes. The Kondo effect can be characterized by a single parameter, the Kondo temperature T_K, which indicates the strength of the Kondo effect [30] :

$$T_K = \sqrt{E_c \Gamma} e^{-\pi \epsilon_o (E_c - \epsilon_o)/2\Gamma E_c}. \tag{2.6}$$

Here, Γ is the tunneling rate to and from the QD and is often referred to as the bare electrode coupling, and ϵ_o is the energy level from the Fermi energy of the metal electrodes.

The main Kondo features observed in the QDs are presented in Fig. 2.8. Because of the higher-order tunneling properties of the Kondo effect, current flow within the Coulomb blockade region is allowed, which is manifested as peaks in conductance at zero bias, $V_b = 0$. Figure 2.8 (b) shows the two-dimensional conductance plot as a function of bias and gate voltages, which shows three Kondo resonance lines. The Kondo resonances are usually seen in every other Coulomb blockade regions, as shown in Fig. 2.8 (b) and (c), because the unpaired electron in the QD is necessary to form a spin-singlet state with conducting electrons in the metal reservoirs. When an additional electron is added to the dot, however, it is paired with the electron in the dot, which makes the total spin of the dot $S = 0$. Therefore, the Kondo effect is not expected when the number of electrons in the QD is even.

The splitting of the resonance peak under an external magnetic field is another signature of the Kondo effect. Because of the Zeeman effect, the Kondo resonance peak is expected to split into two by $2g\mu_B B/e$. Here, g is the Lande g-factor, μ_B is the Bohr magneton and B is the external magnetic field.

Conductance enhancement due to the Kondo effect increases with decreasing temperature, and eventually saturates to the quantum of conductance, $2e^2/h$. Figure 2.8 (d) illustrates the conductance plot as a function of temperature on a logarithmic scale, which can be fitted to an empirical expression [31] :

$$G(T) = G_o \left(1 + (2^{-s} - 1)(T/T_K)^2\right)^{-s}, \tag{2.7}$$

where s is an asymptotic value equal to 0.22 for a spin $\frac{1}{2}$ system. The Kondo temperature, T_K, can be obtained from the fitting of experimental data measured at different temperatures to Eq. (2.7). In addition, T_K can also be estimated from the full width at half maximum (FWHM) of the Kondo resonance peak by FWHM $\approx 2k_B T_K/e$ [30].

The Kondo effects discussed above are expected in normal-metal-contacted QDs. However, it is expected that Kondo effect will be influenced by the nearby ferromagnetism [32, 33, 34]. Since the density states of the conducting electrons in

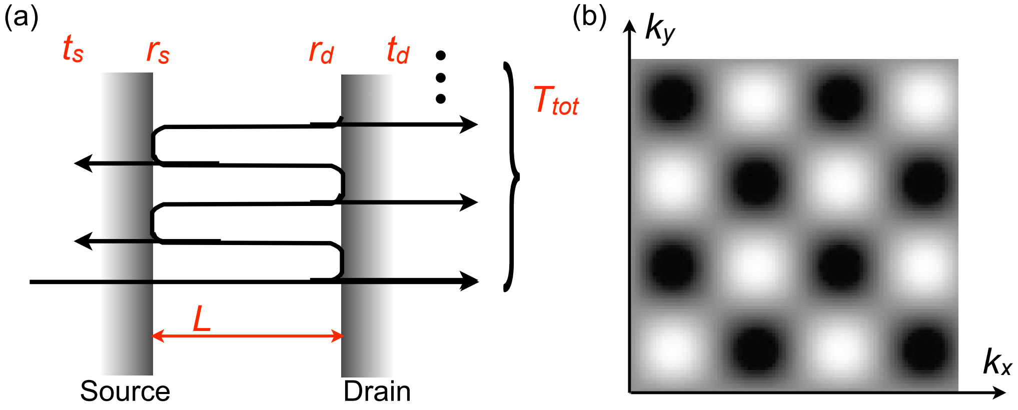

Figure 2.9: (a) Schematic diagram of a FP resonator. The transmission and reflection coefficients are denoted with $t_{s,d}$ and $r_{s,d}$ at each electrode. (b) Two-dimensional interference patterns generated by the FP interference effect.

the ferromagnetic metal reservoirs are different for spin-up and spin-down electrons, the formation of the spin-singlet states with an unpaired electron in the dot is significantly hampered, and even expected to be fully suppressed when the QD is contacted by fully spin-polarized electrodes. We will discuss the Kondo effect incorporated with ferromagnetism in more detail in Chapter 5, with experimental observations in ferromagnet-contacted SWCNT QD.

2.2.4 Fabry-Perot Interference Effect

The charge transport mechanism becomes different when the metal contacts to SWCNTs are nearly transparent. In this regime, the number of electrons in the SWCNT QDs is no longer defined, and the Coulomb charging effect does not play a role in the charge transport. Electron transport through SWCNTs can be considered as wave propagation in a one-dimensional wave guide, which is often referred to as Fabry-Perot (FP) resonator [35]. A schematic diagram of the FP resonator is illustrated in Fig. 2.9 (a). Two mirrors in a usual FP resonator are replaced with source and drain electrodes, and the one-dimensional SWCNT replaces the wave guide. The SWCNT QD parameters, R, C, and Γ, which are used for analyzing the transport behavior in the Coulomb blockade regime are now replaced with the transmission and reflection coefficients, $t_{s,d}, r_{s,d}$ of each electrode. The conductance can be expressed by the total transmission of the SWCNT resonator :

$$G = \frac{2e^2}{h} T_{tot} \ \ , \ \ T_{tot} = \frac{T_s T_d}{|1 - \sqrt{(1-T_s)(1-T_d)} e^{i\delta}|^2}, \tag{2.8}$$

where $T_{s,d} = |t_{s,d}|^2$, and δ is an energy and length dependent parameter. Two-dimensional FP interference pattern as a function of bias and gate voltages is illustrated in Fig. 2.9. The FP resonator behavior was first experimentally demonstrated by Liang *et al.* [27]. To explain the experimental data, they extended the basic concepts of the FP resonator to consider two degenerate conduction channels in metallic SWCNTs by using Landauer-Büttiker formalism. The FP interference effect has also been observed in superconductor [36] and ferromagnet-contacted SWCNTs [37].

In this thesis, we will discuss the new MR features relating to the FP interference effect observed in ferromagnet-contacted SWCNT. We find that the MR is indeed influenced by the quantum inference effect. Detailed experimental observations and discussions will be presented in Chapter 4.

2.3 Spin-Dependent Transport

2.3.1 Spintronics

Spintronics is the recently developed terminology for the electronics, in which electron spins are considered as the basic unit for information. Ever since the first transistor was realized at Bell labs in December 1947, modern electronics have heavily relied on electron charges. However, the first commercial product using the giant magnetoresistance (GMR) effect was introduced to the market in 1997 [1]. GMR is a quantum mechanical effect observed in magnetic layered film, which is related to

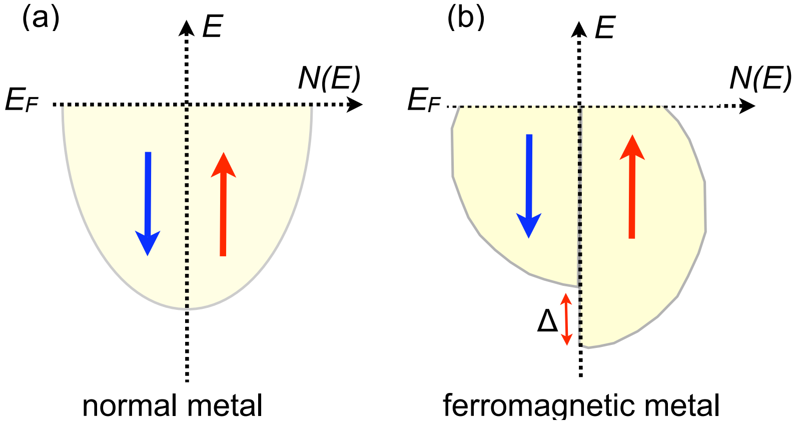

Figure 2.10: A schematic diagram of the density of states for (a) normal metal and (b) ferromagnet.

the electron spins, not charges, so the output signal in GMR based devices can be controlled by the external magnetic field. GMR based devices have been exclusively used in data-storage applications such as hard drives. Another spintronic-device was found in the magnetic tunnel junctions [38, 39], which are based on tunneling magnetoresistance (TMR) effect.

Spin-Dependent Transport

Spin-dependent transport will happen in any systems as long as there are spin-unbalanced charges at the Fermi level. The most commonly found spin-unbalanced systems are ferromagnetic materials, such as Fe, Co, Ni, Dy, Gd and their alloys. Figure 2.10 illustrates a band diagram of (a) normal metal, and (b) ferromagnet, respectively. In a normal metal, spin-up and spin-down electrons are equally distributed at the Fermi energy. However, in a ferromagnet, the electron density of states become spin dependent. Because of the exchange coupling that exists in ferromagnets, spin-up and spin-down electron bands are separated by the exchange energy Δ, and eventually causes different density of states for the spin-up and spin-

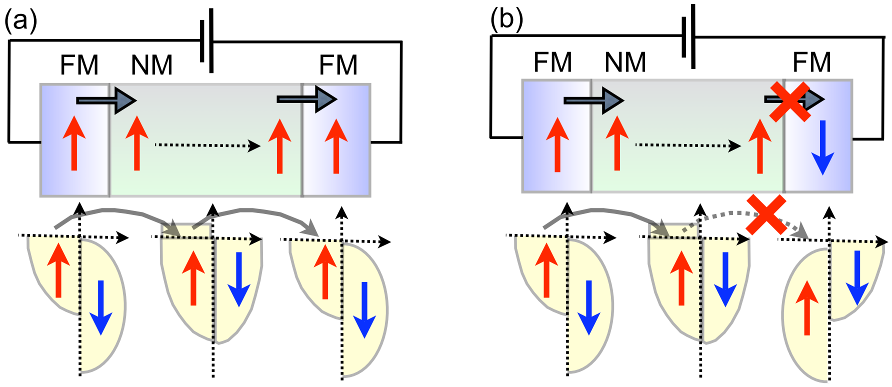

Figure 2.11: Schematic representations of spin-polarized transport from a ferromagnet / normal metal / ferromagnet (GMR) device. (a) The spin-polarized electrons can flow through the channel (on-state). (b) The spin-polarized electrons are blocked because there are no available states for spin-up electrons at the drain electrode (off-state).

down electrons at the Fermi level, as shown in Fig. 2.10 (b). The strength of spin polarization $\mathcal{P}$ is defined by the density of states of spin-up, $N(E_F)_\uparrow$ and spin-down, $N(E_F)_\downarrow$ electrons at the Fermi energy :

$$\mathcal{P} = \frac{N(E_F)_\uparrow - N(E_F)_\downarrow}{N(E_F)_\uparrow + N(E_F)_\downarrow}. \tag{2.9}$$

The polarization of pure ferromagnets is measured to be typically $\leq 50\%$ [40], and 100% polarization can also be obtained in some magnetic oxide compounds [41]. The most widely used spintronic devices are made of either alternating ferromagnet (FM) /normal metal (NM) films such as in a GMR device, or an insulating layer sandwiched by two ferromagnetic films, which exploits the spin-polarized TMR effect.

The basic mechanism of spin-dependent GMR effect is illustrated in Fig. 2.11. We assume that the polarization of ferromagnetic electrodes is $\mathcal{P} = 100\%$ for simplicity. At first, spin-up electrons are injected from the FM into the NM, and transport through the NM. The spin-polarized electrons are then extracted to the

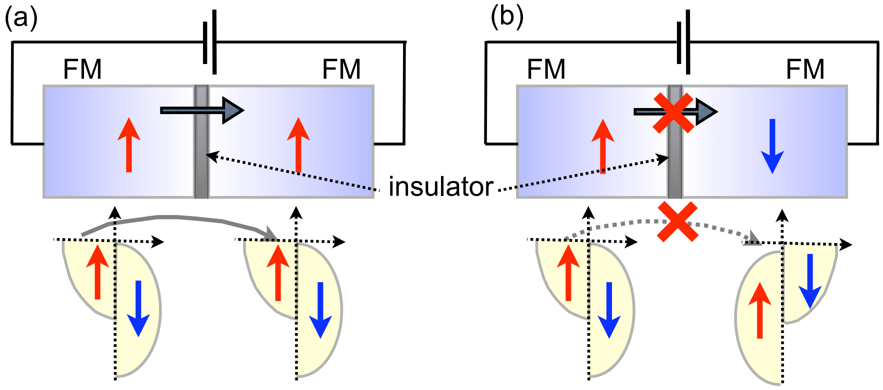

Figure 2.12: Schematic representations of spin-polarized transport from a ferromagnet / insulator / ferromagnet (TMR) device. (a) The spin-polarized electrons can flow through the barrier (on-state). (b) The spin-polarized electrons are blocked because there are no available states for spin-up electrons at the drain electrode (off-state).

other FM, whose polarization is aligned in either the same or the opposite direction of the transported electron spins. The GMR device switches from on (current flow) and off (no current flow) depending on the relative spin polarization of the FM electrodes. This simple device scheme is referred to as spin-valve (SV). In SV devices, one of two FM electrodes is fabricated to change its spin polarization at higher external magnetic field than the other to realize the parallel or anti-parallel spin configurations. This can be achieved by letting one of the FM electrodes interact with an antiferromagnetic film. The exchange coupling between the FM and antiferromagnetic films make the switching of the polarization of the FM difficult [42]. The other possibility is to make the physical dimension of each FM electrode different. Because it requires higher magnetic field to switch the polarization of a narrower electrode than that of a wider electrode, the parallel and anti-parallel spin configurations can be achieved [43]. We have utilized the latter scheme in our FM contacted SWCNT devices, and it has worked nicely.

NM conducting channels in the GMR devices can be replaced with an insu-

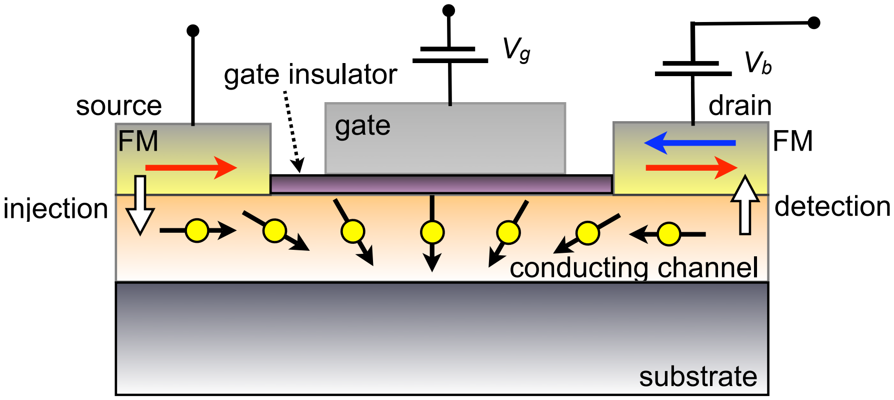

Figure 2.13: Schematic diagram of spin FET. The injected spins from the FM source are modulated by the gate electric field, and detected by the FM drain electrode.

lating layer as shown in Fig. 2.12. In this scheme, the spin-polarized electrons tunnel through the insulator. The TMR effect was first observed at low temperature by Julliere in 1975 using a Ge insulating layer sandwiched by Fe films [44]. However, it had taken almost two decades to receive interests from engineering communities when the first room temperature TMR effect was demonstrated with an aluminum oxide layer [45]. The basic transport mechanism of TMR is almost identical to that of GMR, except for the tunneling of spin-polarized electrons. Since the conductance through the TMR device is determined by the density of states at the Fermi energy of the FM electrodes, the conductance in the parallel, G^P and anti-parallel configurations, G^{AP} can be determined by the density of states. In the model proposed by Julliere, TMR is defined by following [44] :

$$\mathrm{TMR} = \frac{R^{AP} - R^P}{R^P} = \frac{G^P - G^{AP}}{G^{AP}} = \frac{2\mathcal{P}_1\mathcal{P}_2}{1 - \mathcal{P}_1\mathcal{P}_2}. \tag{2.10}$$

Here, $\mathcal{P}_1$ and $\mathcal{P}_2$ are the spin polarizations of the first and the second FM electrodes.

2.3.2 Spin Field-Effect Transistor

Both GMR and TMR devices are basically based on a two-probe geometry, in which the electronic signal is controlled by an external magnetic field. In 1990, Datta and Das proposed a new type of semiconductor-based spintronic device, whose geometry is similar to the conventional FETs as shown in Fig. 2.13 [46]. This electronic device is referred to as a spin FET. In spin FETs, spin-polarized electrons are created and detected by FM source and drain electrodes, and manipulated by a gate. The electric field generated by the gate electrode controls the spin orientation in the semiconducting channel through the spin-orbital coupling [47]. Since the degree of the spin precession is controlled by the gate, the current through the channel is a function of both the external gate voltage and magnetic field. The experimental realization of the spin FET is yet to be reported, mainly because of the difficulty in efficient spin injection to semiconductors.

2.4 Spin Transport in Carbon Nanotubes

2.4.1 Background and History

Carbon systems have been considered one of the promising candidates for spintronic materials. The spin-orbital coupling is negligible in carbon systems compared with typical metals and semiconductors [48]. Carbon nanotubes have extraordinary long elastic- and phase-coherent lengths, up to several μm [49], which are essential for the realization of spin transport. Besides, as discussed earlier, carbon nanotubes also have intriguing electronic properties, including one-dimensional and zero-dimensional QD behavior. These unique characteristics make SWCNT interesting for the study of how spin transport is influenced by the different transport mechanisms, such as the Coulomb blockade, the Kondo effect and the FP interference effect.

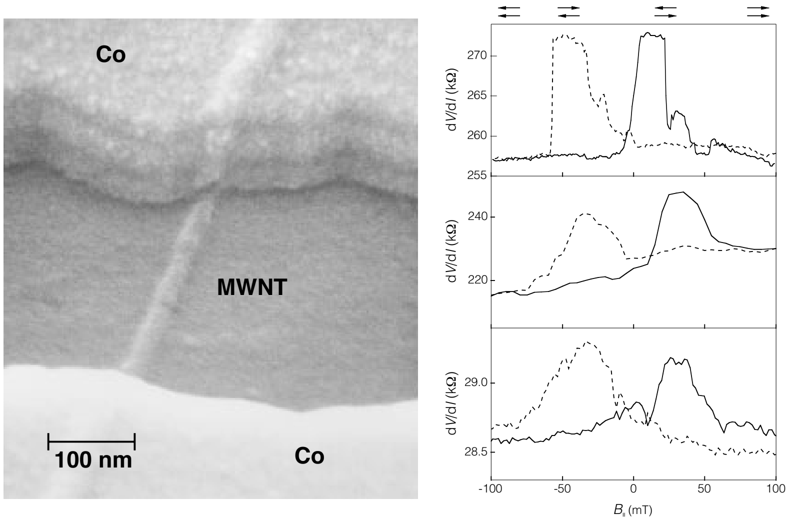

Figure 2.14: The first spin transport measurement with carbon nanotubes. (a) SEM image of the Co contacted MWCNT. (b) The differential conductance as a function of external magnetic field measured from three different samples. (from Ref. [3])

Previous Studies of Spin Transport through Carbon Nanotubes

The first spin transport in carbon nanotubes was reported by Tsukagoshi *et al.* in 1999 [3]. Figure 2.14 shows a scanning electron microscopy (SEM) image of their device and the representative MR switchings as a function of external magnetic field. They measured up to ∼ 9% MR switching, and 130 nm spin-flip scattering length, from the Co contacted MWCNTs. Ever since the first realization, spin transport through MWCNTs have been reported by a few groups with different FM materials such as Co [50] and Pd/Ni alloy [51]. In addition, improved MR switching up to ∼ 60% was also observed in MWCNT contacted by perovskite manganite $La_{0.7}Sr_{0.3}MnO_3$ (LSMO) films [52]. The first spin-dependent transport in SWCNTs was also observed in 2002 by J. Kim *et al.*, where they used Co electrodes [53]. Similar to MWCNTs, several different FM films have been used to inject and detect spins in SWCNTs, including Fe [54], Co [53], Ni [55] and magnetic semiconductor GaMnAs [54]. However, all of the experimental observations mentioned above could

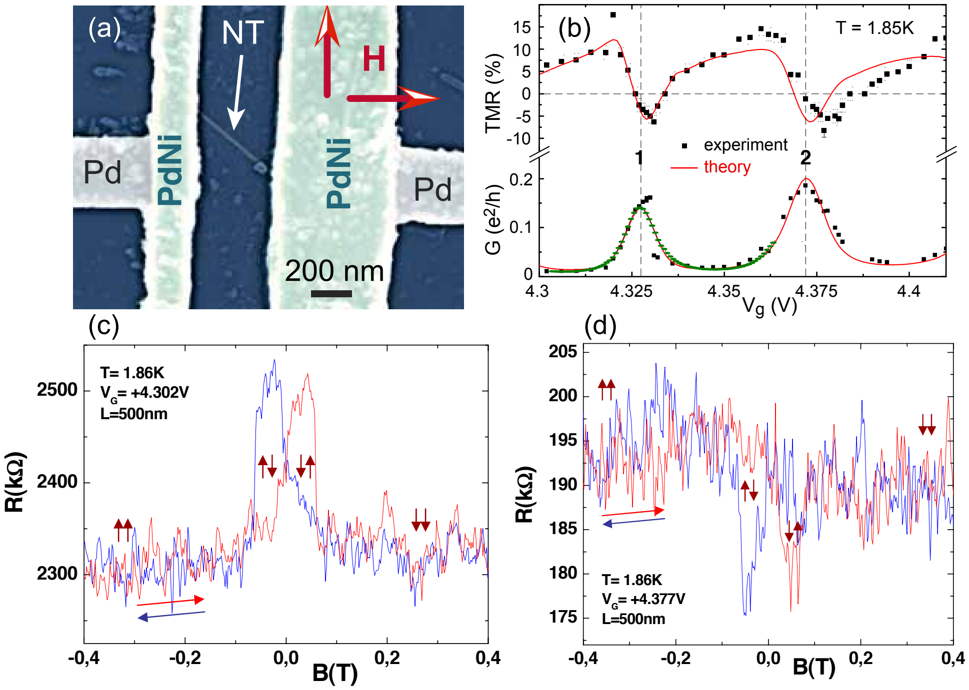

Figure 2.15: (a) SEM image of the Pd/Ni-contacted SWCNT. (b) Conductance and calculated MR as a function of gate voltage measured at $T = 1.85$ K. (c) and (d) are representative positive and negative MR switchings, respectively. (from Ref. [4, 56])

not be called as spin FETs, because of the missing gate control.

Recently, Sahoo *et al.* reported the first FM-contacted SWCNT showing the gate voltage dependent MR in the Coulomb blockade regime [4]. Figure 2.15 (a) shows the SEM image of their Pd/Ni-contacted SWCNT device. The spin signal which is manifested as the MR switching was indeed observed to be dependent on the gate electric field. Figure 2.15 (b) displays MR data and conductance in the same gate voltage range showing clearly the gate voltage dependence on the MR. Furthermore, negative MR switching, i.e., low resistance in the anti-parallel configuration, was observed. The representative positive, i.e., high resistance in the anti-parallel configuration, and negative MR switching are shown in Fig. 2.15 (c) and (d), respectively. The oscillatory behavior of MR was explained by the non-interacting resonant tunneling model using the Breit-Wigner formula, and the MR sign change was claimed to be attributed to the highly anisotropic electrode couplings.

It is worth noting that this is the first observation of spin-dependent transport measurement exhibiting not only the gate voltage dependence, but also the connections to the corresponding quantum charge transport mechanism. After this experiment, spin-related transport behavior was also observed in the FP interference regime, and showed the gate voltage dependent MR oscillations as well [37].

2.4.2 Motivation

The fascinating electronic properties of SWCNTs have attracted much attention and most of the basic properties are well understood now. However, the situation becomes less clear when the additional parameter, spin, is added to the system. Even after the seminal work done by Sahoo *et al.* [4] and Man *et al.* [37], understanding of spin transport incorporated with quantum charge transport phenomena is still in its early stages. The experimental methods for consistent and reliable spin manipulations in SWCNTs are yet to be developed. In addition, it is still open to debate whether the conventional two probe geometry is reliable enough to observe spin transport through carbon nanotubes [57].

In fact, several questions have been raised whether the spin signals observed from the two-probe FM-contacted nanotubes could be from other effects, such as the anomalous magnetoresistance (AMR) effect [43], magneto-Coulomb effect (MCE) [58], Hall effect [59], and tunneling anisotropic magnetoresistancelike effect [54, 60]. These effects are mainly from the interactions between FM electrodes and external magnetic field, and not from the spin-dependent transport through SWCNTs.

All of these questions along with technical difficulties make this field even more challenging. Despite these hurdles, there are still lots of unexplored and unexplained physical phenomena, such as the spin-charge separation expected to be present in one-dimensinal Luttinger liquid systems [61, 62]. In this thesis, we will report some of new experimental observations regarding spin transport through SWCNTs, and their connections to several quantum transport phenomena including the Coulomb blockade effects, the Kondo effects, and the FP interference effects.

Chapter 3

Fabrication of Ferromagnet-Contacted Single-Walled Carbon Nanotubes and Measurements

3.1 Introduction

In this chapter, the overall fabrication processes of ferromagnet-contacted single-walled carbon nanotubes (SWCNTs) and experimental details will be presented. First, the growth method for SWCNTs will be described. Next, the detailed procedures for patterning techniques, especially e-beam lithography and lift-off will be discussed. Then, step-by-step fabrication methods for realizing ferromagnet-contacted SWCNT devices will be discussed. Finally, the basic measurement setup and experimental details will be presented.

3.2 Overview

The fabrication process for ferromagnet-contacted SWCNT devices is comprised of four main parts: (i) growth of SWCNTs, (ii) locating nanotubes, (iii) ferromagnetic

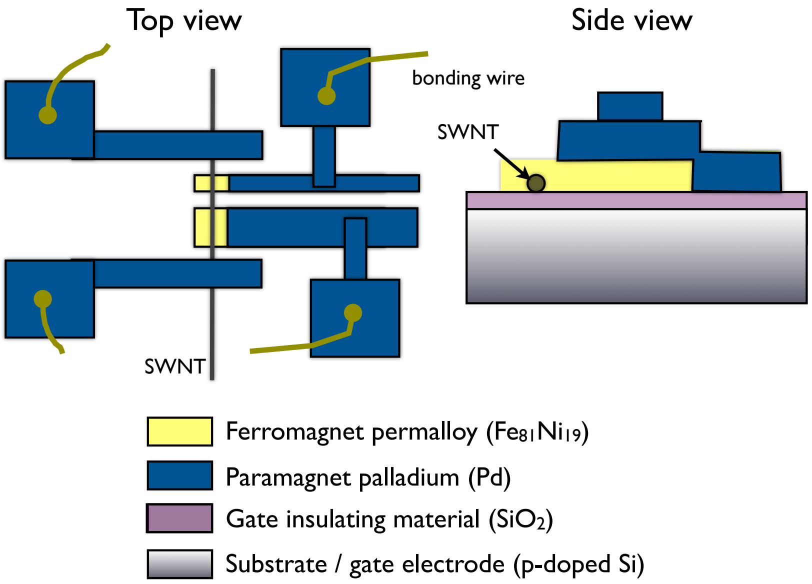

Figure 3.1: Schematic diagrams of a ferromagnet-contacted four-probe SWCNT device.

electrode fabrication, and (iv) fabrication of extension lines and bonding pads.

Figure 3.1 shows schematic diagrams of a four-probe ferromagnet-contacted SWCNT device viewed from top and side, respectively. It mainly consists of ferromagnetic permalloy (Py, $Ni_{81}Fe_{19}$) source and drain electrodes, and additional two paramagnetic palladium (Pd) electrodes. Two ferromagnetic electrodes will be utilized for spin injection and detection, and the Py electrodes will be used as reference voltage probe and current source in a nonlocal measurement scheme. For a local measurement, only two ferromagnetic source and drain electrodes are required. All electrodes are connected to 150×150 μm^2 Pd bonding pads for electric measurements.

3.3 Growth of Single-Walled Carbon Nanotubes

The SWCNTs used in this thesis are grown on top of silicon substrates by the well known chemical vapor deposition (CVD) technique, developed by Kong *et al.* [63]

Substrate Preparation

The Si-substrates used in this study are degenerately p-doped so that they maintain reasonable conductivity at low temperature, and can be used as a back gate in our measurement. The oxide thickness of our devices is in a quite broad range of 300 nm − 600 nm. We either grew silicon oxide at the Microelectronics Research Center in the J. J. Pickle Research campus, or directly purchased commercially available Si/SiO_2 substrates. The 300 nm oxide wafers were purchased from Nova Electronic Materials. Ltd, and the resistivity of these <100> wafers is $0.001 - 0.003\ \Omega\cdot\mathrm{cm}$ at room temperature.

The Si/SiO_2 substrate needs to be annealed at high temperature in H_2. The hydrogen annealing is known to reduce dangling bonds of SiO_2, which can act as charge trap sites [64]. The annealing is performed at 900 °C for more than one hour in a mixture of hydrogen and argon. The ratio of H_2/Ar mixture is approximately $1:1$, and the flow rate of hydrogen is ~ 1 liter-per-minute.

Catalyst Preparation

SWCNTs are grown from pre-deposited catalysts. For the original catalyst in Ref. [63], 15 mg Aluminum nanoparticles (Fumed Alumina, Degussa Corporation), 20 mg $Fe(NO_3)_3\cdot 9H_2O$ and 5 mg $MoO_2(acac)_2$ (both from Aldrich) are added to 150 ml of methanol and sonicated overnight. The concentration of catalyst can be optimized depending on the density of grown nanotubes. The catalyst used in this thesis is the original catalyst diluted to 1:400 ratio, i.e., 1 ml of original catalyst in 400 ml of methanol.

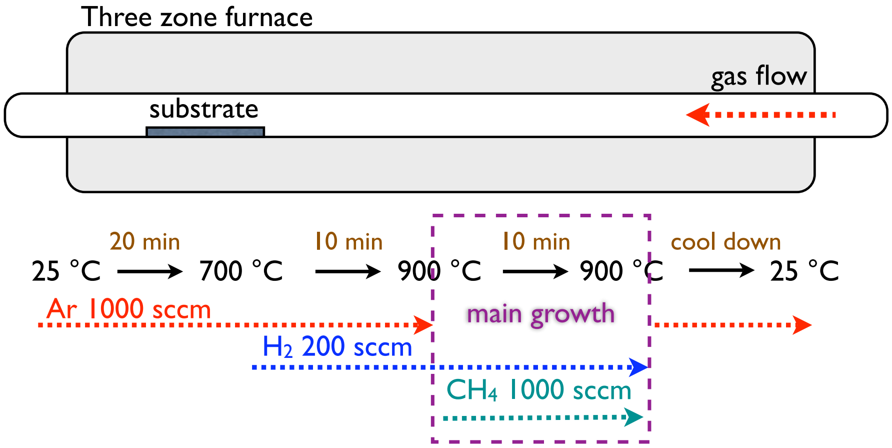

Figure 3.2: Schematic diagram of SWCNT growth furnace and detailed growth conditions.

SWCNT Growth

Diluted catalysts (1:400) are spin-casted on top of pre-annealed substrate diced to a size of 14 × 14 mm^2. Before the spin casting, the diluted catalysts are sonicated for one hour. The setting for the spin coater is 3000 rpm for 1 min. The catalyst coated substrate is transferred into a 1-inch quartz growth tube placed in three zone furnace as shown in Fig. 3.2. The substrate is positioned as for downstream of gas flow as possible so that the reactant gas, methane (CH_4) is more dissociated [65]. The temperature, time setting and gas flow rate are illustrated in the lower half of Fig. 3.2. The hydrogen used in the growth is ultra-high-purity research grade (99.999%), and the methane is high-purity grade (99.96%), and both gases were purchased from Praxair Ltd.

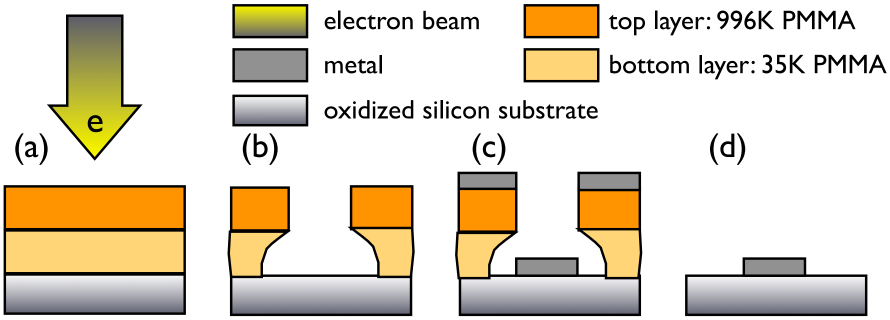

Figure 3.3: Schematic diagrams of electron beam lithography. (a) PMMA resist coating and e-beam exposure, (b) development. (c) metal deposition and (d) lift-off.

3.4 Device Fabrication

3.4.1 E-beam Lithography

Three independent e-beam lithography and lift-off processes are required in a single sample preparation cycle: (i) fabrication of alignment marks, (ii) ferromagnetic contact to carbon nanotubes and (iii) fabrication of normal metal extension lines and bonding pads. Each e-beam lithography consists of four steps as shown in Fig. 3.3 : (a) Polymethyl methacrylate (PMMA) resist coating and e-beam exposure, (b) development, (c) metal deposition, and (d) lift-off.

PMMA Resist Coating and E-Beam Exposure

Two homemade PMMA resists are used for bi-layer coating to improve undercut. For the bottom layer, 4.7 g of 35,000 molecular weight (8%, 35K) PMMA (Acros Organics) is dissolved in 50 ml chlorobenzene (99+%, Acros Organics) for more than 24 hours. A magnetic stir bar is used to help PMMA dissolution further. The top layer, 4% 996K PMMA, is prepared from the same procedure, except with 4.7 g of 996,000 molecular weight PMMA (Aldrich) in 100 ml of chlorobenzene.

At first, 35K PMMA is spin-coated at 6000 rpm for one minute as a bottom layer on nanotube grown susbtates. The resultant thickness of the layer is around 430 nm. The film is baked in a convection oven at 170°C for 30 minutes. Next, 996K PMMA is spin-coated at 6000 rpm for one minute as a top layer, resulting in 370 nm in thickness, and baked again at 170°C for 30 minutes. The pre-designed patterns are exposed by electron-beam lithography using a 20 keV electron beam in a Raith 50 pattern generator equipped with a laser sample stage. We usually use 220 μC/cm^2 as a dose factor.

Development

The e-beam exposed PMMA can be dissolved in a developer. Here, we use a 1:1 mixture of 2-isopropanol (IPA) and 4-methyl-2-pentanone (99.5% MIBK, Acros Organics). Samples are gently stirred in the developer for 60 seconds, then transferred and stirred in methanol for 30 seconds. Samples are blown dry with dry nitrogen after an additional 30-second rinsing with IPA.

Metal Deposition

There are several metal deposition techniques including E-beam evaporation, thermal evaporation and sputtering. Different evaporation methods are chosen depending on the properties of deposited metal. In the process of our ferromagnet-contacted SWCNT devices, the thermal evaporation is used in the first metal deposition for the fabrication of alignment marks made of Cr and Au. The E-beam evaporation method is used for both Py and Pd film in the second and third metal deposition steps.

Lift-off

The final metalized structure is obtained by removing PMMA resists in boiling acetone. The sample is first soaked in indirectly heated acetone for 7 minutes, and gently blown with a pipet for an additional 5 minutes. Next, the sample is transferred to preheated clean acetone, followed by the same procedure, 7 minute soaking and 5 minute blowing. We follow the same procedure more than three times to ensure clean samples without PMMA residue. Finally, the sample is rinsed in boiling IPA and blow dried with dry nitrogen.

3.4.2 Fabrication of Alignment Marks and Electrode Design

The relative position of grown SWCNTs is defined by alignment marks. The Cr (5nm) / Au (35nm) alignment marks are fabricated by e-beam lithography and lift-off process, and each alignment mark is designed to be unique so that we can locate the relative position of an individual SWCNT, as shown in Fig. 3.4 (a). The spacing between alignment marks is 10 μm and the total area of the marks is 80×80 μm^2.

After the fabrication of alignment marks, the substrates are scanned by tapping mode atomic force microscopy (AFM). Figure 3.4 (b) shows an AFM image of several SWCNTs grown from pre-deposited catalysts and alignment marks. Since the scan area of an individual scan is around 24×24 μm^2 (512 lines per image) and scan speed is maintained to be slower than 20 μm/s, this is one of the most time consuming steps in the whole sample fabrication process.

Since we need to control the relative spin polarization of ferromagnetic electrodes in the parallel or anti-parallel configurations, the coercive field B_c for both electrodes need to be different. In order to fabricate ferromagnetic electrodes with different B_c, we design them in different aspect ratios, because it requires higher magnetic field to switch the polarization of the narrower (hard) electrode than the wider (easy) electrode [43]. The dimension of the easy electrode is 3.0×0.5 μm^2, and that of hard electrode is 3.0×0.07 μm^2 or 3.0×0.05 μm^2. The distance between the electrodes is designed to be $200 - 300$ nm. To ensure both well-defined electrodes and absence of PMMA residues around electrodes, the dosage for e-beam should be

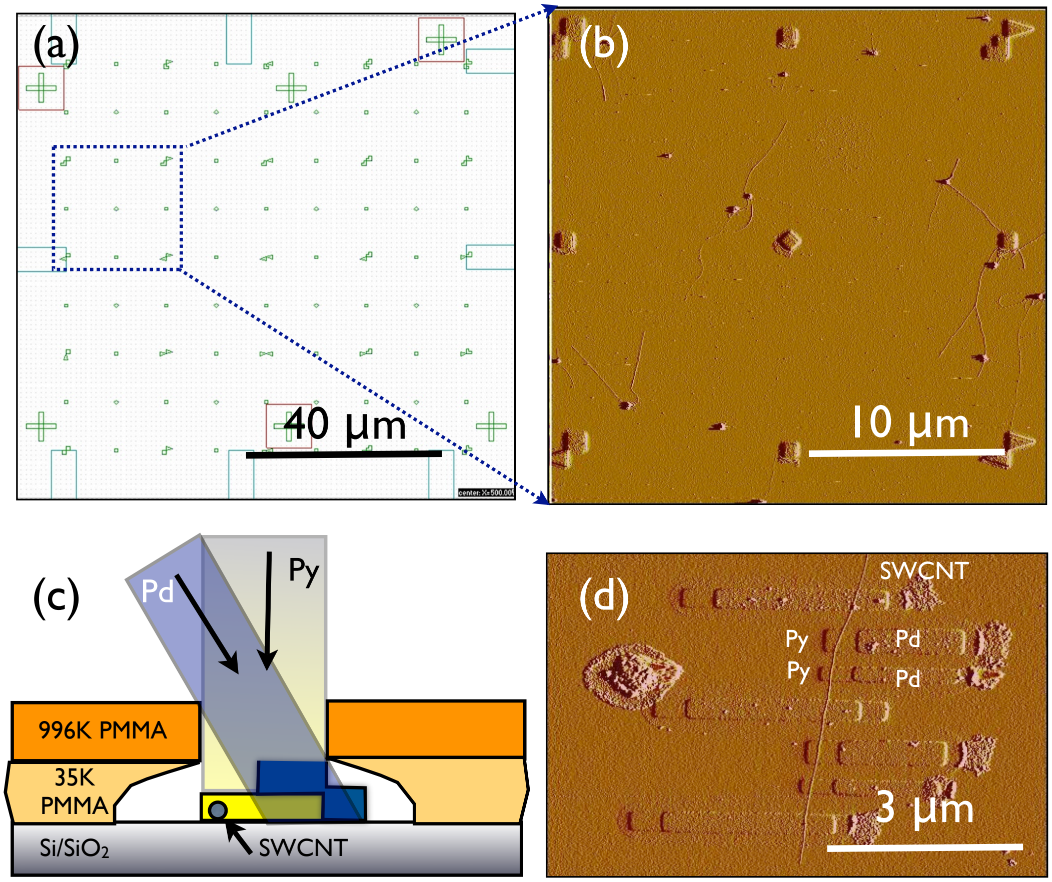

Figure 3.4: (a) Schematic diagram of alignment marks. (b) AFM image of selected area. (c) Schematic diagram of Py and Pd angle evaporation. (d) AFM image of SWCNT contacted by multiple ferromagnetic electrodes.

tested in advance.

3.4.3 Ferromagnetic Electrodes

After e-beam exposure and development followed by the procedure described in the previous section, the sample is mounted in an E-beam evaporation chamber for Py and Pd deposition. First, Py is deposited on top of pre-located SWCNTs at 90 degrees to the surface. Subsequent palladium evaporation is followed without breaking vacuum, after the sample stage is rotated by a certain degree with the long axis of electrodes aligned in the direction of metal evaporation. The rotation of the sample stage is to avoid possible Pd electric contacts to SWCNT, while ensuring most of permalloy is protected by Pd from oxidization.

The base pressure of the E-beam evaporator (Edwards Auto 500) in the Center for Nano- and Molecular Science and Technology (CNM) is in the high 10^{-6} mbar range, and it can be improved to low 10^{-6} or high 10^{-7} mbar using a liquid nitrogen cold trap. During evaporation, a bar magnet is placed on top of the sample stage to align the magnetization of the permalloy film. After reaching base pressure, $12-13$ nm Py film is deposited at a rate of ~ 0.7 $\mathring{A}$/s, and ~ 15 nm Pd evaporation is followed at a rate of ~ 0.5 $\mathring{A}$/s. An AFM image of Py/Pd-contacted SWCNT is presented in Fig. 3.4 (d). Since the offset from the angle evaporation is not more than 300 nm given the chamber geometry, careful pattern design and alignment process are required.

3.4.4 Fabrication of Bonding Pads and Sample Packaging

In the two-probe local measurement scheme, the final Pd extension lines and bonding pads are fabricated by an additional e-beam lithography and lift-off process. The width of extension lines is designed as 0.5 μm, and Pd is evaporated to more than ~ 50 nm in thickness to guarantee the electrical contact to pre-deposited Py/Pd electrodes. In a four-probe non-local measurement scheme, additional Pd electrodes are designed to be 3×0.5 μm^2, and the extension lines and bonding pads are fabricated by the same procedure as local measurement samples. A schematic diagram of final extension lines and bonding pads are illustrated in Fig. 3.5 (b) and (c), respectively, and the SEM image of the final device is shown in Fig. 3.5 (a).

After finishing the final lift-off, the sample is mounted on a 28-pin chip carrier (Spectrum, LCC02834) as shown in Fig. 3.5 (d). In order to use oxidized silicon

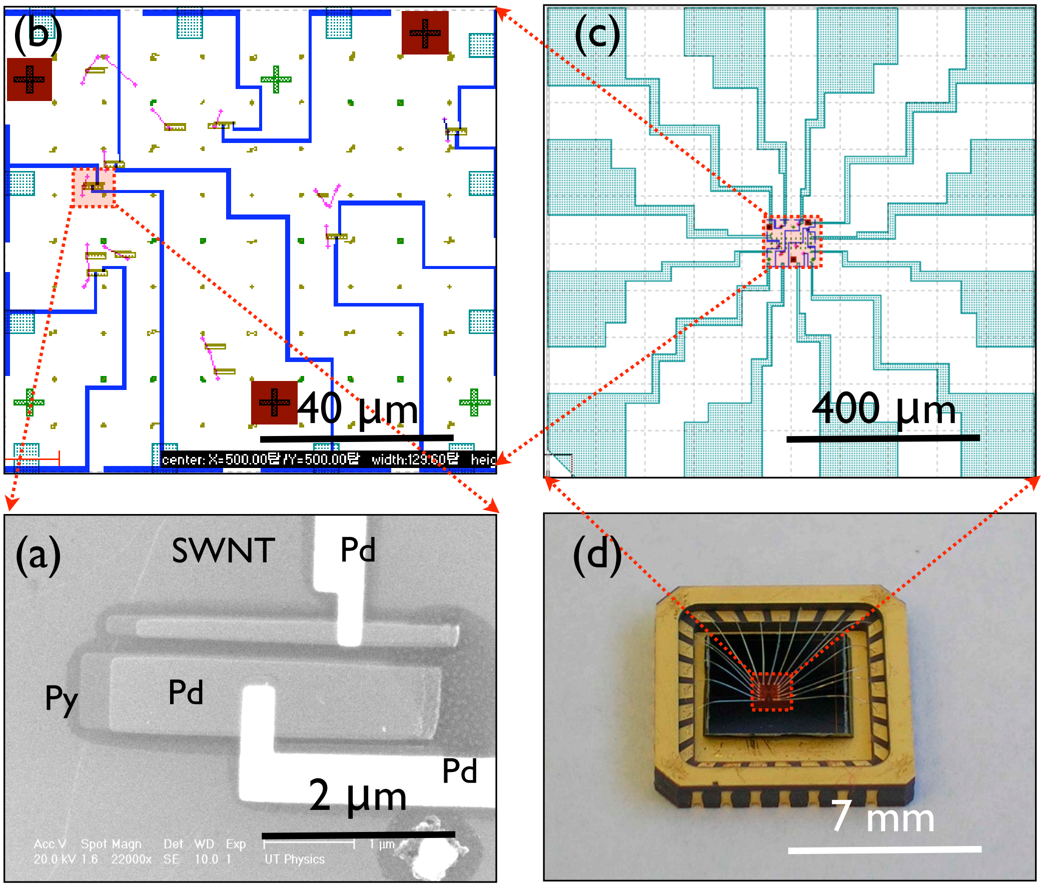

Figure 3.5: (a) SEM image of a final device. (b) Schematic diagram of a final lithography pattern generated by Raith 50 software. (c) Schematic diagram of bonding pads generated by Raith 50. (d) Optical image of a sample packaging after wire bonding.

substrate as a back gate, the oxidization layer of the backside substrate is removed by scratching using a scriber. Sample mounting needs extra caution so that the easy axes of the ferromagnet electrodes are positioned in the same direction as the external magnetic field. The final nanotube devices are completed by connecting bonding pads to Au-plated pads on the chip carrier with Al bonding wires using a ultrasonic wire bonder (West Bond 7476D). An optical image of the final sample is shown in Fig. 3.5 (d).

Before cooling down the samples to liquid helium temperatures, the electric connections of the samples can be tested quickly to see if they worth cooling down. The samples showing high resistance ($\geq$ MΩ) at room temperature usually do not show large enough current to measure at low temperature. For non-local devices, all three pairs of each nanotube segment should show reasonably low resistance values.

3.5 Electric Measurement Setup and Experimental Details

For DC current-voltage measurement, a bias DC voltage is applied through a low-pass RC filter with a cut-off frequency ($f = 1/2\pi RC$, where $R = 20\ \Omega$ and $C = 470\ \mu$F) at 17 Hz. A voltage divider is used to improve the resolution of the data acquisition card (National Instruments, DAC PCI-6052E) voltage output, which is about 0.3 mV for a 16 bit DAC. The DAC voltage resolution is improved to 0.003 mV by using a 100× divider, at the expense of reduced voltage range by a factor of 100. The noise level is reduced also by using a voltage divider. A gate DC voltage is also applied through a low-pass filter and sometimes a voltage divider as well. The current extracted from a drain electrode is amplified by the current preamplifier (DL Instruments, DL 1211), and the voltage signal from the current amplifier is read by the NI-DAC. The temperature is monitored and controlled by a

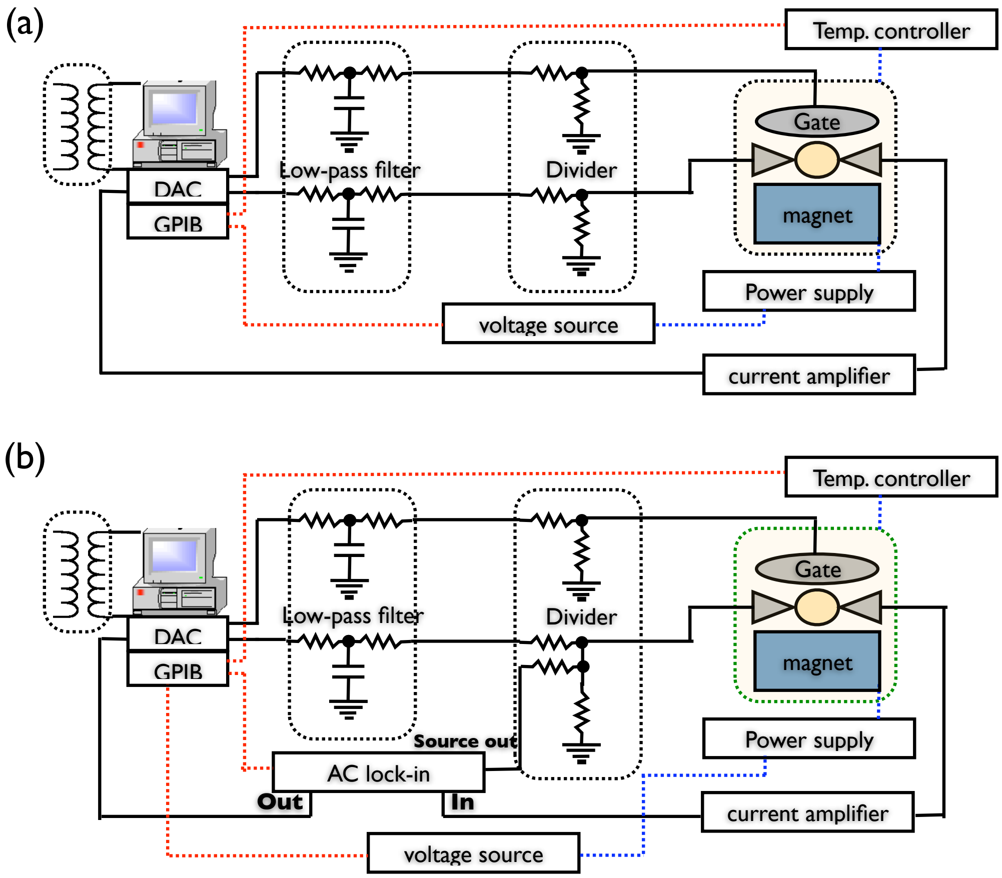

Figure 3.6: Schematic diagrams of measurement setup. (a) DC measurement (b) AC measurement.

LakeShore Temperature Controller 331 via GPIB communication. The 2 T superconducting magnet is controlled by a KEPCO power supply. The overall setup for AC measurement is similar to DC measurement except that an additional sinusoidal excitation bias voltage from an AC lock-in amplifier (Stanford Research Systems, SR830) is added to the existing bias voltage through an additional resistor as shown in Fig. 3.6 (b). AC measurement usually requires more time than DC, but it has the advantage of reduced noise level.

Chapter 4

Spin Transport in Individual Single-Walled Carbon Nanotubes with Highly Transparent Ferromagnetic Contacts

4.1 Introduction

The realization of spin transport through carbon nanotubes has attracted tremendous attention during the last decade from both scientific and engineering communities, ever since the first experimental observation was reported from Co-contacted multi-walled carbon nanotubes (MWCNTs) by Tsukagoshi *et al.* in 1999 [3]. The carbon nanotubes are considered one of the most promising spin-information conveyors because of the ballistic nature of electron transport [49], and the relatively long spin-coherence length due to the negligible spin-orbital coupling [23]. Besides, in modern electronics, spintronic-devices are following the same pace of miniaturization as electronic devices have been through. Because of their minuscule scale, quantum mechanics is required to understand charge and spin transport behaviors through nanoscale-sized devices. Thus, investigating spin-dependent transports in these quantum transport regimes is of particular importance. As discussed in Chapter 2, single-walled carbon nanotubes (SWCNTs) electronically confined by metal electrodes show a broad range of quantum transport behavior depending on how well they are coupled to the metal electrodes. As the transparency of metal contact with SWCNTs is decreased, for example, the charge transport changes from the Fabry-Perot (FP) interference [27] to the Coulomb blockade [26]. Accordingly, when metal electrodes are fabricated with ferromagnetic films to manipulate electron spins, SWCNTs will allow us to explore spin-dependent transport in several quantum transport regimes.

Recently, Sahoo *et al.* observed that spin transport in SWCNTs are indeed correlated with corresponding charge transport in the Coulomb blockade regime [4]. Man *et al.* also observed the spin-dependent transport in the FP interference regime, and found that the oscillatory behavior of magnetoresistance (MR) is related to the quantum interference effect [37].

In this chapter, we will report on the some new observations of the spin-dependent transport behavior in the FP interference regime. From the report in Ref. [37], MR showed oscillatory behavior as a function of gate voltage. The highest MR occurred at the conductance valley, and the lowest MR which was close to $\simeq 0$ % was mostly observed at the conductance peak. This out-of-phase feature between the MR oscillations and the FP interference modulations is well explained by a single-channel FP model. However, in our device, the MR shows the opposite dependence on the conductance oscillations. The apex of the MR oscillations coincides with the conductance peak, and the MR dip occurs at the conductance valley. We refer to this gate-voltage-dependent MR oscillation as in-phase behavior. Furthermore, the MR at the dip shows negative switching, $\simeq -4\%$. The MR features shown in the gate voltage measurements are further supported by the bias voltage measurements. Our observations can be explained by a double-channel FP model with channel mixing at the metal contacts, and we found that the double-channel mixing is necessary to explain the negative MR switchings at the conductance valley. The observed in-phase MR oscillations as a function of both gate and bias voltages are well reproduced by numerical fitting. In addition, the oscillatory behavior of MR disappears at larger bias voltage, $V_b \geq 20$ mV, and at higher temperature, $T \geq 20$ K where the electron transport through the SWCNT no longer exhibits the FP interference effect.

4.2 Fabry-Perot Interference Effect

Figure 4.1 (a) shows a representative atomic force microscopy (AFM) image of a two-probe SWCNT device contacted by ferromagnetic permalloy (Py, $Ni_{81}Fe_{19}$). As described in Chapter 3, SWCNTs are grown by the chemical vapor deposition (CVD) method [63] on a highly p-doped Si/SiO_2 substrate, and contacted by ~ 13 nm Py film. On top of the Py, ~ 10 nm thickness of Pd film is evaporated to protect the Py from oxidization, and to secure the electric contact to the bonding pads in the final metallization process. With careful alignment process and the angle evaporation method, the electrical contact to SWCNTs is only made by ferromagnetic electrodes. The two-probe SWCNT device is completed by connecting the two ferromagnetic Py electrodes to the Pd bonding pads with an additional e-beam lithography and lift-off process. A scanning electron microscopy (SEM) image of the final device is presented in Fig. 4.1 (b). The dimension of the easy electrode (wider) is designed to be $3.0 \times 0.5\ \mu m^2$, and that of the hard electrode (narrower) is $3.0 \times 0.07\ \mu m^2$ in order to create different coercive fields for each electrode. The spacing between the electrodes is around $L \sim 250$ nm.

Figure 4.1 (c) shows the two-dimensional conductance plot as a function of both gate and bias voltage at $T = 4.2$ K. In this plot, the crisscrossing patterns

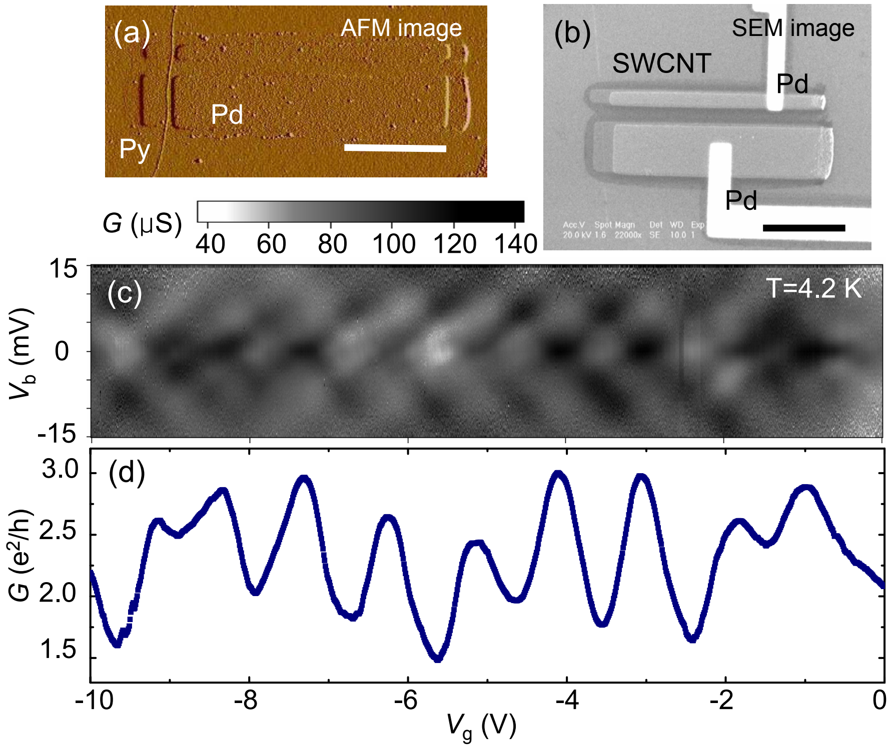

Figure 4.1: The representative (a) AFM and (b) SEM images of two-probe ferromagnetic contacted SWCNTs. (scale bar = 1 μm) (c) Two dimensional conductance plot as functions of both gate and bias voltages in the FP interference regime. (d) Conductance plot as a function of gate voltage at equilibrium ($V_b = 0$ mV).

generated by the interference effects in the FP resonator are conspicuous [27]. The conductance oscillates sinusoidally at around $G \sim 2.5\ e^2/h$ with a $\Delta G \sim 0.5\ e^2/h$ amplitude in the selected gate voltage range, $-8.5\text{ V} < V_g < -2.0\text{ V}$, as shown in Fig. 4.1 (d). The gate V_g and bias voltage V_b spacing between adjacent resonant lines, which is associated with the basic energy scale of the SWCNT FP resonator, can be determined by the channel length of the SWCNT. The measured energy scale is around $\Delta E \sim 6.9$ meV, and this agrees well with the theoretical expectation, $hv_F/2L = 6.6$ meV for $L = 250$ nm. Here, h is the Planck constant and $v_F = 8 \times 10^5$ m/s is the Fermi velocity of electrons in carbon nanotubes [23].

4.3 Energy-Dependent Magnetoresistance

4.3.1 Gate-Voltage Dependence

MR measurements is done by sweeping an external magnetic field between 200 mT and −200 mT. The MR used in this chapter is defined as $\text{MR} = (G^P - G^{AP})/G^{AP} = (R^{AP} - R^P)/R^P$, where $G^{P(AP)}$ and $R^{P(AP)}$ are the conductance and resistance in the parallel (anti-parallel) spin configurations of ferromagnetic electrodes. Figures 4.2 (a) and (b) show representative negative (i.e., $R^P > R^{AP}$), and positive (i.e., $R^{AP} > R^P$), MR switchings, respectively, at different gate voltages. To control the spin polarization ($\mathcal{P}$) of the ferromagnetic electrodes, the external magnetic field (B) is applied to the long axis of electrodes. Here, the magnetic field sweep direction is labeled as positive, when the field is ramped up from −200 mT to 200 mT, and the direction of the magnetic field sweep from 200 mT to −200 mT is referred to as negative. In Fig. 4.2, the closed red squares represent the positive sweep of the magnetic field, and the blue closed circles the negative sweep.

In these measurements, the magnetic field range where the electrode polarization is aligned in the anti-parallel configuration is different in the positive and

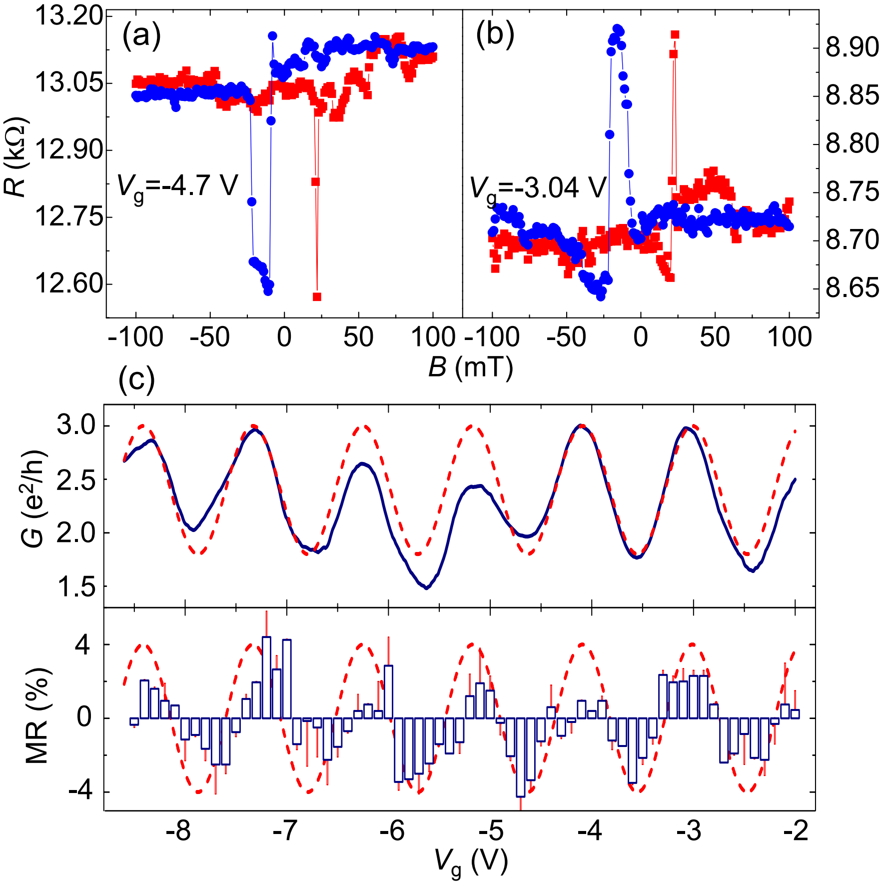

Figure 4.2: Gate voltage dependent MR in the FP interference regime. Representative negative and positive MR switchings at different V_g are shown in (a) and (b). Red closed squares are for the positive, and blue closed circles are for the negative magnetic field sweep. (c) Conductance and MR traces as a function of gate voltage at $V_b = 0$ mV. The sinusoidal function denoted by the red dashed line is a guide to the eye.

negative sweep directions. The range is $\Delta B = |B_{c2} - B_{c1}| = 15 \sim 16$ mT for the negative, and $\Delta B = 4 \sim 5$ mT for the positive sweep. Here B_{c1} and B_{c2} represent the coercive magnetic fields of the easy and hard electrodes, respectively. This asymmetric MR switchings may be attributed to the exchange coupling between the ferromagnetic film and the antiferromagnet oxide layer formed on top of the unprotected Py [42].

Figure 4.2 (c) shows the conductance (upper) and MR (lower) plots as a function of V_g in the FP interference regime. The MR shows three distinctive features: (i) The conductance and MR oscillate as a function of V_g with the same phase, i.e., in-phase feature. (ii) The value of MR switching at the conductance valley is negative. (iii) The shape of positive and negative MR oscillatory plots look almost symmetric around the vertical axis through the maximum and minimum MR points in each oscillation period. The sinusoidal curves represented by the red dashed lines are used as a guide to the eye.

The first two features cast a clear contrast with the previously reported data in the FP regime by Man *et al.* [37]. In their work, the conductance and MR oscillate in out-of-phase fashion, i.e., MR peaks (valleys) occur at the conductance valleys (peaks), and only positive MR switching was considered in data analysis, even though they actually saw negative MR switching as well. Only the third feature in our data shows resemblance to the previous report [37].

4.3.2 Bias-Voltage Dependence

In order to examine the observed MR features more closely, we performed bias voltage dependent measurements. The MR modulation as a function of bias voltage measured at the conductance valley **A**, and peak **B**, as labeled in Fig. 4.3 (a), shows clear in-phase MR behavior similar to the gate-voltage measurements. In Figs. 4.3 (b) and (c), closed red and blue circles represent the conductance in the

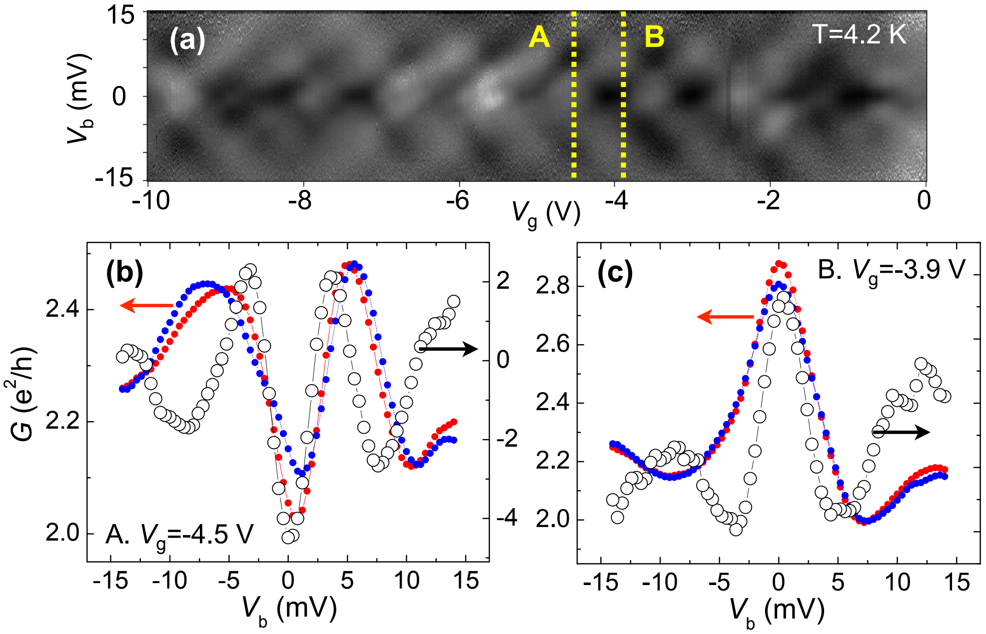

Figure 4.3: Bias voltage dependence of MR. (a) Two-dimensional conductance plot in the FP regime. (b) , (c) Conductance and MR oscillation as a function of bias voltage measured at conductance valley **A**, $V_g = -4.5$ V, and peak area **B**, $V_g = -3.9$ V. The closed red and blue circles represent the conductance in parallel and anti-parallel configurations, respectively, and the open dark circles are for the calculated MR.

parallel and anti-parallel configurations, respectively. At the conductance valley, the conductance (resistance) in the parallel configuration is indeed lower (higher) than that in the anti-parallel configuration at low bias voltages, $|V_b| \leq 2$ mV, which results in negative MR switchings.

More interestingly, the MR also shows oscillatory behavior as a function of bias voltage. For example, the MR at the valley changes from negative to positive, and back to negative, with increasing bias voltage, as shown in Fig. 4.3 (b). Similar sign-changing oscillatory behavior of MR as a function of bias voltage is also observed at the conductance peak, where the sign of MR changes from positive to negative and then to positive again as bias voltage increases, as shown in Fig. 4.3 (c). At higher bias voltages, the amplitude of MR switchings decreases and eventually diminishes to zero at $|V_b| \geq 20$ mV. Finally, the shapes of both positive and negative MR oscillations are symmetric around the zero bias voltage.

To summarize, the three distinctive MR features observed in the previous gate voltage measurements, (i) in-phase oscillations, (ii) negative MR at conductance valley, and (iii) the symmetric MR shapes, have also been observed in the bias voltage measurements.

4.3.3 Data Analysis with a Two-Channel Model

In the single-channel FP interference model proposed by Man *et al.* [37], the conductance (G) through SWCNTs is represented by a non-interacting single-channel wave guide model [35] :

$$G = \frac{2e^2}{h} \sum_{\sigma,\sigma' \in (+,-)} T_{\sigma,\sigma'}, \;\; T_{\sigma,\sigma'} = \frac{T_L^{\sigma} T_R^{\sigma'}}{|1 - \sqrt{(1 - T_L^{\sigma})(1 - T_R^{\sigma'})} e^{i\delta}|^2}, \tag{4.1}$$

where $T_{L,R}^{\sigma}$ represent the spin-dependent transmission probabilities at the left and right contacts as $T_{L(R)}^{\sigma} = T_{L(R)}(1 + \sigma\mathcal{P})$, with $\sigma = \pm 1$ depending on the relative spin

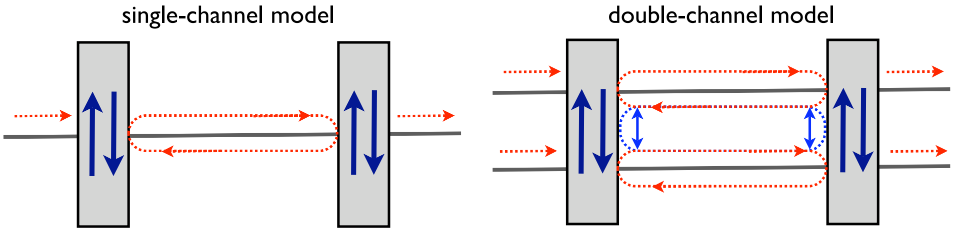

Figure 4.4: Schematic diagrams for (a) single-channel and (b) double-channel mixing FP models.

polarization $\mathcal{P}$ of electrodes, and δ is the control parameter varying as a function of gate and bias voltages.

Using this model, the in-phase MR modulation to the conductance oscillation can be observed under limited conditions, i.e., the transmission coefficients (T) at both metal contacts should be close to $\simeq 1$. Although the single-channel FP interference model illustrated in Fig. 4.4 (a) allows the in-phase behavior of MR, it fails to produce the negative values of MR at the conductance valley as shown in our data. The MR calculated with $G^P = (2e^2/h)\,(T_{+,+} + T_{-,-})$ and $G^{AP} = (2e^2/h)\,(T_{+,-} + T_{-,+})$ is only limited to MR $\geq 0\%$. Additionally, the single-channel FP model cannot account for the observed charge transport behaviors either. It has been experimentally demonstrated that certain current-voltage characteristics shown in the FP regime, such as a prominent conductance dip structure, cannot be explained by the single channel model [27]. Liang *et al.* found that the two conducting channels in metallic SWCNTs and the finite channel mixing between them, as shown in Fig. 4.4 (b), should be considered in data analysis in order to explain the observed FP interference effects in SWCNTs. Considering that the MR is highly correlated with FP interference effects and the negative MR occurs at the conductance valley, we have adopted the two-channel FP model to explain the observed spin-dependent transport behavior, especially negative MR switchings.

Following Ref. [27], we utilize the concept of the scattering matrix, S-matrix.

However, it is not trivial to include spin-dependent factors in the *spinless* S-matrix in the case where electrons are reflected by the spin-polarized electrodes. Naturally, the elements of S-matrix should depend on spins of both the incoming and outgoing electrons. If we neglect the spin scattering at the interface, spins should be conserved during reflections, and the spin-dependent S-matrix (S_σ) can be defined as

$$S_\sigma = \begin{bmatrix} \widehat{t}_\sigma & \widehat{r}'_\sigma \\ \widehat{r}_\sigma & \widehat{t}'_\sigma \end{bmatrix} \approx \exp\left(i \begin{bmatrix} \widehat{0} & \widetilde{r}_\sigma \\ \widetilde{r}^\dagger_\sigma & \widehat{0} \end{bmatrix} \right), \tag{4.2}$$

where $\widehat{t}$ ($\widehat{t}'$) is a 2×2 matrix describing the transmission form the left (right) side of the channel to the right (left) side, and $\widehat{r}$ ($\widehat{r}'$) is for the reflection at the left (right) side of the channel. In general, the spin-dependenence of the matrix elements of $\widehat{t}$, $\widehat{r}$ and hence S_σ is only accessible through detailed microscopic calculations.

Here, we propose the spin-dependent S_σ-matrix which is parameterized by a phenomenologically defined polarization fitting factor p, and barrier asymmetry α :

$$S_{\ell=(L,R),\sigma} = \exp\left(i\sqrt{\frac{1}{2}(1+\ell\alpha)(1+\sigma p)} \begin{bmatrix} \widehat{0} & \widetilde{r} \\ \widetilde{r}^\dagger & \widehat{0} \end{bmatrix} \right), \tag{4.3}$$

where $\ell = 1$ is for the left (L) and $\ell = -1$ for the right (R) barrier. The spin-dependent transmission coefficients at each electrodes can be calculated from the S-matrix by $T_{\ell,\sigma} = \mathrm{Tr}(\widehat{t}^\dagger_{\ell,\sigma} \widehat{t}_{\ell,\sigma})$, and barrier asymmetry α, and the polarization of electrode $\mathcal{P}_\ell$ are defined by

$$\alpha = \frac{T_L - T_R}{T_L + T_R}, \quad \text{where } T_\ell = \frac{T_{\ell\uparrow} + T_{\ell\downarrow}}{2}, \quad \mathcal{P}_\ell = \frac{T_{\ell\uparrow} - T_{\ell\downarrow}}{T_{\ell\uparrow} + T_{\ell\downarrow}}. \tag{4.4}$$

The total spin-dependent transmission coefficient $T_{tot} = \mathrm{Tr}(\widehat{t}^\dagger \widehat{t})$, and then spin-dependent conductance in Eq. (4.1) can now be calculated from the total matrix S_{tot} obtained from $S_{tot} = S_R \otimes S_{\mathrm{SWCNT}} \otimes S_L$ [66]. Here S_{SWCNT} represents the

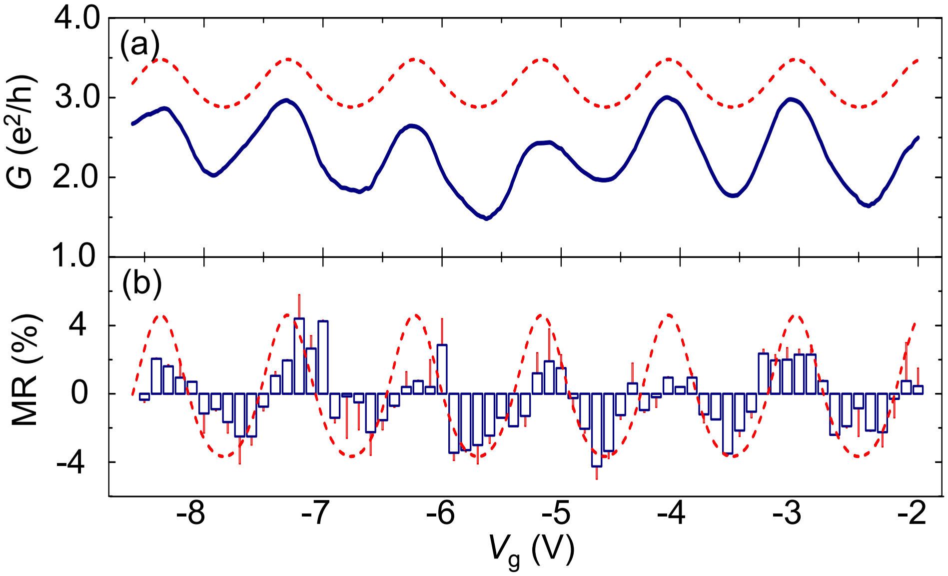

Figure 4.5: Numerical calculations based on the double channel mixing FP model. (a) Conductance oscillations as a function of V_g. Theoretical calculation is represented by red dotted line and experimental data by dark line. (b) Experimental data of gate-voltage-dependent MR (bar) and the calculated MR (red dotted line).

S-matrix inside of SWCNT without the electron scatterings between two modes :

$$S_{SWCNT} = \begin{bmatrix} e^{i\phi_1} & 0 & 0 & 0 \\ 0 & e^{i\phi_2} & 0 & 0 \\ 0 & 0 & e^{i\phi_1} & 0 \\ 0 & 0 & 0 & e^{i\phi_2} \end{bmatrix}, \tag{4.5}$$

where $\phi_{1,2}$ represents the phase accumulated by the electrons in the two transport modes, and can be expressed by a linear combinations of bias and gate voltages [27]:

$$\phi_{1,2} = \pm\left(\frac{eV_b}{\hbar v_F}L + \frac{\pi}{4}\frac{LC_LV_g}{e}\right). \tag{4.6}$$

Here C_L is the capacitance of nanotube per unit length.

Figures 4.5 (a) and (b) show the theoretical fitting results (red dotted lines) to the conductance and MR as a function of V_g, respectively, based on the proposed double-channel mixing FP model. The SWCNT channel length is considered as $L = 250$ nm, and $C_L \approx 16$ electrons / Vμm. In this fitting, the barrier asymmetry α is not considered in order to reduce the fitting parameters for simplicity. In fact, the effect from the barrier asymmetry does not affect the main MR features in the FP regime, and it is interesting to compare with its significant role in inducing negative MR in the Coulomb blockade regime [4]. The transmission coefficients used in this analysis are $T_{L(R),\uparrow} = 0.99$ and $T_{L(R),\downarrow} = 0.81$, and the calculated polarization is $\mathcal{P} = 0.10$. Using the model, all of the three distinctive features of MR are successfully reproduced. Primarily, the negative MR observed at the conductance valley is well reproduced.

Using a single set of control parameters used in the V_g fitting in Fig. 4.5, we can also obtain a reasonably good fitting of bias-voltage-dependence data sets both at the conductance valley ($V_g = -4.5$ V) and peak ($V_g = -3.9$ V), as shown in Fig. 4.6. Because the phase accumulation of transporting electrons is the linear function of both bias and gate voltage as shown in Eq. (4.6), it is not surprising that MR shows the same dependence on the bias and gate voltages.

We note that the proposed double-channel mixing model fails to reproduce quantitatively the conductance oscillations. The fitting results turn out to be consistently higher than the experimental data by up to $\Delta G \simeq 1.0\ e^2/h$, as shown in Fig. 4.5 (a) and Fig. 4.6 (a), (d). We speculate that series resistance at places other than the interface between SWCNTs and metals may be responsible for the difference.

The complexity of the MR features observed at large V_b cannot be accounted for by the double-channel model either. In Fig. 4.3, we can notice that the magnitude of MR is decreased as the applied voltage is increased, and the MR oscillation deviates from the conductance with an increasing bias voltage. More specifically,

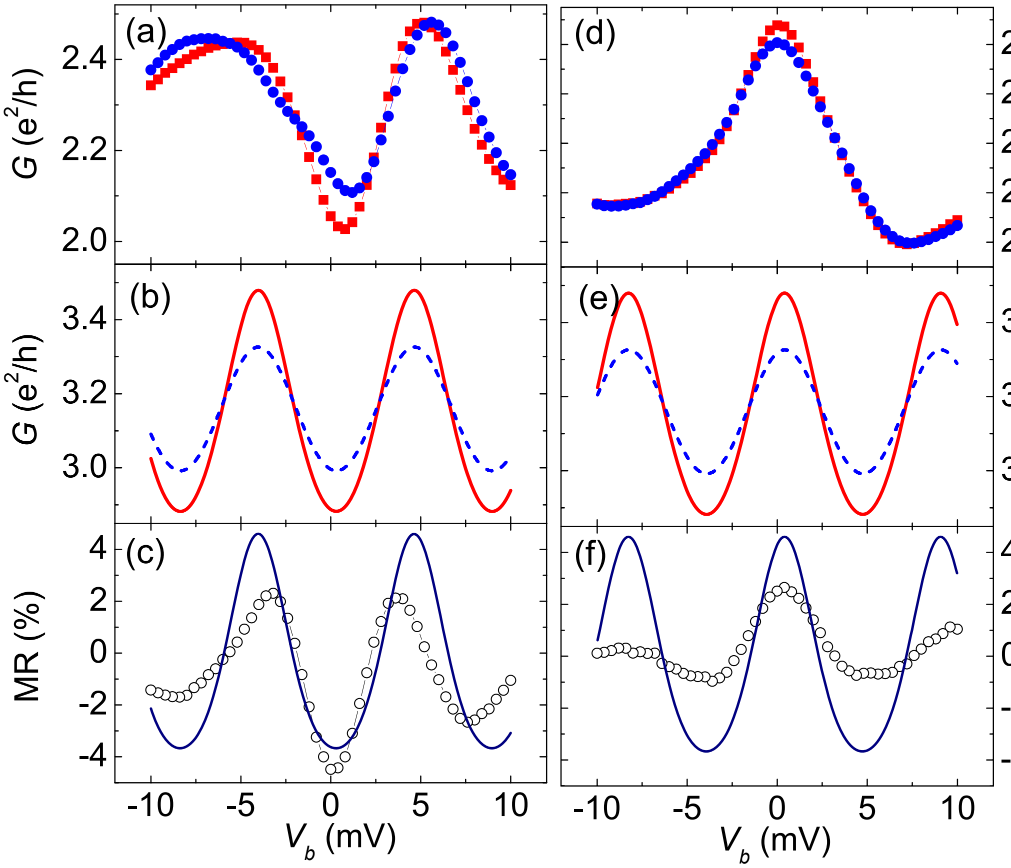

Figure 4.6: Numerical fitting results of V_b-dependent MR at the conductance valley (a,b,c) and peak (d,e,f). (a) and (c) are experimental data and the theoretical calculations for conductance oscillations in parallel (red) and anti-parallel (blue) configurations. (c) Experimental data of MR (open circles) and the calculated MR (solid line) at the conductance valley, $V_g = -4.5$ V. (d) and (e) are experimental data and numerical fitting result for the conductance, respectively, and (f) MR fitting at the conductance peak, $V_g = -3.9$ V. The same fitting parameters are used as in the gate voltage measurement.

MR is completely suppressed at $|V_b| \geq 20$ mV, and the bias voltage where the MR peak in Fig. 4.3 (b), and MR valley in Fig. 4.3 (c) occurs is reduced to ~ 3.5 mV from the voltage at the conductance peak and valley, ~ 6.9 mV.

The decrease of MR with increasing bias voltage has also been observed in the SWCNT FP resonator by Man *et al.* [37], and they suggested that the rapid decrease of the effective spin polarization of the ferromagnetic electrodes with increasing bias voltage might be the main reasons for the MR suppression [67, 68]. Even though this interpretation can be applied to our data, i.e., both the voltage at which the MR is completely suppressed, $|V_b| \geq 20$ mV and the effective polarization $\mathcal{P} \simeq 0.1$ in our sample are reasonably close to Ref. [37], the interpretation is not yet conclusive.

We speculate that the suppression of the FP interference effect is partly responsible for the MR decrease at large bias voltage in our device. As shown in the two-dimensional conductance plot in Fig. 4.3 (a), the FP interference patterns are getting suppressed as bias voltage increases. Thus, electron dephasing at larger bias could cause detrimental effects on the MR signals. Similar MR decrease due to the suppression of the quantum interference effect can be found in the temperature-dependent measurements.

Figure 4.7 shows two-dimensional conductance plots and separate MR traces at different temperatures. The crisscrossing FP interference patterns are still noticeable at $T = 10$ K, but barely recognizable at $T = 20$ K. As electrons in the SWCNT FP resonator are less and less influenced by the interference effect with increasing temperature, the amplitude of MR oscillations significantly decreases, even though the overall shape of MR traces follows the conductance oscillations. At $T \geq 20$ K, the MR is completely suppressed, and neither gate voltage dependence nor switching features are observed, which strongly suggests that the MR decay is indeed associated with the loss of quantum interference effect as the temperature increases.

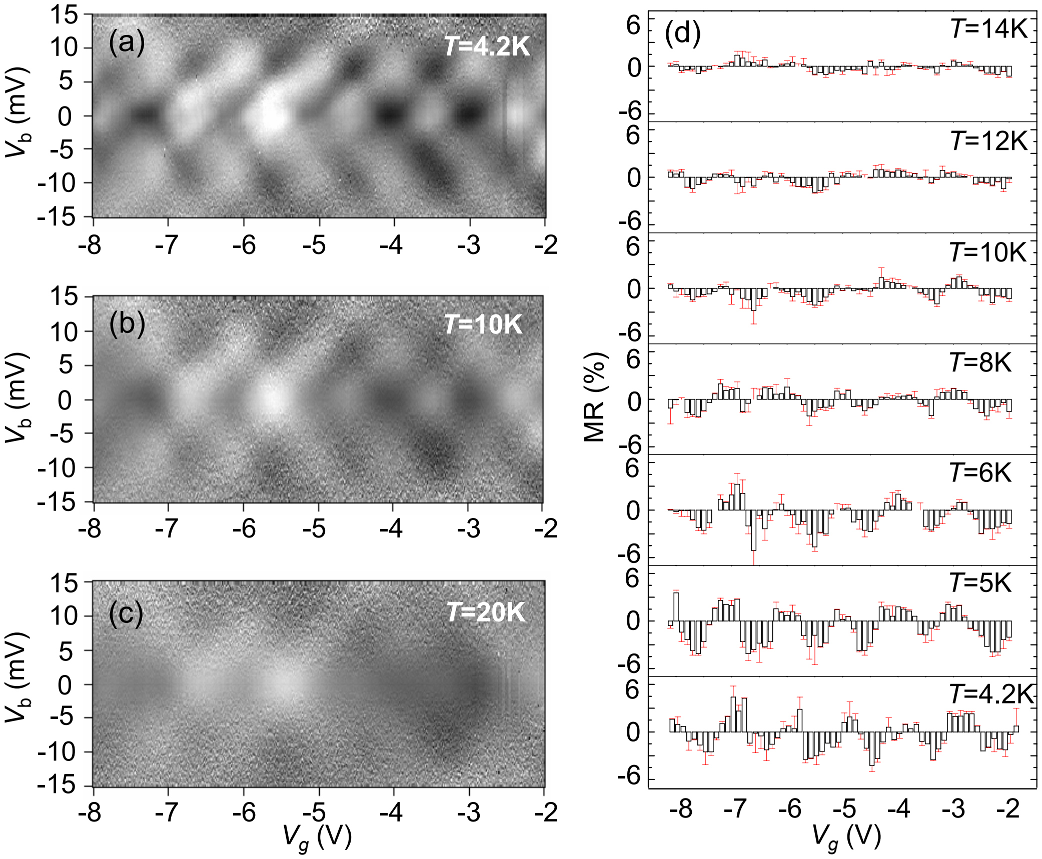

Figure 4.7: Two-dimensinal conductance plots as functions of both gate and bias voltage at (a) 4.2 K, (b) 10 K, and (c) 20 K. (d) MR traces as a function of gate voltage at zero bias at different temperatures.

4.4 Summary

In summary, we have measured spin-dependent transport in an individual SWCNT FP resonator contacted by highly transparent ferromagnetic electrodes. The in-phase relationship between MR and conductance oscillations, negative MR at the conductance valley, and the symmetric shape of MR traces are observed in both the gate and bias voltage measurements, and can be mostly understood by the double-channel FP model with channel mixing. The suppression of MR at larger bias and higher temperature suggests that spin-dependent transport in the SWCNT FP resonator is indeed correlated with the quantum interference effects.

Chapter 5

Kondo Effect in Ferromagnet-Contacted Single-Walled Carbon Nanotube

5.1 Introduction

Because of improved device fabrication technique, the realization of single electron transport in mesoscopic scale conductors is common nowadays. While underlying physical mechanisms of the Coulomb blockade and the Kondo physics observed in the quantum dots (QDs) contacted by normal electrodes are well understood, quantum transport in the presence of the superconductivity and ferromagnetism is rather unexplored. Especially, the Kondo physics under ferromagnetism has raised several interesting questions. The Kondo effect mainly arises from the anti-ferromagnetic interactions between conduction electrons in metal reservoirs and a localized electron spin inside QDs. Thus, the detailed spin information in both the electrodes and the QDs is crucial to Kondo-related transport. In the extreme case, the Kondo effect is expected to be fully suppressed when fully spin-polarized materials are utilized as metal electrodes, since one of electron spins is completely missing. In this situation, the anti-ferromangetic interactions are no more present. Therefore, it is interesting to know how the Kondo effect develops under the interaction with unbalanced electron spins in the ferromagnetic electrodes.

Actually, it has been theoretically argued [32, 33, 34] and experimentally demonstrated in C_{60} molecular system [69] that the Kondo effect can be persisted in ferromagnet-contacted QDs. Furthermore, zero-bias Kondo resonance peak can be split into two even without an external magnetic field, because of the exchange interactions between spin-polarized electrodes and QDs. In addition, negative magnetoresistance (MR), i.e., higher conductance (lower resistance) in the anti-parallel configuration than that in the parallel configuration, has been expected deep inside the Kondo regime at low bias voltages. Normal Kondo resonance peak is fully expected in the anti-parallel configuration, but the conductance at zero bias from the Kondo physics becomes smaller due to the splitted peaks in the parallel configuration.

In this chapter, we report new experimental observations related to the Kondo physics from individual single-walled carbon nanotube (SWCNT) contacted by ferromagnetic electrodes. To the best of our knowledge, our measurement is the first report on the Kondo effects observed in ferromagnet-contacted SWCNT. In contrary to theoretical expectations, the MR observed deep inside the Kondo valley is always positive at zero bias, i.e., higher resistance in the anti-parallel configuration than that in the parallel, and it features in-phase evolution, i.e., the MR peak occurs at the conductance peak, as a function of bias voltage. The strong Kondo effect combined with weak ferromagnetism, which may be attributed to the small polarization of electrodes, can explain our observations. In addition, we observe out-of-phase MR oscillations (i.e., the MR dip coincides with conductance peak) and particle-hole symmetry features at the edges of Kondo ridges or in the so called mixed valence regime.

5.2 Magnetoresistance in the Kondo Regime

Figure 5.1 (a) shows an atomic force microscopy (AFM) image of one of our devices. The overall process for device fabrications is identical to that described in Chapter 4. Figure 5.1 (b) shows the two-dimensional conductance plot as a function of gate V_g and bias voltage V_b at $T = 4.2$ K. We can clearly see three alternating zero-bias Kondo resonance features of the conductance within the measured gate voltage range of $1 \text{ V} \leq V_g \leq 5$ V. In between the Kondo regimes, the conductance is strongly suppressed while the conductance is significantly enhanced along the Kondo ridges (around $V_g \sim 1.9$ V, $V_g \sim 3.7$ V, and $V_g \sim 4.6$ V, respectively). The Coulomb blockade occurs due to the strong Coulomb repulsion when the QD is occupied by even number of electrons. In contrast, the Kondo ridges are attributed to the interplay between the strong electron-electron correlation and the localized magnetic moment in the QD when the QD is occupied by an odd number of electrons [70, 71]. As presented in Fig. 5.1 (c), the resonance peak measured at $V_g \simeq 3.7$ V with different temperatures can be fitted to an empirical expression [31] :

$$G(T) = G_o \left(1 + (2^{-s} - 1)(T/T_K)^2\right)^{-s}, \tag{5.1}$$

where s is an asymptotic value equal to 0.22 for a spin $\frac{1}{2}$ system, and the Kondo temperature, T_K, can be obtained from the fitting. From the well-matched fitting, we can confirm that the resonance feature at $V_b = 0$ is indeed related to the Kondo physics. In addition, T_K can also be estimated from the full width at half maximum (FWHM) of the Kondo resonance peak by FWHM $\approx 2k_BT_K/e$ [30]. The extracted T_K in the first Kondo ridge ($V_g \sim 1.9$ V) is ~ 14 K, and ~ 16 K for the second Kondo ridge ($V_g \sim 3.7$ V).

MR measurement is done by sweeping an external magnetic field from 200 mT to -200 mT (negative sweep), and from -200 mT to 200 mT (positive sweep)

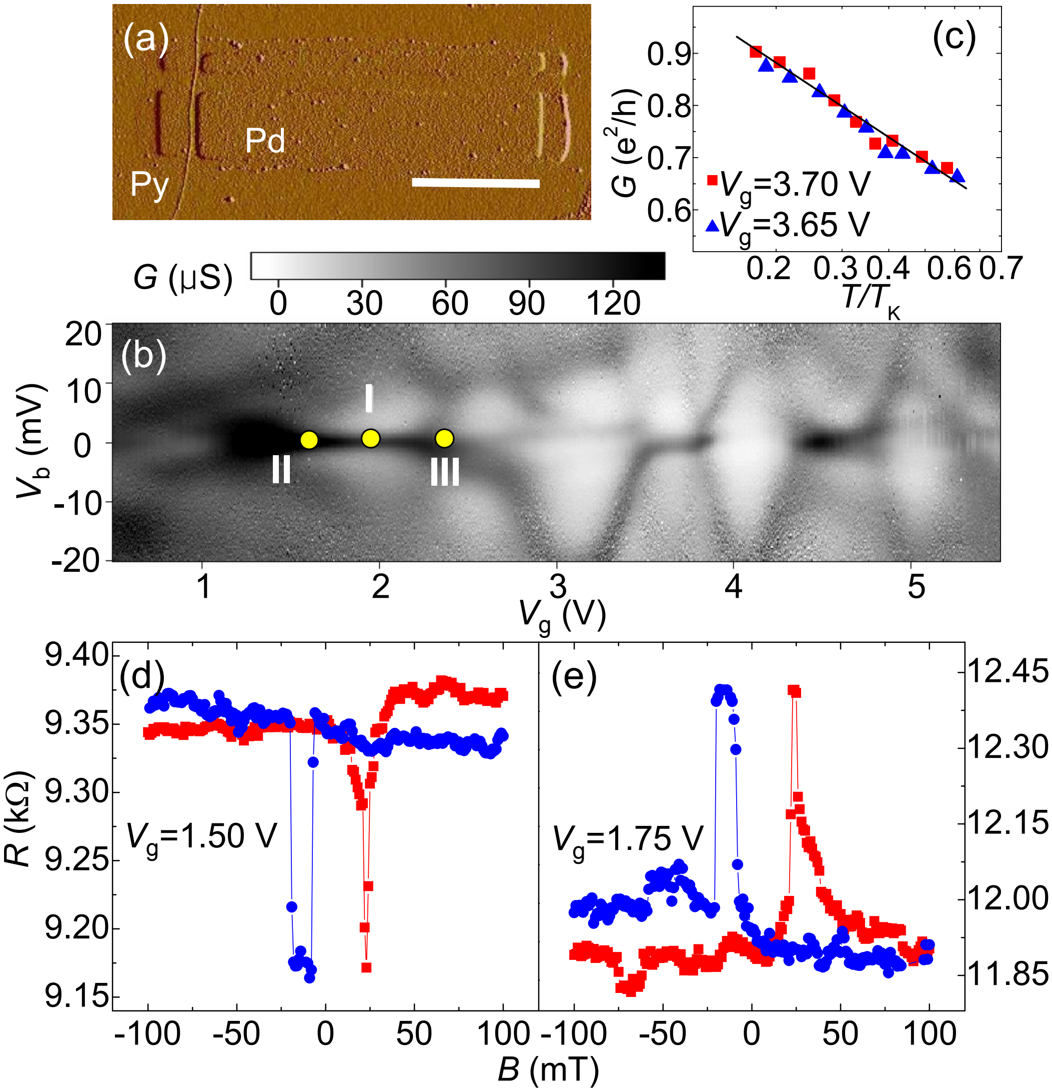

Figure 5.1: (a) AFM image of a representative device. The scale bar corresponds to 1 μm . (b) Two-dimensional conductance plot as a function of bias and gate voltage at T = 4.2 K. The gate voltage deep inside the Kondo valley is denoted as **I** and the two edges of Kondo valley as **II** and **III**. (c) Conductance vs normalized temperature measured at the second Kondo valley, $V_g \sim 3.7$ V. (d),(e) Representative negative and positive MR switching as a function of external magnetic field measured at **II**, $V_g = 1.50$ V and inside Kondo valley at **I**, $V_g = 1.75$ V, respectively.

at fixed gate and bias voltages. The MR is defined by MR $= (G^P - G^{AP})/G^{AP} = (R^{AP} - R^P)/R^P$, where G^P (G^{AP}) is the conductance in the parallel (anti-parallel) configurations of ferromagnetic electrodes and the resistance is $R^P = 1/G^P$, and $R^{AP} = 1/G^{AP}$. By repeating the same measurement at varying gate and bias voltages, we can monitor gate-voltage and bias-voltage dependent MR.

Although the zero-bias conductance peak prevails over the whole Kondo ridge, the detailed transport mechanisms are different at the center marked as **I** and the two ends of the Kondo ridge marked as **II** and **III** in Fig. 5.1 (b). While the pure Kondo effect governs the transport at the center, more contributions come from the single-electron resonance near the ends of the Kondo ridge, which are called mixed-valence regimes [70, 71]. Indeed, the different transport mechanisms give opposite MR behavior in the mixed valence regime and the deep Kondo regime, i.e., the MR switching is negative in the mixed valence regime as shown in Fig. 5.1 (d), but changes to positive in the deep Kondo regime as shown in Fig. 5.1 (e). This difference will be seen and discussed in greater detail below.

We first investigate the deep Kondo regime, i.e., at the centers of the Kondo ridges. Figure 5.2 (a) and (b) show the conductance and MR modulations as a function of gate voltage over the first and second Kondo ridge, respectively. The conductance and MR curve along the third Kondo ridge ($V_g \sim 4.6$ V) exhibit similar feature. Figure 5.2 (b) and (d) show the resonant conductance peaks in the parallel (closed circles) and anti-parallel (open circles) configurations along with MR (open diamonds) modulations as a function of bias voltage in the first ($V_g = 1.9$ V) and the second ($V_g = 3.65$ V) Kondo ridges, respectively.

MR measured in the Kondo regimes reveals four interesting properties: (i) The Kondo effect still survives and gives rise to well-defined zero-bias conductance peaks even in the parallel polarizations of the electrodes. (ii) The MR is relatively small (MR $\leq 4\%$), and (iii) its sign is positive. (iv) The MR and conductance

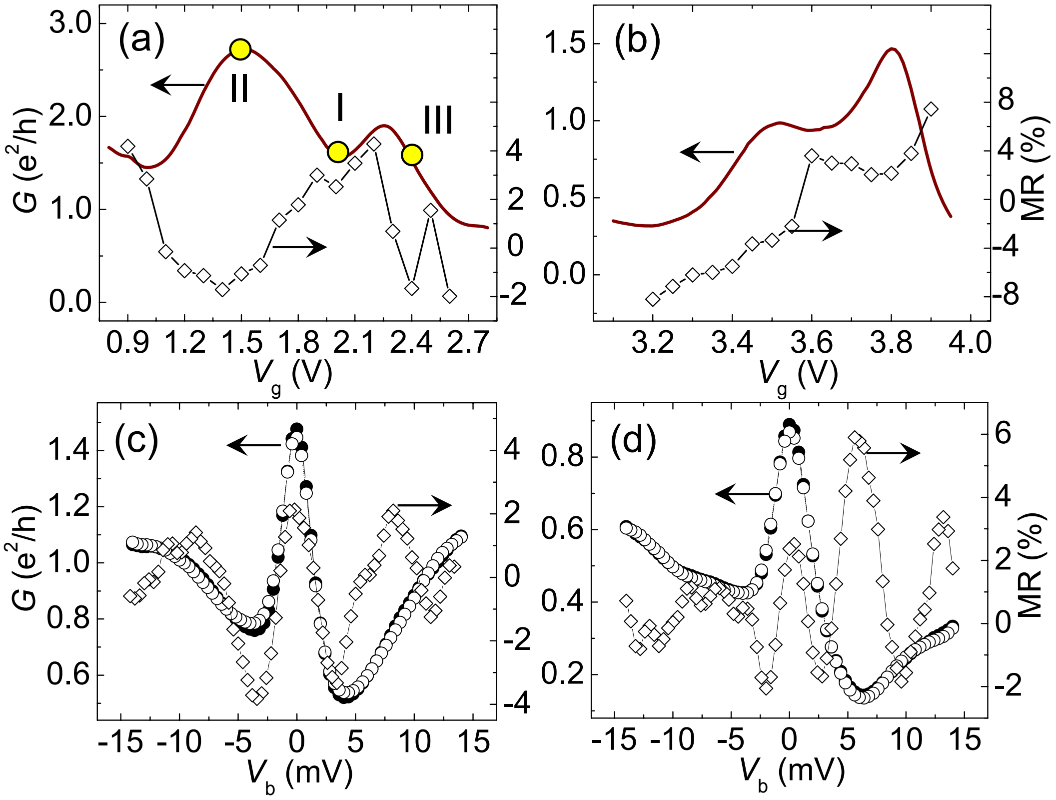

Figure 5.2: (a),(b) Conductance and MR as a function of gate voltage in the first and second Kondo regions, respectively. (c) Conductance and MR modulations as a function of bias voltage measured deep inside the Kondo valley, $V_g = 1.9$ V. Closed and open circles represent the Kondo resonance conductance peaks in the parallel and anti-parallel configurations, respectively. Open diamonds represent the MR. (d) Same measurement as (c) at the second Kondo valley, $V_g = 3.65$ V.

oscillations exhibit the in-phase behavior, i.e., the MR peaks occur at the peaks of conductance as shown in Fig. 5.2 (c) and (d).

Properties (i), (ii) and (iii) are contrasts to a hasty expectation based on the recent theoretical predictions [32, 33, 34] and experimental demonstration [69]. In those systems, the suppression of the Kondo effect in the parallel configurations is expected to lead to large negative MR. MR feature (i) and (ii) can be accounted for by the relatively small polarization of ferromagnetic electrodes, and detailed discussion will be made below. However, features (iii) and (iv) are non-trivial. Below, we will demonstrate that the positive MR and in-phase behavior of the MR and conductance curve are another unique features of the Kondo effect in the presence of small polarization based on simple theoretical arguments.

To understand the spin-dependent transport through the device, we need to consider the effect of the effective Zeeman splitting from ferromagnetic electrodes. There can be several sources of the effective Zeeman splitting. They are summarized by the equation of $\Delta_Z = \Delta_{\text{ext}} + \Delta_{\text{SDIPS}} + \Delta_{\text{corr}}$. Δ_{ext} comes from the externally applied magnetic field including the stray field directly from the ferromagnet electrode. The almost flat background modulation shown in Fig. 5.1 (d) and (e), which is maintained up to ±400 mT, is a strong indication that the stray-field effects are negligible in our device. Δ_{SDIPS} arises from the spin-dependent phase shifts across the spin-active interfaces [4, 72, 73]. It is not simple to estimate Δ_{SPIPS}, and there is no rigorous theoretical model for Δ_{SDIPS} in SWCNT/ferromagnet contacts. Only a toy model has been proposed [48]. However, the almost symmetric MR shapes shown in bias voltage dependence suggests that the effect from Δ_{SDIPS} is small in the deep Kondo regime in our device. Finally, Δ_{corr} comes from the different kinetic energy gains (uncertainty principle) for two spin components with different hybridization with conduction bands in the electrodes [32, 34, 74]. Δ_{corr} vanishes in the absence of the strong Coulomb interaction, and is a manifestation of the interplay between the strong electron-electron correlation and the quantum fluctuations of charge. We believe that in the Kondo regime of our sample, the effective Zeeman splitting comes mainly from Δ_{corr}.

According to the scaling theory [34, 75], $\Delta_{\text{corr}} \approx (\mathcal{P}_L\Gamma_L + \mathcal{P}_R\Gamma_R)\log(\epsilon_d/D)$, where ϵ_d is the QD energy-level position, and D is the width of the conduction band of the electrodes. The polarization of ferromagnetic electrode $\mathcal{P}_L$ and $\mathcal{P}_R$ can be defined by $\mathcal{P}_{L(R)} = (\Gamma_{L(R),\uparrow} - \Gamma_{L(R),\downarrow})/(\Gamma_{L(R),\uparrow} + \Gamma_{L(R),\downarrow})$. Here $\Gamma_{L(R),\sigma}$ ($\sigma =\uparrow,\downarrow$) is the spin-dependent hybridization of the QD level with the conduction band of the ferromagnetic electrodes $L(R)$. The spin-averaged total hybridization will be denoted by $\Gamma_0 = (\Gamma_L + \Gamma_R)/2$ with $\Gamma_{L(R)} = \Gamma_{L(R),\uparrow} + \Gamma_{L(R),\downarrow}$. With this, asymmetric coupling of the left (L) and right (R) ferromagnetic contact can be expressed by $\alpha = (\Gamma_L - \Gamma_R)\,/\,(\Gamma_L + \Gamma_R)$. Γ_0 indicates how well SWCNT QD is coupled to electrodes, and is manifested as the broadening of conductance peaks at the Coulomb blockade degeneracy points. In our device, it is found to be $\Gamma_0 \simeq 4.0$ meV.

We estimate for our sample $\Delta_{\text{corr}} \approx 10$ K at the largest mainly due to the small polarization of permalloy film. The polarization $\mathcal{P}_L \sim \mathcal{P}_R \sim 0.2$ of ferromagnetic electrodes is found from the theoretical fittings as discussed below, and is similar to $\mathcal{P} \sim 0.1$ extracted in the same device in the Fabry-Perot interference region as described in Chapter 4. The Kondo resonance peak can thus survive even in the parallel configuration because the strong Kondo effect associated with the large Kondo temperature ($T_K \approx 14$ K) overshadows the effective Zeeman splitting from the ferromagnetic electrodes. This is the main reason why the Kondo peak does not split even in the parallel configuration and the magnitude of MR is relatively small.

The explanation for the in-phase MR and positive switching features needs another attention to the Kondo physics. We first note that according to the Fermi liquid picture of the Kondo correlated state, the Kondo resonance peak can be

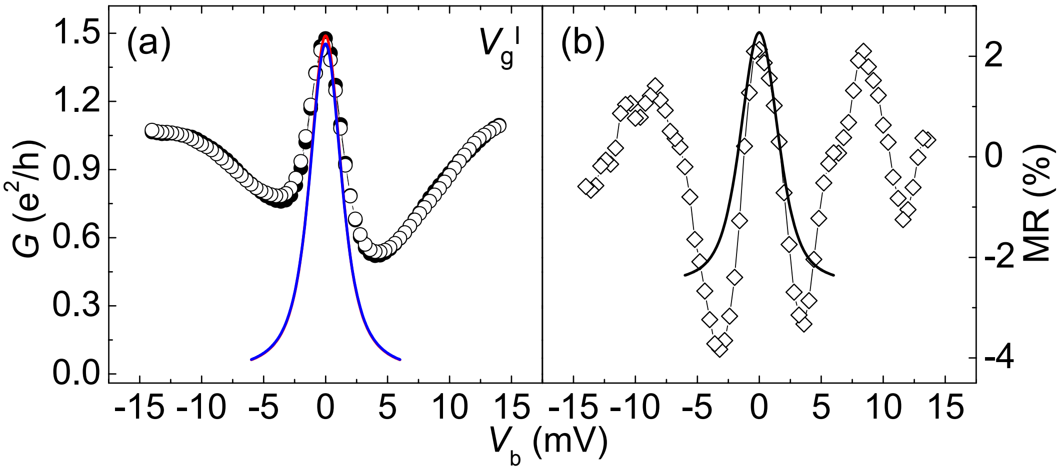

Figure 5.3: Theoretical fitting to both (a) conductance and (b) MR at labeled Kondo ridge, **I**.

regarded as a Lorentzian line shape centered at the Fermi energy and of width k_BT_K. In principle, this is valid only for $|eV_b|, k_BT \ll k_BT_K$. However, it turns out that it still holds even for finite T and V_b, up to $k_BT, |eV_b| \lesssim 10k_BT_K$, when the level broadening is replaced by the temperature-dependent effective broadening of the Kondo peak :

$$\Gamma_{\text{eff}}(T) = T_K'' \exp\left\{\frac{a\log(T/T_K'')}{1-\exp[-(a/b)\log(T/T_K'')]}\right\} . \tag{5.2}$$

Eq. (5.2) is merely an empirical model that can only be justified by fitting either to the experimental data or the numerical renormalization group calculations. Using fitting parameters $T_K'' \approx 0.728$, $a \approx 0.568$ and $b \approx 0.237$, Eq. (5.2) fits very well to the well-known empirical law of zero-bias conductance [31, 30]

$$G_{\text{emp}}(V_b = 0, T) = \left[\frac{(T_K')^2}{T^2 + (T_K')^2}\right]^{0.22} , \tag{5.3}$$

and the numerical renormalization group result [76]. Adopting this, the conductance is given by

$$G_\sigma(V_b, T) = -\frac{e^2}{h}\frac{4\Gamma_{L\sigma}\Gamma_{R\sigma}}{\Gamma_\sigma^2}\int dE\,\frac{f'(E)\Gamma_{\text{eff}}^2}{(E+eV_b)^2+\Gamma_{\text{eff}}^2} \tag{5.4}$$

Figure 5.3 (a) and (b) show the theoretical fitting results to the conductance and MR measured as a function of bias voltage in the first Kondo ridge, $V_g = 1.9$ V, based on the empirical model (5.4). Given only two fitting parameters; $\mathcal{P}_L = \mathcal{P}_R = \mathcal{P} = 0.2$ and $\alpha = 0.25$, both conductance and MR fittings agree well to experimental data. Based on the fitting, we can confirm that the in-phase and positive MR features observed deep inside the Kondo regime can again be explained by the weak ferromagnetism in the leads and the strong Kondo effects.

5.3 Mixed-Valence Regime

We next turn to the mixed-valence regime (the ends of the Kondo ridge). Even in the presence of strong Coulomb interaction, the electrons can tunnel into and out of the SWCNT QD freely if the chemical potential of the dot is aligned to the Fermi level of the leads (up to the level broadening Γ_0). Even though the conductance modulation as a function of bias voltage exhibits also a zero-bias resonance peak in this regime, the transport mechanism is completely different from that in the true (deep) Kondo regime. As pointed out before in Fig. 5.1 (d) and (e), the different transport mechanisms between the mixed-valence and the Kondo regimes lead to a completely different MR behavior. Here we investigate the difference in more detail with the bias-dependence of the MR as shown in Fig. 5.4. Figure 5.4 (a) and (b) show the conductance and MR modulation as a function of bias voltage, respectively, at end **II** of the first Kondo ridge. Figure 5.4 (c) and (d) are the same curves measured at the other end **III**. Comparing the conductance and MR curve, MR shows out-of-phase behavior with the conductance. More interestingly, the MR

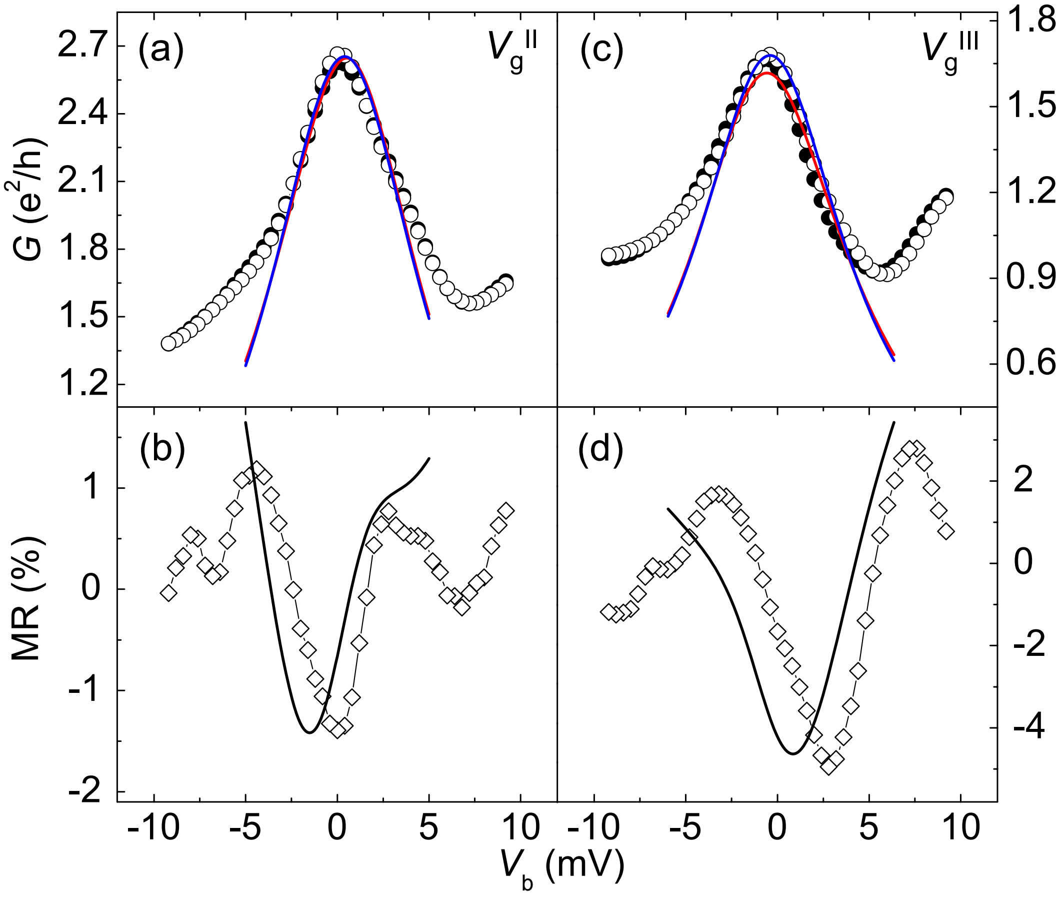

Figure 5.4: Theoretical fitting to conductance and MR in the mixed-valence regime, denoted as **II** and **III** in Fig. 5.2 (a). Fitting parameters are $\mathcal{P} = 0.2$ and bare coupling $\Gamma_o = 4.0$ meV. The asymmetric coupling $\alpha = 0.6$ is used for **II**, and $\alpha = 0.76$ for **III**.

shapes at the two opposite ends of the Kondo ridge are roughly mirror symmetric with respect to each other; i.e., the MR dip at end **II** is slightly shifted to the left, while the the MR dip at the opposite end **III** is shifted to the right relative to the corresponding conductance peak. Qualitatively similar mirror symmetric feature is also observed for the second Kondo ridge.

We first note that the out-of-phase behavior of the MR with respect to the conductance curve can be well understood by means of the Lorentzian approximation of the conductance peak [4],

$$G_\sigma(V_b,T) = -\frac{e^2}{h}\int dE\,\frac{4f'(E)\Gamma_{\mathrm{L}\sigma}\Gamma_{\mathrm{R}\sigma}}{(\epsilon_{\mathrm{d}\sigma}+eV_b)^2+(\Gamma_{\mathrm{L}\sigma}+\Gamma_{\mathrm{R}\sigma})^2}, \tag{5.5}$$

or more precisely by taking into account the Coulomb oscillations [73]. In Eq. (5.5), $\epsilon_{\mathrm{d}\sigma} = -\kappa_{\mathrm{g}} eV_{\mathrm{g}} + \sigma\Delta_{\mathrm{Z}}/2$, and κ_{g} is a constant proportional to gate capacitance.

The approximate mirror symmetric behaviors of the MR is related to the particle-hole symmetry. To see this, we can consider a toy model with a single localized level for which $\Delta_Z > 0$ and $\Gamma_\uparrow = \Gamma_\downarrow$. As the gate voltage tuned, the first conductance peak will arise at $\kappa_g eV_g = -\Delta_Z/2$, the main contribution to which comes from the tunneling of spin-↓ electrons. The transport of spin-↑ electrons is blocked by the large charging energy U. As the gate voltage is increased, the second conductance peak occurs at $\kappa_g eV_g = \Delta_Z + U$. The second peak is now dominated by spin-↑ electrons with the spin-↓ level completely occupied. The roles of the spin-↑ and ↓ electrons are exchanged near the two conductance peaks, and the conductance and hence the MR curve are mirror symmetric around the point $\kappa_g eV_g = U/2$. This can be argued more rigorously by making a particle-hole transformation for a single-impurity Anderson model. In our case,the conditions of $\Gamma_\uparrow \neq \Gamma_\downarrow$ ($\mathcal{P} \neq 0$) and $\Delta_Z = \Delta_{\mathrm{corr}}$ degrade the perfect mirror symmetry. However, qualitatively the argument above is still valid, and the conductance and MR bear an approximate mirror symmetry. Actually, the total effective Zeeman splitting Δ_{Z} at **II** and **III** should be different in sign. The fitting results shown in Fig. 5.4 agree reasonably with the data for both the conductance and MR. Here we used $\Delta_{\mathrm{Z}} = 0.15$ meV in Fig. 5.4 (a) and (b), and $\Delta_{\mathrm{Z}} = -0.22$ meV in Fig. 5.4 (c) and (d).

5.4 Summary

In summary, we have carried out spin-dependent transport measurements in an individual SWCNT contacted by ferromagnets. MR oscillations as a function of both gate and bias voltage are observed in both the Kondo and the mixed-valence regimes. Positive MR switching at zero-bias and in-phase MR evolution deep inside the Kondo ridges are explained by a Fermi liquid picture of the Kondo correlated state considering small electrode polarization and strong Kondo effect. The observed mirror symmetry in the mixed valence regime can be understood by the particle-hole symmetry.

Chapter 6

Magneto-Coulomb Effect in Ferromagnet-Contacted Single-Walled Carbon Nanotubes

6.1 Introduction

Ever since the pioneering work relating ferromagnetism to the single-electron charging effects was introduced by Ono *et al.* [77], several experimental platforms have been utilized over the last decade to investigate how the electron spins are correlated with the Coulomb blockade effect in this highly interacting system [4, 55, 69, 78, 79]. Among these, single-walled carbon nanotubes (SWCNTs) contacted by ferromagnetic electrodes have been considered as a promising system, not only because the spin decoherence due to the spin-orbit coupling is expected to be negligible, but also because the single-electron effects have been commonly observed and well understood in SWCNTs [4, 52, 80, 53, 54]. Actually, it has been demonstrated that spin transport through SWCNTs was influenced by the Coulomb blockade effect [4, 48], which caused magnetoresistance (MR) modulation as a function of gate voltage, and even sign reversal in MR, i.e., the positive and negative switchings as defined in the previous chapters [4, 55, 50]. However, it has been consistently argued that the MR observed in two-probe devices could be influenced and often overshadowed by several magnetic-field dependent mechanisms other than spin transport through SWCNTs [58, 57].

Out of several possible scenarios including anomalous magnetoresistance (AMR) [43], spin-Hall effects [59], and tunneling anisotropic magnetoresistance-like effects [60], the magneto-Coulomb effect (MCE), arising from unbalanced spin-dependent chemical potential of ferromagnetic electrodes under an external magnetic field [78, 81], has been suggested to explain the unexpected MR switchings in the SWCNT devices contacted by ferromagnet (FM) on one side and normal metal (NM) on the other (FM-SWCNT-NM) [54]. The presence of MR in the single FM contacted SWCNT cannot be understood by the spin accumulation and detection mechanism which requires two FM electrodes to control the spin transport through the SWCNTs [44, 82]. Molen *et al.* proposed that by incorporating MCE with the Coulomb blockade effect, the MR observed in the FM-SWCNT-NM device can be understood [58]. In the MCE, single FM is enough to change the transport behavior by inducing extra charges in the SWCNT quantum dots (QDs). More detailed discussions will be presented later in this chapter. They have further raised the questions that the reported MR especially in the Coulomb blockade regime [4, 55] could arise from the MCE, and not from the spin transport through SWCNTs.

Here, we report on the magnetic field dependence of electronic transport through FM-contacted individual SWCNTs in the Coulomb blockade regime. Several observed MR features can be accounted for by the MCE rather than spin accumulation and transport through SWCNTs. Among them are (i) exceptionally large MR switching, i.e., $|\mathrm{MR}| \geq 100\%$, (ii) the absence of symmetry features in the two- and four-fold Coulomb oscillations, (iii) MR sign change across the Coulomb oscillation peak, (iv) single-step staircase type MR switching, and (v) MR switchings in

NM-SWCNT-FM devices.

6.2 Magnetoresistance in the Coulomb Blockade Regime

We will first present the results observed from sample **A**, as shown in Fig. 6.1 (a) exhibiting exceptionally large MR switching. Figure 6.1 (b) displays the two-dimensional conductance plot as a function of gate and bias voltages measured at $T = 4.2$ K. As discussed in Chapter 2, the well defined Coulomb diamonds confirm that the charge transport mechanism shown here is the sequential tunneling through a small conducting island.

To explore the spin-dependent transport, we first ramp the magnetic field in the negative direction to -200 mT, which is large enough to align both FM electrode polarizations in the same direction. The differential resistance ($\partial V/\partial I$) is monitored with the magnetic field sweeping in the positive direction to 200 mT at a fixed gate voltage. The negative B-field sweep data are then taken while the magnetic field ramps down from 200 mT to -200 mT without changing the gate voltage. By performing the same measurements at different gate voltages, we can obtain the two-dimensional resistance plots across six consecutive Coulomb oscillations with the magnetic field sweeping in the positive and negative directions, as shown in Fig. 6.1 (c) and (d), respectively. The degeneracy points where adjacent Coulomb diamonds meet are displayed as dark blue strips.

As expected from typical spin devices in which a conduction channel is sandwiched by two ferromagnetic films, a resistance change is observed when the relative spin polarization of electrodes is switched from parallel to anti-parallel configuration at $B \sim 20$ mT for the positive B-field sweep, and $B \sim -22$ mT for the negative, or vice versa. As discussed in the previous chapters, an anti-ferromagnetic oxidization layer formed on top of the unprotected permalloy film may account for the different magnetic field ranges where the FM electrodes are aligned in the anti-parallel

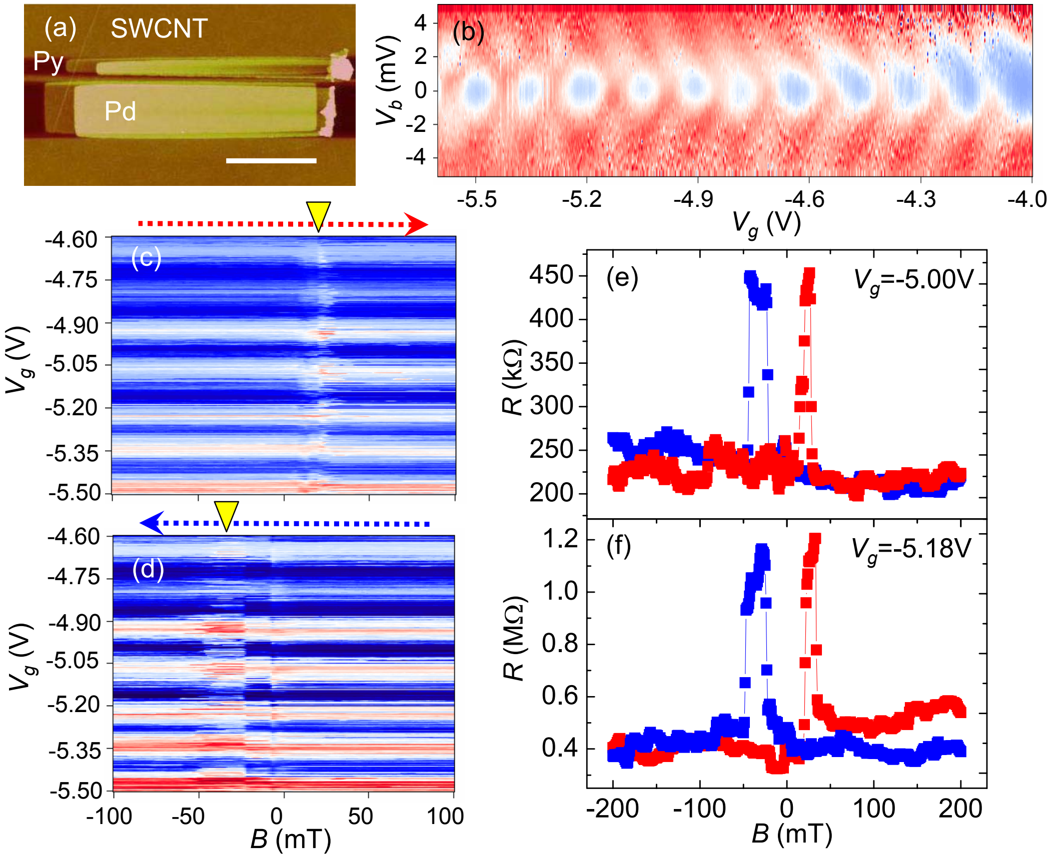

Figure 6.1: (a) Atomic force microscopy image of sample **A**. The scale bar is 1 μm. (b) Two-dimensional conductance plot as a function of gate (V_g) and bias (V_b) voltages at $T = 4.2$ K. (c), (d) Two-dimensional MR traces across six consecutive Coulomb oscillations with magnetic field sweeping in the positive and negative direction, respectively. The dotted arrows represent the magnetic field sweep directions and reversed triangles indicate the regions where the relative spin polarization of FM electrodes is anti-parallel. (e), (f) Representative positive MR traces at different gate voltages.

configuration [42].

Surprisingly, the MR calculated by the previously defined equation in Chapter 4, i.e., MR $= (R^{AP} - R^P)/R^P = (G^P - G^{AP})/G^{AP}$, where $R^{AP}(G^{AP})$ and $R^P(G^P)$ are resistance (conductance) measured in the anti-parallel and parallel configurations, respectively, shows exceptionally large switching, $\sim 100\%$, at certain gate voltages. MR across an individual Coulomb peak is oscillating in between -30% and 120%, and the MR deep inside the Coulomb blockade regime usually shows large switchings around $\sim 100\%$. Similar behavior is observed across all the six individual Coulomb oscillations. For instance, the MR at $V_g = 5.00$ V is about $\sim 90\%$ as shown in Fig. 6.1 (e), and is $\sim 120\%$ at $V_g = 5.18$ V in the next Coulomb blockade region, as shown in Fig. 6.1 (f). Previously, MR switching close to $\sim 60\%$ has been observed in multi-walled carbon nanotubes (MWCNTs) contacted by perovskite manganite $La_{0.7}Sr_{0.3}MnO_3$ (LSMO), where the large MR switchings can be attributed to the large spin polarization, $\mathcal{P} \simeq 1$ of the LSMO electrodes [52]. However, the extraordinarily large MR switchings are not expected in our permalloy (Py, $Ni_{81}Fe_{19}$)-contacted SWCNTs considering that the spin polarization of the Py film is estimated to be $\mathcal{P} \leq 0.2$ from previous measurements in the Fabry-Perot (Chapter 4) and Kondo regimes (Chapter 5). It has been theoretically expected that the value of MR switching is enhanced in the Coulomb blockade regime because of the higher order tunneling events deep inside the Coulomb blockade regions [83]. However, the expected MR enhancement is not large enough to account for our observations.

6.3 Magnetoresistance in the Presence of Two- and Four-Fold Coulomb Oscillations

Another interesting MR behavior is observed in sample **B** exhibiting the intrinsic quantum energy level structures of SWCNTs. It is well known that SWCNT QDs made of metallic nanotubes possess a four-fold degeneracy because of the two $K-K'$ orbital structures in SWCNTs and the spin-up and spin-down degeneracy [23]. This four-fold symmetry features were first observed by Liang *et al.* and explained by the shell filling model nicely [84]. It has also been observed that the four-fold degeneracies are sometimes transformed into two-fold symmetry features when the orbital degeneracy is lifted [85, 86]. The detailed spin configurations of the QD energy states for two- and four-fold Coulomb oscillations can be determined by the evolution of Coulomb peaks in high magnetic field measurements. For example, the spin of the electron which is responsible for each Coulomb peak within a two-fold oscillation group should be alternating between spin-up ($\uparrow$) and spin-down ($\downarrow$) because of the Pauli-exclusion principle. Within a four-fold symmetry group, it is not straightforward to assign the electron spin for each Coulomb peak. The quantum energy state for each Coulomb peak is decided among the four states $\{\circlearrowleft\uparrow, \circlearrowleft\downarrow, \circlearrowright\uparrow, \circlearrowright\downarrow\}$ depending on several parameters: the charging energy E_c, the quantum energy-level spacing ΔE, the subband mismatch δ, the exchange energy J, and the excess Coulomb energy dU [86]. Here, counterclockwise ($\circlearrowleft$) and clockwise ($\circlearrowright$) rotations represent the orbital degeneracy of SWCNTs. Among the four available states, two are for the spin-up electrons, and the rest two for the spin-down electrons. Since the quantum energy-level for spin-up and spin-down electrons are shifted to opposite directions due to the exchange interaction between the FM electrodes and the QD, MR across the two- and four-fold Coulomb oscillations is expected to reveal the particle-hole symmetry feature with respect to corresponding Coulomb peak, as shown in the mixed-valence regime in Chapter 5 [73].

Figure 6.2 (a) shows a two-dimensional conductance plot of sample **B** as a function of gate and external magnetic field measured at $T = 1.7$ K. The direction of the B-field sweep is negative, i.e., from $B = 200$ mT to $B = -200$ mT. In the measured gate voltage range, the twelve Coulomb oscillations can be grouped

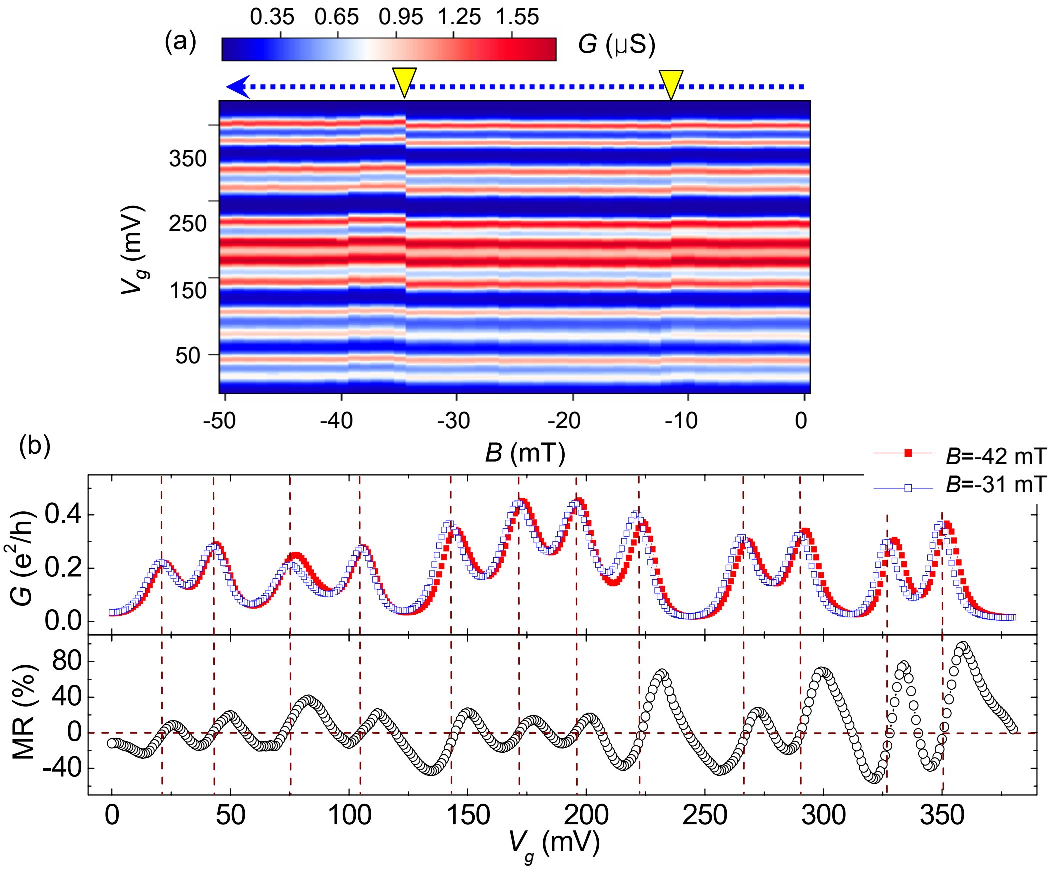

Figure 6.2: Sample **B** exhibiting both two-fold and four-fold symmetry features. (a) Two-dimensional conductance plot as a function of gate voltage with the magnetic field sweeping in negative direction. (b) Conductance and corresponding MR modulation as a function of gate voltage. Red closed and blue open squares represent the conductance in the parallel ($B = -42$ mT) and anti-parallel ($B = -31$ mT) configurations, respectively. Dark dotted lines are used to indicate where MR changes sign.

into two or four oscillations depending on the V_g-spacing between adjacent Coulomb peaks, as seen also in the upper half of Fig. 6.2 (b). As discussed above, the electron spin within a two-fold oscillation group is alternating between spin-up and spin-down, the MR is expected to the show the particle-hole symmetry feature.

When the B-field is ramped in the negative sweep direction from 200 mT, the polarization of the wider (easy) electrode is switched first at $B_{c1} \simeq -12$ mT, which results in the anti-parallel spin polarization of FM electrodes. Two FMs are aligned in the parallel configuration again when the polarization of the narrower (hard) electrode is switched at $B_{c2} \simeq -34$ mT. The coercive fields (B_c) for both FMs are indicated by the inverted yellow triangles in Fig. 6.2 (a). Representative conductance modulations in the anti-parallel ($B = -31$ mT) and parallel ($B = -42$ mT) configurations are plotted as blue open squares and red closed squares, respectively, in Fig. 6.2 (b).

Interestingly, the whole conductance oscillations are shifted uniformly in one gate voltage direction when one of FMs changes its polarization, as shown in the conductance plots in Fig. 6.2 (a) and (b). The conductance oscillations are shifted from those at $B = -11$ mT (parallel configuration) by $\Delta V_g \sim -2$ mV when the polarization of the easy electrode is switched at $B_{c1} = -12$ mT. Conductance modulations are shifted back by $\Delta V_g \sim 3.5$ mV from the oscillations at $B = -33$ mT (anti-parallel configuration) when the hard electrode changes its polarization at $B_{c2} = -34$ mT. Because of the uniform gate voltage shift of conductance oscillations, the conductance in the anti-parallel configuration is bigger than that in the parallel configuration at the left side of each Coulomb peak. On the other hand, the conductance in the parallel is bigger than that in the anti-parallel configuration at the right side of Coulomb peak. Thus, as shown in Fig. 6.2 (b), the MR across the each Coulomb peak looks similar for all measured twelve peaks, and the MR changes its sign across the individual Coulomb peak. The dark dotted vertical lines in Fig. 6.2 (b) show where the MR sign is reversed, and they are coincided with conductance peaks. In addition, the MR as large as $\sim 100\%$ is also observed at $V_g \simeq 360$ mV.

New intriguing MR features are observed from sample **B** when the gate voltage is in the range of -900 mV $\leq V_g \leq -300$ mV. Figure 6.3 (a) shows the two-dimensional conductance plots in negative and positive B-field sweep directions measured at $T = 4.2$ K. In this V_g range, there exist four well-defined four-fold symmetry groups of Coulomb oscillations. Interestingly, the switching induced from the hard electrode at B_{c2} is more pronounced than that from the easy electrode at B_{c1}. In the negative B-field sweep direction, all of the sixteen consecutive Coulomb oscillations are shifted in the negative gate voltage direction by $\Delta V_g(B_{c2}) \sim -6$ mV at $-B_{c2} = -32$ mT. They are shifted in the positive gate voltage direction by $\Delta V_g(B_{c2}) \sim 4$ mV at $B_{c2} = 32$ mT in the positive B-field sweep. Accordingly the MR switchings observed in this V_g-range are primarily determined by the spin polarization of the hard electrode and its reversal, not by the relative spin configurations (i.e parallel or anti-parallel) of both easy and hard FMs. This staircase-type single-step MR switching is more conspicuous in the separate MR line traces at a fixed gate voltage, as shown in Fig. 6.3 (b) and (c). The direction of MR switching at B_{c2} depends on whether the gate voltage is to the left or to the right of the Coulomb peaks. Similar single-step MR switching has been also observed in several other two-probe SWCNT devices measured in the Coulomb blockade regime.

Figure 6.4 (a) shows a two-dimensional conductance plot as a function of bias voltage in the same gate voltage range as in Fig. 6.3 at $T = 2.1$ K, and Fig. 6.4 (b) and (c) display both conductance and MR oscillations across the four groups of four-fold Coulomb oscillations measured during the positive and negative B-field sweeps, respectively. The closed red squares represent the conductance in the parallel configuration ($B = \pm 40$ mT), and the open blue squares for the Coulomb

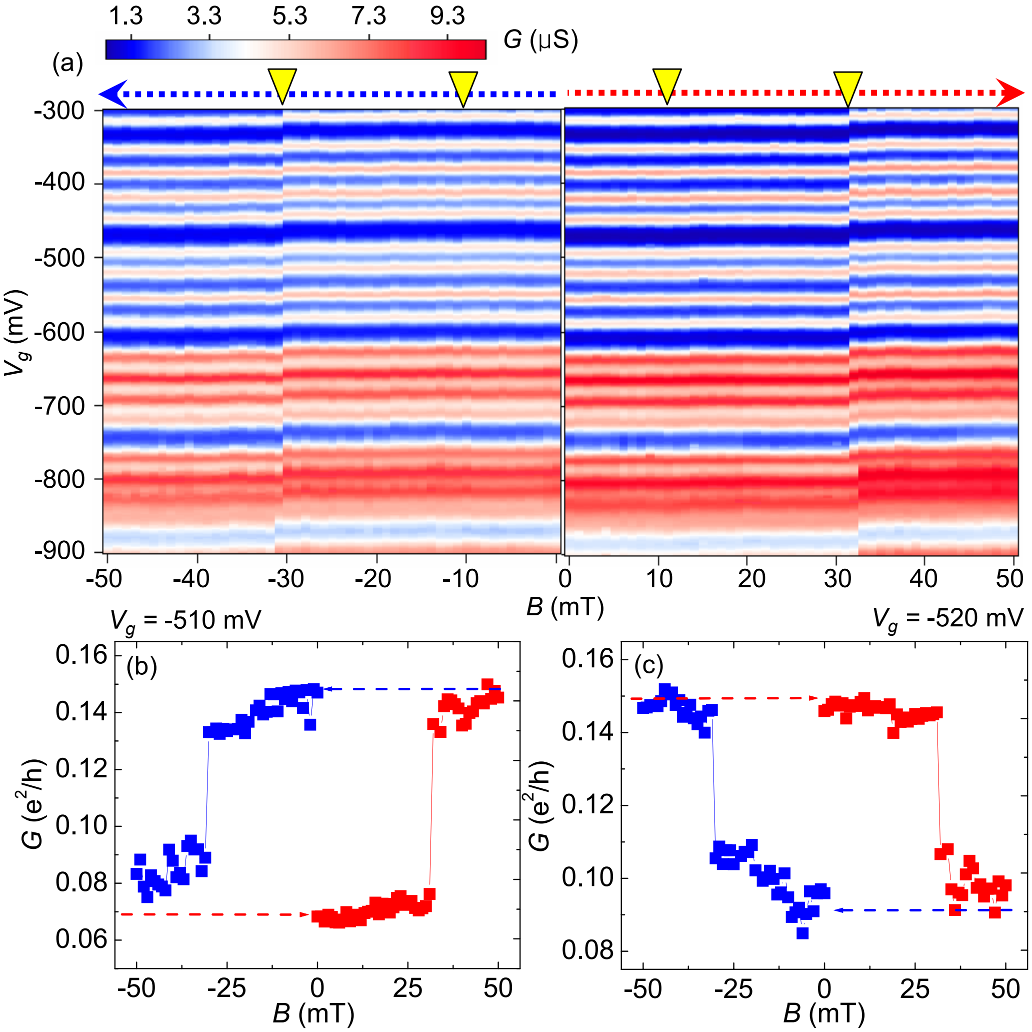

Figure 6.3: (a) Two dimensional conductance plots as a function of both gate and magnetic field measured at $T = 4.2$ K. (b), (c) MR traces as a function of magnetic field in the positive (red closed squares) and negative (blue closed squares) B-field sweep direction at $V_g = -510$ mV and $V_g = -520$ mV, respectively.

oscillations measured in the anti-parallel configuration ($B = \pm 20$ mT). Because of the single-step switching, MR modulations in the positive and negative B-field sweep directions show an opposite behavior. The positions where MR dips occur are to the left side of the Coulomb peaks in the positive sweep, but they are switched to the right side of the Coulomb peaks in the negative sweep direction. A couple of other distinctive MR features including the MR sign change across Coulomb peaks, and the large MR change as described earlier are also noticeable in this set of data.

6.4 Magneto-Coulomb Effect

Here, we claim that the exceptional MR features including (i) large $\sim 100\%$ MR change, (ii) the absence of particle-hole symmetry in two- and four-fold Coulomb oscillations, (iii) MR sign change across conductance peaks, and (iv) single-step MR switchings, observed from the FM contacted two-probe SWCNT devices can be all accounted for by the MCE as proposed by Ono *et al.* [78]. Recently, Van der Molen *et al.* theoretically showed that the MR sign changes at Coulomb oscillation peaks could be explained by the MCE along with the MR switching features in FM-SWCNT-NM devices [58]. In addition, they claimed that the amount of MR switching is determined by the strength of the Coulomb blockade, i.e., the sharper the Coulomb peaks are, the larger the maximum conductance changes, so the MR switching exceeding $\sim 100\%$ could be possible from the MCE. Besides these, we propose that our new experimental observations of the absence of symmetry features and single-step switching can also be explained by the proposed MCE model. In the following, we present a brief physical picture of the MCE and explain the absence of electron-hole symmetry features and single-step MR switchings observed in our devices within the concept of MCE.

Because of the asymmetric density of states and the lifting of spin-up and spin-down electron degeneracy under an external magnetic field at the Fermi level,

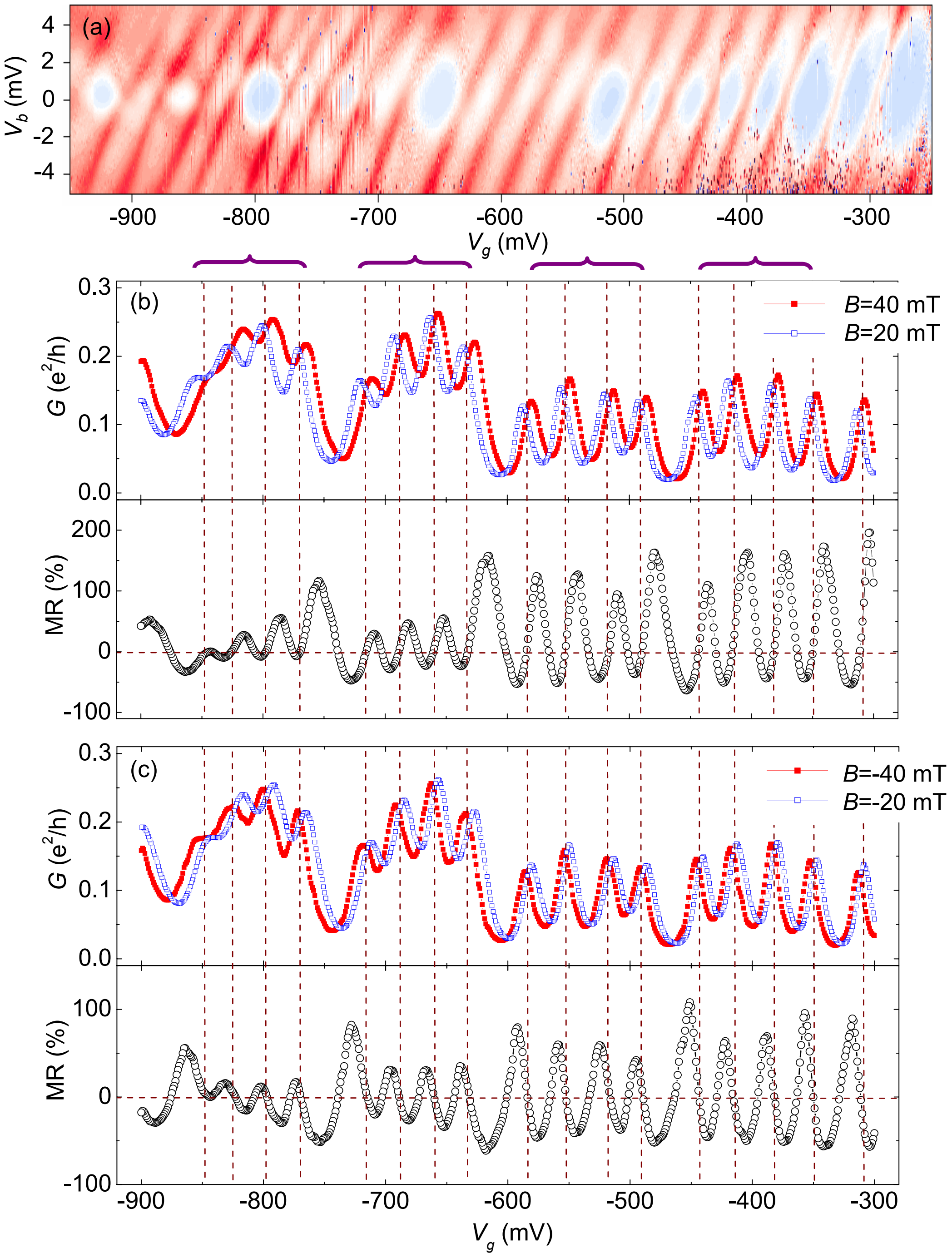

Figure 6.4: (a) Two-dimensional conductance mapping as a function of bias and gate voltage at $T = 2.1$ K. (b),(c) Representative conductance oscillations in the parallel (closed red squares) and anti-parallel (open blue squares) ferromagnet polarizations and the corresponding MR modulations in the positive and negative B-field sweep directions, respectively. Dotted dark lines are used to show where MR sign change.

the additional chemical potential $\Delta\mu$, which is equivalent to a potential difference ΔV, is developed in the FM electrodes :

$$\Delta V = \frac{\Delta\mu}{e} = -\frac{1}{2e}\mathcal{P} g \mu_{\mathrm{B}} B. \tag{6.1}$$

Here, g is the gyromagnetic ratio and μ_{B} is the Bohr magneton. For MCE, the polarization $\mathcal{P}$ is a quantity defined by the density of states for spin-up and spin-down electrons in the d band at the Fermi level, so it is significantly different from the polarization extracted from tunneling experiments, in which the spin-polarized tunneling electrons are mainly from the s-d hybridized bands [78, 81]. For example, the polarization for Ni electrodes is around $\mathcal{P} \simeq 0.8$, and $\simeq 0.6$ for Fe [81]. On the other hand, the polarization of pure Ni and Fe films measured from the tunneling experiments is limited to ≤ 0.4 [40].

Since the FM electrodes are weakly coupled to the SWCNT in the Coulomb blockade regime, the additional voltage developed in the source (drain) electrode induces extra charges through capacitive coupling by $\Delta q(B) = -\frac{C_{s(d)}}{2e}\mathcal{P} g \mu_{\mathrm{B}} B$ in the SWCNT devices, where $C_{s(d)}$ is the capacitance of the source (drain) electrode. These extra charges are continuously induced or depopulated in the SWCNT by the external magnetic field. However, when the magnetic field reaches the coercive fields ($B = \pm B_c$) of the FMs, the induced charges in the SWCNT undergo a discontinuous change. At B_c, the FM polarization switching causes sign reversal in $\mathcal{P}$, which brings additional charges into the SWCNT by :

$$\Delta q(B_c) = \frac{C_{s(d)}}{e}\mathcal{P} g \mu_B B_c. \tag{6.2}$$

In fact, this additionally built-up charges from the MCE is equivalent to the induced charges from the gate electrode. Thus, while varying the external magnetic field, we can observe similar transport behavior in FM-contacted SWCNTs as we expect from the gate voltage measurements. The additional charges from the MCE alter the quantized chemical potentials inside the SWCNT devices equally notwithstanding the detailed spin configurations and energy spacings between states. Therefore, the Coulomb oscillations are shifted by the same amount of gate voltage, which could result in the missing particle-hole symmetry features.

As discussed before, the particle-hole symmetry features in the Coulomb oscillations are determined by the effective Zeeman splitting from the FMs, and it is sensitive to the detailed scattering mechanisms at the interface between FM and SWCNT [48]. In addition, the effective Zeeman splitting is expected to be further reduced in the strong Coulomb blockade regime [73]. On the other hand, the effect from the MCE becomes more prominent as the Coulomb blockade effect gets stronger, so we suggest that the MCE in sample **B** could overshadow the effect from the effective Zeeman splitting.

Within the mechanism of MCE, we can also explain the staircase type single-step MR switching behavior. As expressed in Eq. (6.2), the amount of induced charges is determined by the product of the capacitance, $C_{s(d)}$ and the coercive field, B_c, of FM electrodes. In the gate voltage range of -900 mV $\leq V_g \leq -300$ mV, the capacitances of the source and drain electrodes turn out to be highly asymmetric, which is verified by the prominent single slope of Coulomb blockade diamond structures as shown in Fig. 6.4 (a). The capacitance ratio of the source, drain and gate electrodes extracted by the method introduced in Chapter 2 is $C_d : C_s : C_g \simeq 8 : 2 : 1$, where C_g is the capacitance from the gate electrode coupling. In all measurements presented in this chapter, the hard electrode is employed as the drain electrode and the easy electrode is used as the source, which means the capacitance of the hard electrode is ~ 4 times larger than that of easy electrode. Combining the asymmetric capacitance with different coercive fields for each electrode, the amount of induced charges at the switching of the hard electrode is greater than that of charges from the easy electrode switching by :

$$\frac{\Delta q(B_{c2})}{\Delta q(B_{c1})} = \frac{C_d}{C_s} \cdot \frac{B_{c2}}{B_{c1}} \sim 4 \times 3 = 12. \tag{6.3}$$

We assumed the polarizations of both electrodes are the same. Therefore, the equivalent conductance oscillation shift due to the hard electrode is ~ 12 times larger than that due to the easy electrode, which naturally explains the asymmetric single-step MR switching features as shown in Fig. 6.3.

Here, we point out that even though the extraordinary MR features such as missing particle-hole symmetry and single-step switchings can be all qualitatively understood by the MCE, there exists a point to be addressed at the quantitative level of analysis. The measured Coulomb oscillation shift by $|V_g| \simeq 4$ mV in Fig. 6.4 is equivalent to the energy $\alpha|V_g| \simeq 0.36$ meV, here $\alpha = C_g/(C_s + C_d + C_g) \simeq 0.09$ indicates the strength of the gate coupling. With Eq. (6.1), however, the magnetic field to cause the ~ 0.36 meV energy change is calculated to be around $B \sim 300$ mT, which is approximately one order of magnitude higher than the applied external magnetic field, $B_c \sim 30$ mT. In this estimation, the polarization $\mathcal{P}$ of our permalloy film (Py, $\mathrm{Ni}_{81}\mathrm{Fe}_{19}$) is assumed to be the same as that of the Ni film, $\mathcal{P} \simeq -0.8$ [81, 87], and the Lande g-factor is 2. The more detailed theoretical and experimental works need be followed to answer this difference.

6.5 Magnetoresistance in Four-Probe Device

Another MR feature suggesting the presence of the MCE has been found in the four-probe contacted SWCNT device, sample **C** as illustrated in Fig. 6.5 (a). As shown in Fig. 6.5 (b), the differential conductance measured across the channel defined by the two FM electrodes, II/III, shows similar single-step MR switching as sample **B**. Figure 6.5 (c) shows the two-dimensional conductance plot measured across the

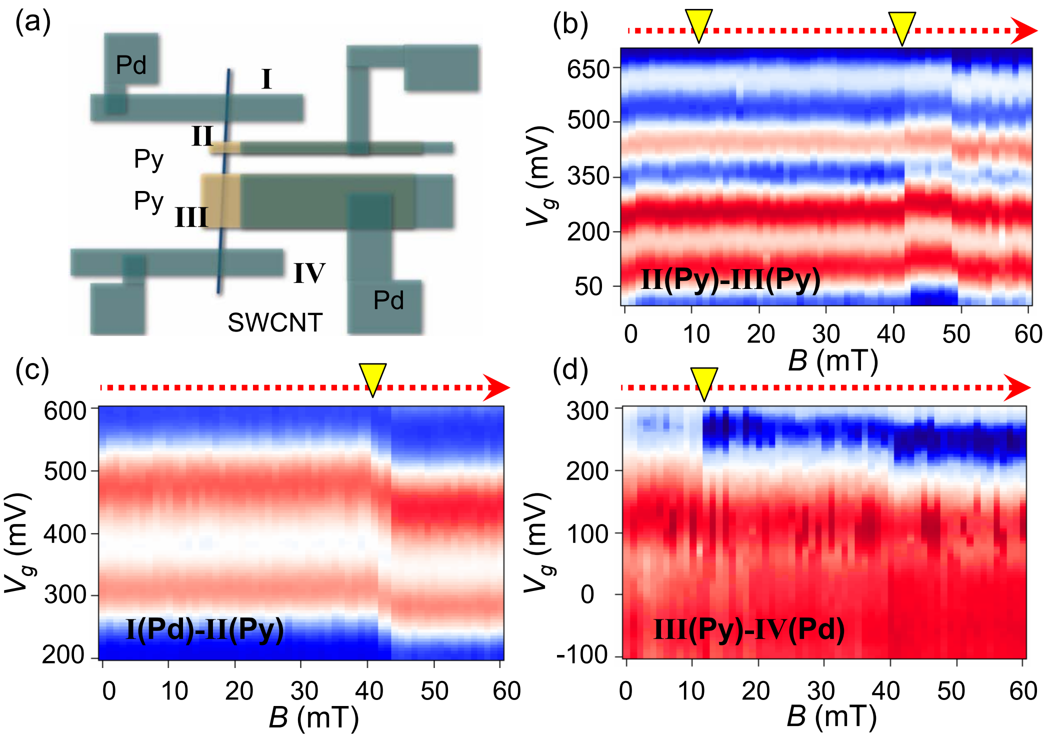

Figure 6.5: (a) Schematic diagram of a four-probe device. Two dimensional conductance plots at different gate voltages with varying external magnetic field across the channel defined by the (b) FM-FM (II-III), (c) NM-FM (I-II) and (d) FM-NM (III-IV).

channel defined by NM (I) and FM (II). Interestingly, the uniform gate voltage shift of conductance oscillations is observed at $B \simeq 42$ mT. Similar switching feature is also observed at $B \simeq 12$ mT between the pair of FM (III) and NM (IV) as shown in Fig. 6.5 (d). The switching feature at $B \simeq 42$ mT is consistently observed in both FM (II)-FM (III) and NM (I)-FM (II) pairs in the several same measurements. The switching at $B \simeq 12$ mT in FM (III)-NM (IV) is also reproducible over several measurements.

These MR switchings that existed with the combinations of NM and FM cannot be expected from the spin transport mechanism, since spin detection is simply impossible with a single FM. As initially suggested by Molen *et al.* [58], however, it is not necessary for SWCNT devices to be contacted by two FMs to manifest the MCE, and a single FM should be enough to introduce the additional charges into SWCNT devices to cause the change in charge transport. Therefore, we can claim that he switching features at $B \simeq 42$ mT in the combination of NM (I)-FM (II) could be associated with the MCE due to the hard electrode II, and the change shown at $B \simeq 12$ mT in the FM (III)-NM (IV) combination due to the easy electrode III. We can further confirm that the polarizations of hard (II) and easy (III) electrode are indeed switched at $B \simeq 42$ and $B \simeq 12$ mT, respectively, from the four-probe non-local measurements. In this measurement, the random MR switchings are significantly reduced because of the separation of spin and charge transports through SWCNTs [57]. The detailed spin transport mechanisms with the four-probe non-local scheme will be discussed in Chapter 7.

6.6 Summary

In summary, we have performed external magnetic field dependent transport measurements in the Coulomb blockade regime with utilizing FM-contacted SWCNT devices, which involved a conventional two-probe measurement scheme. Several interesting MR features, including (i) large MR $\geq$ 100% switching, (ii) the absence of particle-hole symmetry across two- and four-fold Coulomb oscillations, (iii) MR sign change at the peak of Coulomb oscillation, and (iv) single-step staircase switching, are all consistent with the expectations from the MCE. The observation of magnetic field dependent conductance switching from the NM-SWCNT-FM devices further confirms the presence of MCE in two-probe contacted SWCNT devices in the Coulomb blockade regime.

Chapter 7

Direct Observation of Spin Accumulation in a Carbon Nanotube Quantum Dot

7.1 Introduction

In the previous chapter, we have discussed the experimental observations of the magneto-Coulomb Effect (MCE) in the two-probe ferromagnet-contacted single-walled carbon nanotube (SWCNT) quantum dots (QDs). In the Coulomb blockade regime, several distinctive magnetoresistance (MR) features including large $\sim 100\%$ switchings, the absence of symmetry features in two- and four-fold Coulomb oscillations, MR sign change across conductance peaks, and single-step staircase switchings can be associated with the MCE. Even though the MCE can find its physical origin in the electron spins and their dependency on an external magnetic field, it is completely different mechanism from the spin-dependent transport in spin devices, such as magnetic tunnel junctions (MTJs) or spin-valves (SVs), in which an insulating layer or a conducting channel is sandwiched by ferromagnetic electrodes [88, 44]. In those systems, the electronic transport can be controlled by the relative spin polarization of the ferromagnetic electrodes, so that the spin information of the transporting charges plays an important role to decide transport properties of the devices. The MCE does not account for the spin-dependent transport through conducting channels. In the MCE, the unbalanced chemical potential in ferromagnetic electrodes under an external magnetic field induces extra charges inside the SWCNT QDs by capacitive couplings, and causes the change of transport properties notwithstanding the spin information of transporting electrons. Besides the MCE, it has been known that there are several other electronic mechanisms including anomalous magnetoresistance (AMR) [43], Hall effects [59] and tunneling anisotropic magnetoresistance-like effects [60] which could be present in experimental MR data. Thus, separating spin transport signals from the effects mentioned above is necessary to exploit the spin-dependent transport through SWCNTs.

Recently, Tombros *et al.* exploited a four-probe non-local device geometry to explore the spin-dependent transport through SWCNTs [57]. In this scheme, spin transport signals are no longer affected by the MCE and other spurious effects, because the pathway of spin transport is completely isolated from charge flow [43, 89, 90]. However, their experimental data did not show the connection of the observed spin transport to the corresponding charge transport mechanism, mainly due to the lack of gate voltage dependency.

In this chapter, we report experimental observation of isolated spin transport through a ferromagnet-contacted SWCNT QD in the Coulomb blockade regime. We have utilized a four-probe non-local geometry composed of two ferromagnets, permalloy (Py, $Ni_{81}Fe_{19}$), which are employed as spin injector and detector, and two normal metal palladium (Pd) electrodes used for current source and voltage reference [91]. The measured non-local signals, which are directly associated with the isolated spin transport through the SWCNT QD, show gate voltage dependence across four consecutive Coulomb oscillations at low temperatures. The spin transport shows an opposite dependency on whether the accumulated spins are polarized by the injection or the reflection from the ferromagnet electrodes, which is determined by the direction of the driving current [90]. At higher temperature, the non-local spin signals are no longer influenced by the Coulomb blockade effect, and gate-voltage-independent spin signals are sustained up to $T \sim 200$ K.

7.2 Device Fabrication and Measurement

The fabrication of a four-probe-contacted SWCNT device is similar to previously studied two-probe devices except for the additional Pd contacts to SWCNTs. Figure 7.1 (a) is a scanning electron microscopy (SEM) image of the device to be discussed in this chapter. The middle two Py/Pd electrodes (II,III) are fabricated by the first fabrication process, and the outside two Pd electrodes (I,IV) are prepared by the second lithography. The dimension of ferromagnetic electrode II (hard electrode) is $3.0 \times 0.05\ \mu\text{m}^2$, and electrode III (easy electrode) is $3.0 \times 0.5\ \mu\text{m}^2$. The Pd electrodes I and IV are $4.0 \times 0.5\ \mu\text{m}^2$ in size and ~ 40 nm in thickness. All experiments were performed by standard AC lock-in techniques in a variable temperature cryostat equipped with a superconducting magnet. Non-local spin dependent measurements were carried out in the temperature range of $4.2\text{ K} \leq T \leq 200$ K.

7.3 Spin Transport Through Nanotube Quantum Dot

7.3.1 Local Measurement

First, we focus on two-probe local measurements to investigate respective QDs formed between I-II, II-III and III-IV electrodes. The resistances at room temperature between theses three pairs are 130 $k\Omega$, 110 $k\Omega$ and 32 $k\Omega$, respectively. As shown in the two-dimensional conductance plot as a function of bias and gate voltages at $T = 4.2$ K presented in Fig. 7.1 (b), the QD formed between ferromagnets II

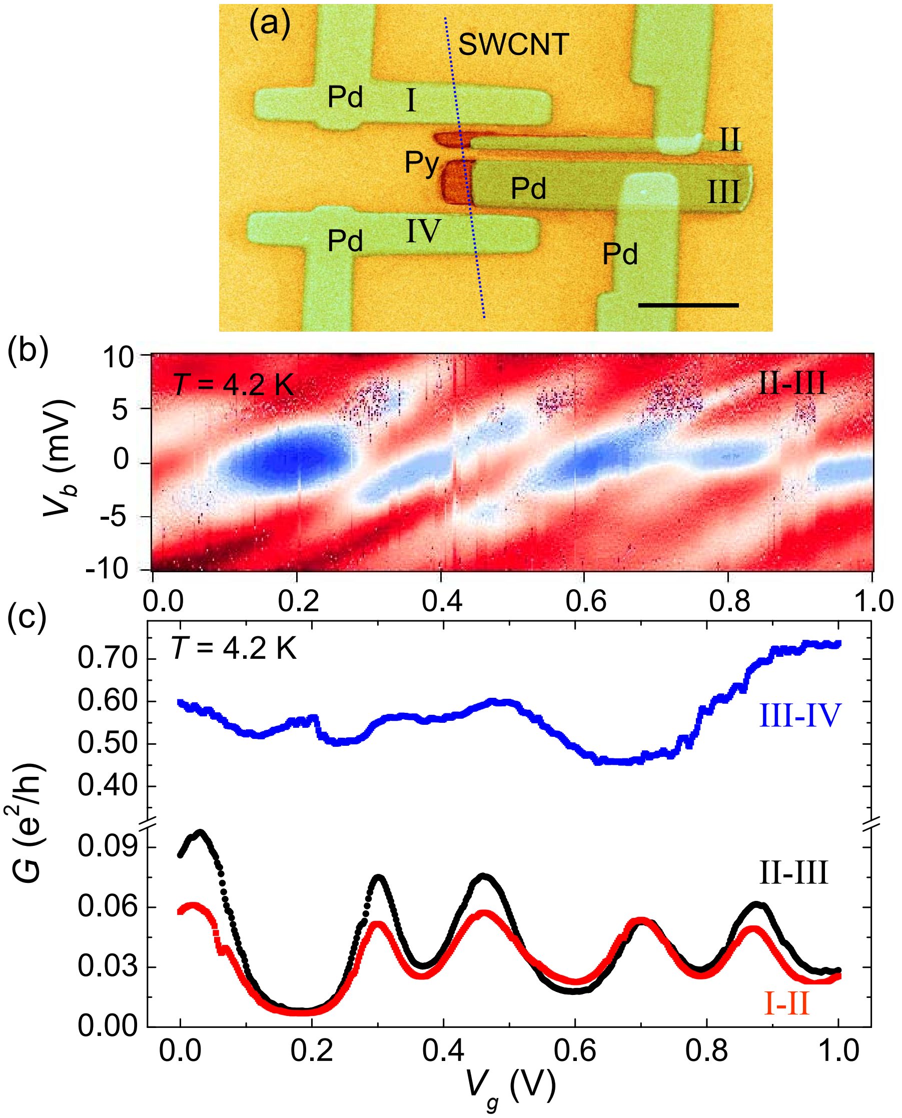

Figure 7.1: (a) SEM image of the four-probe device. (scale bar : 1 μm) The dotted line is used to specify the location of SWCNT. The position of the SWCNT is confirmed by the atomic force microscopy (AFM) scanning. (b) Two-dimensional conductance plot as a function of bias and gate voltage from the SWCNT QD confined by II-III. (c) Conductance oscillations across I-II (red), II-III (black) and III-IV (blue) at $T = 4.2$ K.

and III shows Coulomb diamond structure. Interestingly, the Coulomb oscillations from the QD formed between I-II show almost identical gate voltage dependence as those from the QD defined by electrodes II-III as shown in Fig. 7.1 (c), which suggests the SWCNT behaves as a single QD between I and III. Since the conductance between III and IV is consistently higher than that from the other QD by an order of magnitude, the combination of electrodes III and IV is used for current source in a non-local measurement scheme. The remaining two electrodes, I and II are therefore employed as voltage probes for the non-local spin signal.

In a local measurement scheme depicted in Fig. 7.2 (a), the pathway for spin transport is the same as for charge transport. Therefore, the measured signals could originate not only from the spin-accumulation, but also from other spurious effects including the MCE. Figure 7.2 (b) shows a two-dimensional conductance modulation plot of the SWCNT QD defined by the two ferromagnets, II and III, across four individual Coulomb peaks, with the magnetic field sweeping in the negative sweep direction, i.e., the magnetic field is ramped from $B = 200$ mT to $B = -200$ mT. The first switching at $B \sim -10$ mT is much weaker than the second switching at $B \sim -40$ mT. This single-step staircase switching, which could be attributed to the anisotropic capacitive couplings of source and drain electrodes, is one of characteristic features expected from the MCE as discussed in Chapter 6. In addition, other MR features including the uniform gate voltage shift in Coulomb oscillations and the resulting MR sign change across conductance peaks are also observed in the ferromagnetic electrodes II-III contacted SWCNT QD as shown in Fig. 7.2 (c).

We further performed two-probe local measurements across the combinations of I-II and III-IV. In these combinations, the MR switching due to spin accumulation is not possible. However, the modifications on charge transport due to the MCE can be prevalent [58]. As presented in Chapter 6, MR switching features are observed in both I-II and III-IV combinations, and the switching at $B \simeq -40$ mT shown in

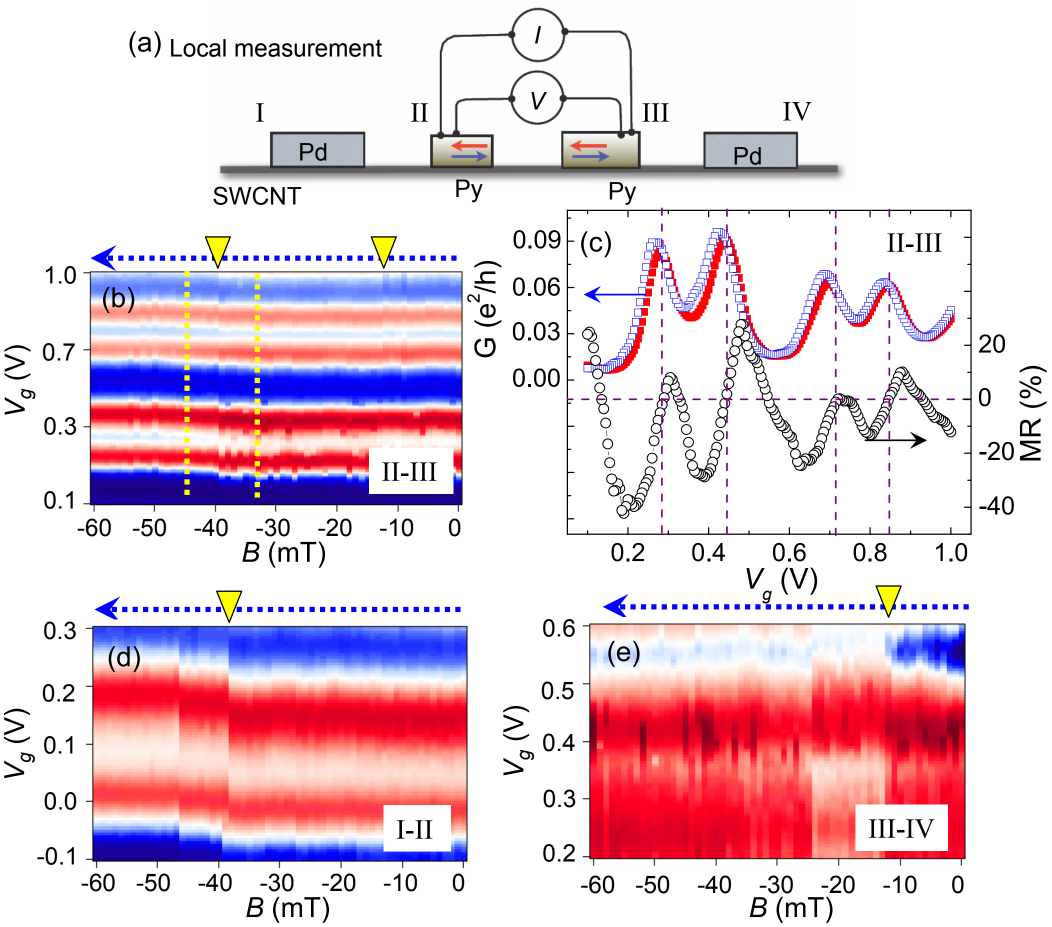

Figure 7.2: (a) Schematic diagram of a two-probe local measurement scheme. (b) Two-dimensional conductance plot of the QD (II-III) as a function of gate voltage with the magnetic field sweeping in the negative direction. (c) Conductance and calculated MR across four consecutive Coulomb oscillations. Red closed and blue open squares represent the conductance in parallel ($B = -45$ mT) and anti-parallel ($B = -34$ mT) configurations, respectively. (d), (e) Two-dimensional conductance plot of the QD defined by I-II and III-IV.

Fig. 7.2 (d) is from the polarization switching of electrode II. The switching shown at $B \simeq -11$ mT in Fig. 7.2 (e) is from electrode III. The switching features at $B \simeq -40$ mT in Fig. 7.2 (d) and $B \simeq -11$ mT in Fig. 7.2 (e) are consistently observed in both local and non-local measurements. Considering several MCE-related features, we can suggest that the MCE is the dominant mechanism in the observed spin-dependent signals measured in the two-probe local schemes. We note that there are other random switching features, which are possibly due to the static charges around the device. The random switchings can be removed by utilizing the four-probe non-local measurement scheme, since the isolated spin signals are not susceptible to charge fluctuations around the device.

7.3.2 Non-Local Measurement

In our non-local measurement scheme, the driving current flows from III to IV, or from IV to III as shown in Fig. 7.3 (a). When the current is introduced from ferromagnet III to the SWCNT channel, the conducting electrons are actually injected from Pd electrode IV to the channel and extracted to ferromagnet III. In this case, we call the sign of current flow as positive. The negative current is for the opposite case, i.e., electrons are injected from ferromagnet III and extracted to Pd electrode IV. The spin-polarized electrons by ferromagnet III can transport through the central QD (II-III), and detected by the voltage probes I and II as $\Delta V = V_{\mathrm{II}} - V_{\mathrm{I}}$, which is referred to as a non-local spin signal from now on [91].

Figures 7.3 (b) and (c) show two-dimensional non-local signal plots as a function of the external magnetic field measured across four Coulomb oscillations under the driving current $I = -50$ nA and $I = 50$ nA, respectively. The signal is measured with the magnetic field sweeping in the negative direction, and the overall non-local signals are almost identical in the positive B-field sweep as well.

Under the negative current, the non-local signal difference between the anti-

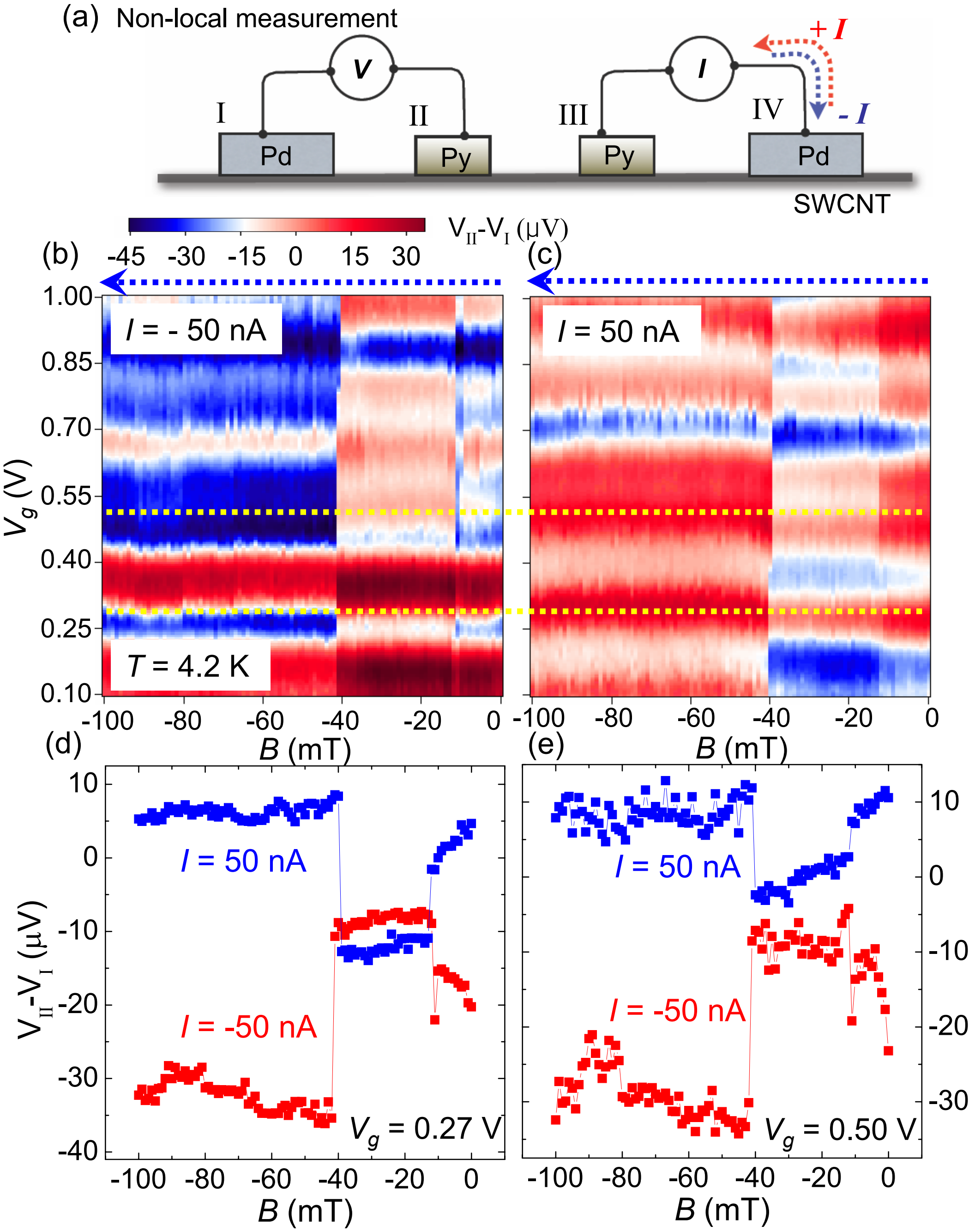

Figure 7.3: (a) Schematic diagram of a four-probe non-local measurement scheme. (b), (c) Two-dimensional non-local signal plots driven by $I = -50$ nA and $I = -50$ nA, respectively, as a function of gate voltage with the magnetic field sweeping in the negative direction. (d), (e) Line traces of the non-local spin signal at peak and valley driven by $I = 50$ nA and $I = -50$ nA, respectively.

parallel (ΔV_{AP}) and parallel (ΔV_P) electrode polarizations, i.e., $\Delta V_{AP} - \Delta V_P$, remains positive across the four individual Coulomb oscillations, even though the magnitude shows modulations as a function of gate voltage as shown in Fig. 7.3 (b). When the driving current is reversed to positive, however, the non-local spin signals show the opposite behavior. In this case, the spin signal difference, $\Delta V_{AP} - \Delta V_P$ turns into negative along with gate-voltage-dependent magnitude modulations similar to the case of negative current. Line plots shown in Fig. 7.3 (d) and (e), which are extracted at fixed gate voltages $V_g = 0.27$ V and $V_g = 0.50$ V, clearly show the opposite behavior of the non-local spin signals with the reversal of the current direction.

As pointed out earlier, the non-local spin signals show gate-voltage-dependent behavior. Figure 7.4 (a) shows both the conductance (top section) and the non-local signal traces across four Coulomb peaks with the driving current varying from 50 nA to -50 nA in the parallel configuration ($B = -50$ mT) at $T = 4.2$ K. The dark dotted lines are used to specify the positions of the individual Coulomb peaks. By comparing the non-local spin signals with the conductance modulations, we can notice that the spin signals indeed correlate with the Coulomb oscillations in the SWCNT QD. For positive driving currents, the non-local spin signals seem to follow the Coulomb oscillations for the first two peaks, i.e., the peaks of non-local signal coincides with the conductance peaks. For the next two Coulomb oscillations, however, the modulation of non-local signal forms dip-like structures at the conductance peaks. When the driving current is reversed to negative, the gate-voltage-dependent non-local signal modulation shows opposite behavior. The dip-like structures of non-local spin signals occur at the conductance peaks for the first two Coulomb oscillations, and the peaks of non-local signals form at the corresponding conductance peaks for the last two oscillations. It is interesting to point out there is an additional peak (dip) structure in the non-local signal, at $V_g \simeq 0.6$ V, which is between the first

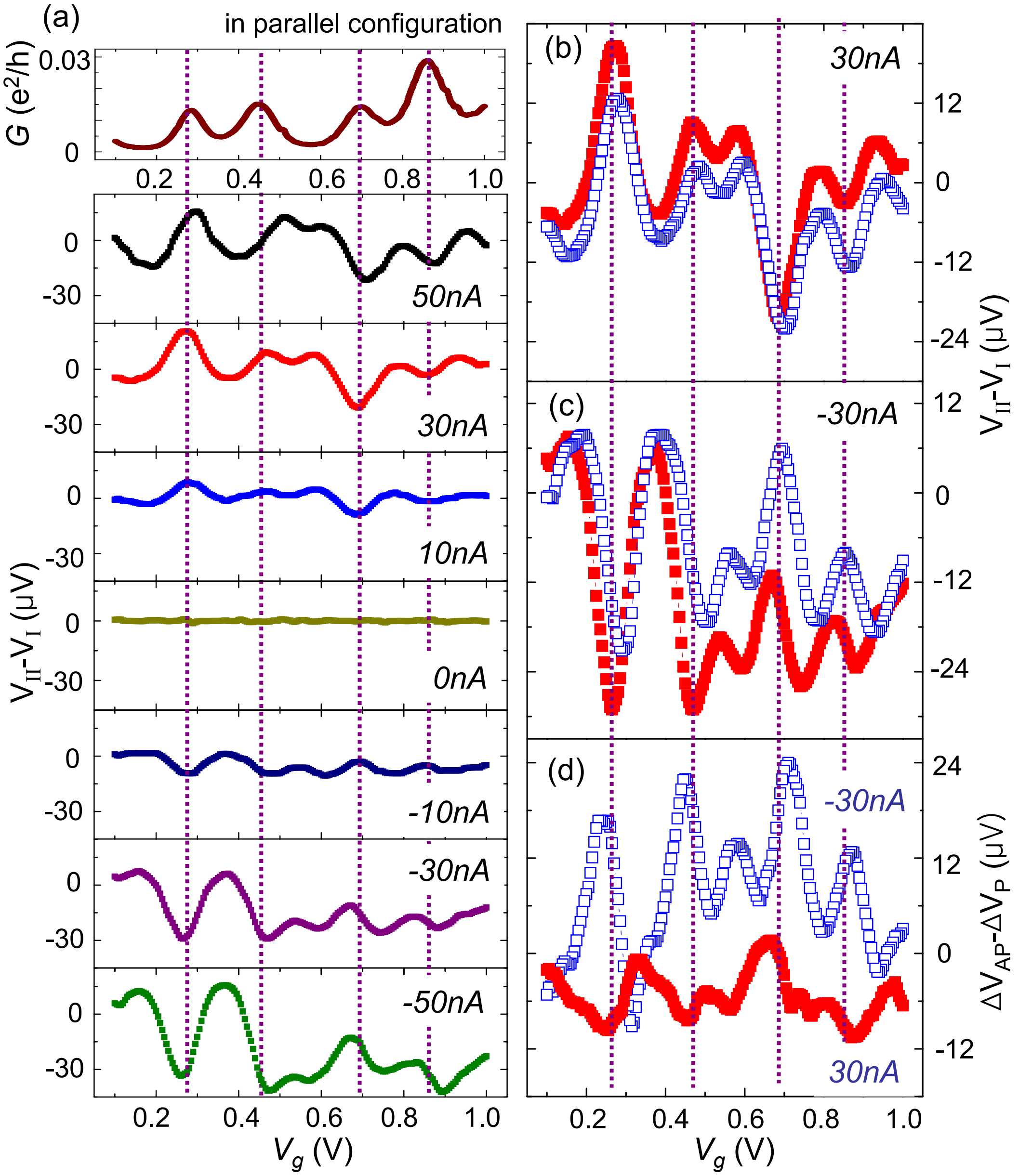

Figure 7.4: (a) Both conductance (top section) and non-local signal modulations across four individual Coulomb oscillations with driving current varying in the parallel configuration, and with $B = -50$ mT at $T = 4.2$ K. (b) , (c) Non-local signal traces as a function of gate voltage in both parallel (red closed squares) and anti-parallel (blue open squares) configurations with $I = 30$ nA and $I = -30$ nA, respectively. (d) Calculated non-local signal difference between anti-parallel and parallel at $I = -30$ nA and $I = -30$ nA.

and the last two Coulomb oscillations under the positive (negative) driving current. In this gate voltage, there is no equivalent conductance peak or dip structure as shown in the top section of Fig. 7.4 (a).

Figures 7.4 (b) and (c) show the non-local spin signal traces across the four Coulomb oscillations with $I = 30$ nA and $I = -30$ nA as the driving current, respectively. The closed red squares represent the data in the parallel configuration, and open blue squares the anti-parallel configuration. As seen from both graphs, the spin signals show similar gate voltage dependency in both the parallel and anti-parallel configurations. The non-local signal differences between parallel and anti-parallel configurations, $\Delta V_{\mathrm{AP}} - \Delta V_{\mathrm{P}}$, for the positive ($I = 30$ nA) and negative ($I = -30$ nA) currents are presented as red closed and blue open squares in Fig. 7.4 (d), respectively, which also show gate-voltage-dependent modulations. In addition, $\Delta V_{\mathrm{AP}} - \Delta V_{\mathrm{P}}$ for the positive current mostly remains negative, and turns into positive for the negative current, as observed in Fig. 7.3.

7.3.3 Memory Effect

To check the reliability of observed non-local spin-dependent signals, we further performed the measurements to show the memory effect of the four-probe-contacted SWCNT spin device as presented in Fig. 7.5 (a) and (b). Under the positive driving current $I = 30$ nA, the magnetic field is first ramped to $B = -200$ mT to align both ferromagnets II and III in the same direction. As the magnetic field is swept in the positive direction, the easy electrode III first switches its spin polarization at $B \simeq 11$ mT, at which the relative spin polarization of the ferromagnets becomes anti-parallel. As the magnetic field is ramped further until it reaches $B = 30$ mT, the spin polarization of electrodes remains in the anti-parallel configuration, since the hard electrode II, whose coercive field is $B \simeq 40$ mT, is still aligned in its initial direction. At $B = 30$ mT, the magnetic field is swept back to $B = -200$ mT.

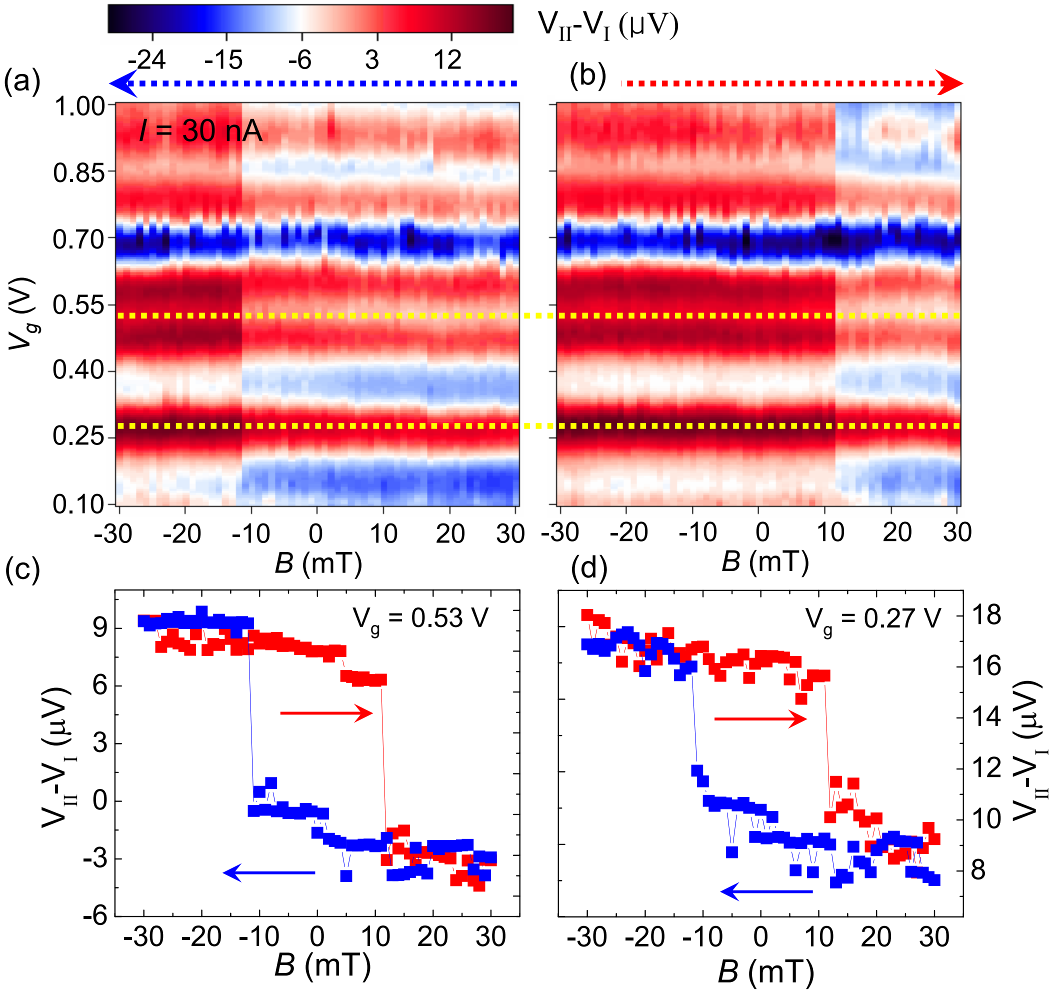

Figure 7.5: (a), (b) Two-dimensional non-local spin signals as a function of gate voltage with the magnetic field sweeping in the negative and positive sweep directions, respectively. (c), (d) Line traces of non-local signal showing the memory effect at different gate voltages.

The anti-parallel electrode polarization is thus maintained until the easy electrode is switched back to the original direction at $B \sim -12$ mT. If we follow the B-field sweep scheme described above, there exist two different values for non-local spin signals at zero magnetic field representing the relative spin configurations, i.e., parallel and anti-parallel.

The non-local signal traces in Fig. 7.5 (c) and (d) show the characteristic features of the memory effect at different gate voltages, and there exist two different non-local signals at $B \sim 0$ mT. Similar hysterisis loop structure was also observed under the negative current flow, $I = -30$ nA. From these measurements, we can show that we can willingly control the spin polarization of ferromagnetic electrodes with the external magnetic field, and the non-local spin signals are indeed determined by the relative spin polarization directions of the ferromagnetic electrodes.

7.3.4 Discussions

The non-local spin signals have revealed the opposite dependency on the driving current direction as demonstrated in both the spin signal difference between parallel and anti-parallel configurations, $\Delta V_{\mathrm{AP}} - \Delta V_{\mathrm{P}}$, and the gate-voltage-dependent modulations. In the following, we will present a simple physical picture to address the dependence of non-local spin signals on current directions.

In the case of positive driving current, conducting electrons are injected from the Pd electrode IV into the SWCNT, and extracted to the ferromagnetic electrode III. The non-polarized electrons in the SWCNT can then be spin-polarized by the interaction with the Py electrode. For instance, if the ferromagnetic electrode is aligned in the spin-up direction, spin-up electrons can be easily extracted from the SWCNT to the ferromagnet, but spin-down electrons cannot, which results in an increased number of spin-down electrons in the SWCNT channel. Therefore, the accumulated electron spins in the SWCNT have the opposite spin orientation to that of the ferromagnet. Such opposite spin polarizations between ferromagnet and electrons underneath the electrode was experimentally observed in gallium arsenide (GaAs) spin devices by scanning Kerr microscopy technique [92]. The accumulated spin-polarized electrons are ultimately transported through the central QD, and are detected by the second ferromagnet, II. On the other hand, when the electrons are injected from polarized ferromagnets to the SWCNT channel, the polarization of accumulated electrons in the SWCNT channel is aligned in the same direction with that of the ferromagnet electrode. If the ferromagnetic electrode is aligned in the spin-up direction, more spin-up electrons are injected from the ferromagnet to the SWCNT channel than spin-down electrons. The resultant polarization of accumulated electrons in the SWCNT channel is then aligned in the same direction as the electrode.

Thus, the spin polarization of accumulated electrons in the SWCNT channel is opposite for different driving current directions. Because the spin detection mechanism at the second ferromagnet II is the same irrespective of the direction of the driving current, the measured non-local spin signals show opposite dependency on the current directions. The similar sign change of the non-local signal differences between parallel and anti-parallel configurations, $\Delta V_{\mathrm{AP}} - \Delta V_{\mathrm{P}}$ depending on the driving current direction was observed in a GaAs semiconductor contacted by Fe electrodes [90].

However, the gate-voltage-dependent non-local signals observed in our device have not been either observed experimentally or discussed theoretically. It is obvious that the non-local spin signals are highly correlated with the Coulomb oscillations, but how the gate-voltage-dependent non-local signals are related to the corresponding Coulomb oscillations needs to be answered.

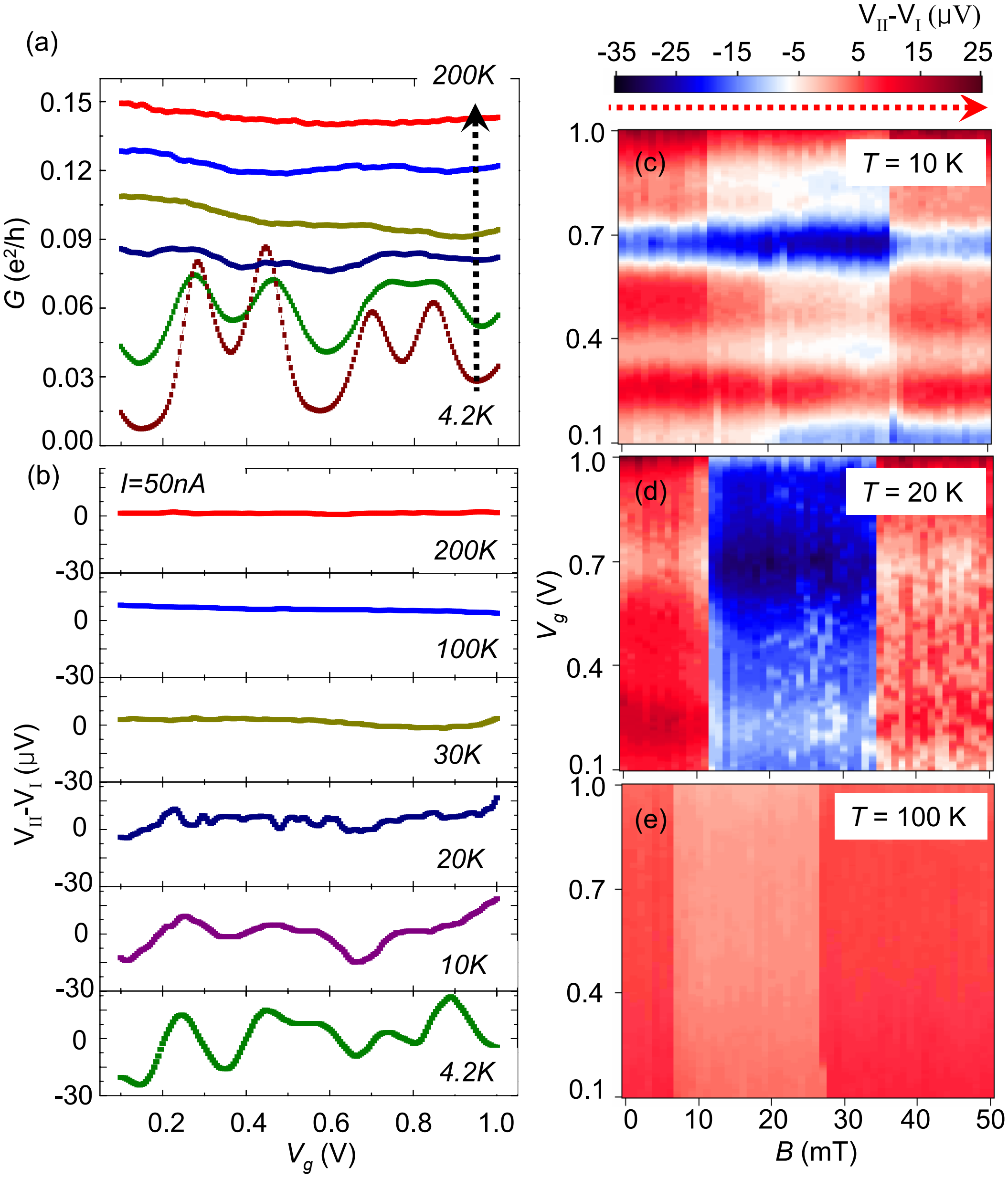

Figure 7.6: (a) Conductance modulations at different temperatures across the QD formed by two ferromagnets, **II-III**. (b) Non-local signal traces as a function of gate voltage at different temperatures. Two dimensional non-local signal plots with the magnetic field sweeping in the negative direction at different temperatures, (c) $T = 10$ K, (d) $T = 20$ K and (e) $T = 100$ K. The driving current is $I = 50$ nA.

7.4 Temperature-Dependent Spin Transport

Another evidence that non-local spin signals are influenced by the Coulomb blockade effect can be found temperature-dependent measurements. At $T = 10$ K, there still remain well-defined Coulomb oscillations in the conductance plot, and the non-local spin signals also show gate-voltage-dependent modulations as shown in Fig. 7.6 (b) and (c). However, the gate-voltage-dependence features in the non-local signal disappear at 20 K, above which the Coulomb blockade effect is smeared out because of the increasing thermal energy. From this observation, we can further confirm that the gate-voltage-dependent non-local spin signals are indeed associated with the Coulomb blockade effect at low temperatures. At higher temperatures, the spin transport through the SWCNT is independent of the gate voltage. We found that the non-local signal becomes weaker, but spin signals induced by the reversal of electrode spin polarization are measurable up to ~ 200 K.

We further analyzed the temperature-dependence of the non-local spin signals in a quantitative way. Figures 7.7 (a) and (b) show the non-local signal difference between parallel and anti-parallel configurations, $\Delta V_{\mathrm{AP}} - \Delta V_{\mathrm{P}}$, at $V_g = 0.4$ V under the negative and positive driving currents, respectively, at different temperatures. The opposite spin-signal behavior depending on the driving current directions is clearly noticeable. In addition, the decrease of $\Delta V_{\mathrm{AP}} - \Delta V_{\mathrm{P}}$ is observed with increasing temperature. The complete temperature dependence of the non-local signal difference is displayed in Fig. 7.7 (c) in the range of $4.2 \text{ K} \leq \text{T} \leq 200$ K, which shows two separate temperature regimes. In the first regime, $4.2 \text{ K} \leq T \leq 20$ K, the non-local signals are sensitive to the gate voltage because of the Coulomb blockade effect. In the second regime $T \geq 30$ K, however, the non-local spin transport through the SWCNT QD is no longer influenced by the Coulomb blockade effect, and the value of the non-local signal monotonically decreases and becomes immeasurable at $\simeq 200$ K. Following the decrease of spin signals, the absolute value of coercive fields B_c,

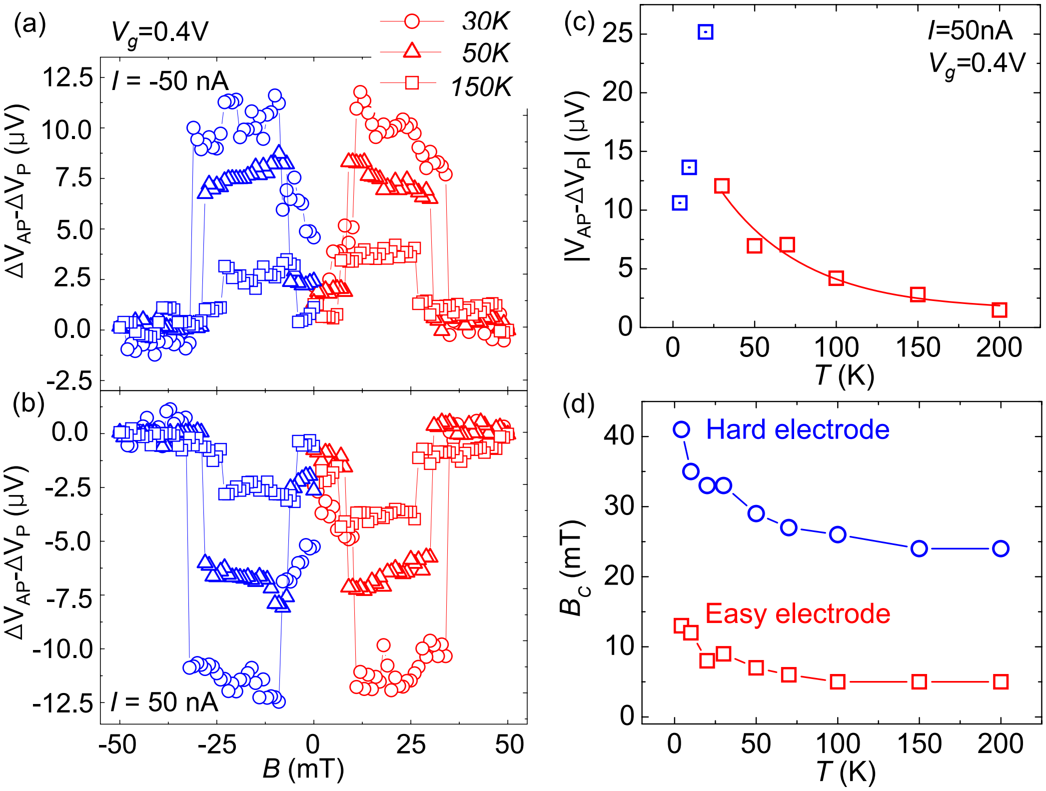

Figure 7.7: Non-local spin signals at different temperatures at (a) $I = -50$ nA and (b) $I = 50$ nA. The data is normalized with the value in the parallel configuration at $B = 50$ mT. (c) Non-local voltage shift between parallel and anti-parallel configurations as a function of temperature. (d) Temperature dependence of coercive fields B_C for easy and hard electrodes.

for both the easy and hard electrodes decay as the temperature increases, as shown in Fig. 7.7 (d). B_C of the easy electrode III decreases from 12 mT at 4.2 K to 6 mT at 200 K, and that of the hard electrode II decreases from 41 mT at 4.2 K to 24 mT at 200 K.

The decrease of the non-local spin signals with increasing temperature has also been observed in diffusive metallic systems [43, 89], which is attributed to the decrease of spin-coherence length as the temperature increases. However, we cannot make a straightforward comparison between the diffusive metallic systems and the SWCNT, since the transport through SWCNTs is considered to be ballistic [93, 27]. In our device, the single-QD behavior observed across the electrodes I and III suggests that the transport through the SWCNT channel (II-III) is indeed ballistic. In order to investigate the spin transport through the ballistic SWCNT systems, other careful experiments such as the channel-length-denpendent non-local spin signal measurements may be necessary to address how the spin-coherence length is related with ballistic transport mechanism.

7.5 Summary

In summary, we have experimentally observed the isolated spin transport through the SWCNT QDs utilizing a four-probe non-local geometry, in which two ferromagnetic electrodes are used to control spins, and two normal metal electrodes are for the current source and voltage reference. The non-local spin signals show the opposite behaviors in gate-voltage-dependent modulations and spin signal difference, $\Delta V_\mathrm{AP} - \Delta V_\mathrm{P}$, when the direction of the driving current is reversed between positive and negative, which could be attributed by the opposite spin-polarization mechanisms depending on different current directions. The non-local spin signals through the SWCNT QD is found to be highly correlated with the Coulomb oscillations in the Coulomb blockade regime at low temperatures. At high temperatures, the spin transport through the SWCNT is no longer influenced by the Coulomb blockade effect. We found that the non-local signal becomes weaker as temperature increases, and gate-voltage-independent non-local spin signals are measurable up to ≤ 200 K.

Finally, we point out that our four-probe non-local devices allow the study of the spin precession effect, which would allow us to finally test the plausibility of spin-charge separation in a one-dimensional system [61, 62].

Chapter 8

Background and Motivations for Studying Organic Semiconductors

8.1 Background

Over the last couple of decades, a new research field based on electronically active carbon based semiconducting materials such as conjugated polymers and oligomers has emerged [94]. This research field has utilized organic thin film transistors (OTFTs) as its basic operation unit. Because of the relatively low mobility of the organic semiconductor films, OTFTs are not expected to compete with the conventional semiconducting transistors based on single-crystalline inorganic semiconductors such as Si, Ge, and GaAs, in the area where high speed is the key element of device performances [95]. However, both low cost and appealing device-processing conditions such as low processing temperature, open the possibility that OTFTs can replace or compete with several current thin-film transistor applications. For instance, flexible displays [96], organic light-emitting diodes [97], flexible thin-film photovoltaic cells [98, 99], disposable electronics [100], low price active matrix displays [101], chemical sensors [102], and radio frequency ID tags [103] are the areas where organic-based electronics have advantages over inorganic semiconductors.

Among those, the applications for flexible displays [101] and electronic papers [104] have been intensively studied and developed enough to be available commercially. In these fields, a charge carrier mobility $0.1-1$ cm^2/Vs, on/off current ratio $\geq 10^4$, and a threshold voltage close to zero should be comparable to those of amorphous silicon [105]. Several organic semiconductors, such as pentacene [106, 107] and rubrene [108] exhibit charge carrier mobilities within or even exceeding the range, and pentance OTFTs show superior on/off current ratio $\simeq 10^8$ and a zero threshold voltage as well [95].

Even though the lengthy list of applications and the breathtakingly rapid improvements in device performance show how much attentions have been paid to organic electronics, the physical mechanisms of electronic charge transport have not been well established. Because of its week intermolecular bonding, i.e., Van der Waals bonding which results in small bandwidth and large effective mass of charged carriers, charge transport in organic semiconductors is no longer described by delocalized charged carriers as in metal systems. In the form of thin film, which is most organic electronics have been relied on, charge transport is limited by extrinsic factors, such as grain boundaries [109, 110] and ambient conditions [111]. When organic semiconductors are utilized in OTFTs, charged carriers are also hampered by device parameters, such as metal contacts [112] and the interaction with gate-insulating materials [113]. In these cases, charged carriers are usually immobilized at several localized states, and able to escape from those trap states with an assist from lattice vibrations (phonon). Thus, the charge transports through organic semiconductors can be explained by a phonon-assisted hopping model or a multiple trapping and release model [114].

Among these, the interaction between gate insulator and organic semiconductor, and its influence on charge transport behaviors have been caught attentions. Since charge transport is expected to be restricted to a few molecular layers of the organic materials at the interface with gate insulators in OTFTs [5, 6], understanding the electronic transport mechanism in ultrathin two-dimensinal molecular layers is of fundamental interest and is critically required to improve device performance as well.

8.2 Organic Field-Effect Transistors

Operations of OTFTs

Ever since the first realization of OTFT exhibiting meaningful current control with a gate electrode [115], OTFTs have been relied on conventional two-probe source and drain electrodes fabricated by either top or bottom contact method as shown in Fig. 8.1. In both geometries, the charge density in the active organic semiconductor layer is controlled through capacitive coupling by a gate electrode. In the top-contact scheme, organic semiconductors initially deposited on top of gate-insulating layers by several methods, such as vapor deposition in vacuum [116] or in carrier gas [117], solution process [118], and direct stamp printing [119], are electronically contacted by metal electrodes. In the bottom-contact scheme, semiconducting films are deposited on pre-fabricated source and drain electrodes by the similar methods as shown in Fig. 8.1 (b). It has been known that the top-contact method is usually better than the bottom-contact in terms of charged carrier mobilities [120], because molecular ordering at the interface between metal and semiconductors is usually poor in the bottom contact scheme, which introduces more trapped states in the conducting channel. Besides, we need to use the top-contact scheme for our research purposes, since the continuous organic semiconductor film growth in between pre-fabricated electrodes (bottom-contact) is basically impossible considering the height difference between metal electrodes ($\geq$ 10 nm) and a pentacene single layer ($\sim$ 1.6 nm).

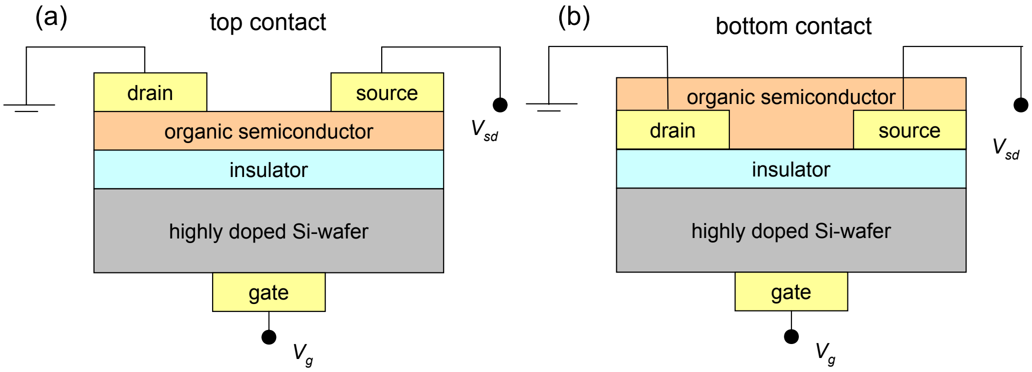

Figure 8.1: Schematic diagrams of (a) top and (b) bottom contacted organic thin film transistors.

The electronic properties of OTFTs are characterized by a transfer characteristic behavior obtained by a current-voltage (I-V) measurement. At small bias V_{sd} and large gate voltage V_g, which is referred to as linear regime ($V_g \gg V_{sd}$), the current flowing through organic semiconductor film can be expressed by :

$$I_{sd} = \frac{W}{L} C_i \mu \left(V_g - V_t\right) V_{sd} \ , \quad V_{sd} \ll V_g, \tag{8.1}$$

where W and L are channel width and length, respectively, C_i is the gate capacitance per unit area, μ is the effective field-effect mobility, and V_t is the threshold voltage [121]. Thus, charged carrier mobility μ can be calculated from the slope of the transconductance ($\partial I_{sd}/\partial V_g$) curve using the geometrical dimensions of OTFTs and the permittivity of gate-insulating materials. In the saturation regime ($V_{sd} \gg V_g$), the drain current is then independent of the bias voltage :

$$I_{sd,sat} = \frac{W}{2L} C_i \mu \left(V_g - V_t\right)^2 \ , \quad V_{sd} \gg V_g. \tag{8.2}$$

When the square-root of the drain current $\sqrt{I_{sd,sat}}$ is plotted as a function of gate voltage, the carrier mobility μ can be extracted from the slope of the curve in the

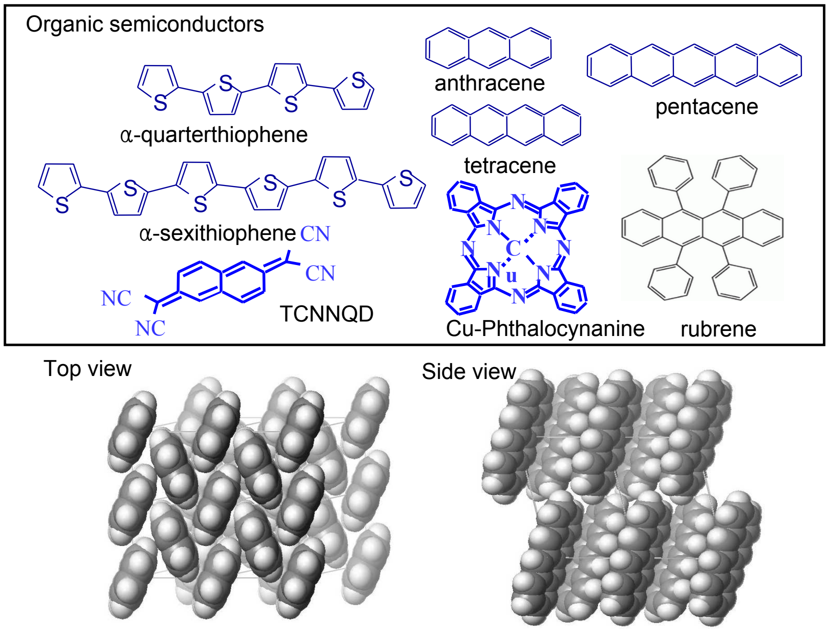

Figure 8.2: Different organic semiconductors. (top) Herringbone structure of pentacene molecules viewed from top and side. (bottom)

saturation regime as well.

Organic semiconductors.

At the early stage of OTFT research, conducting polymers such as polyacetylene and polythiophehe were mainly used as active semiconducting layers. The field-effect mobilities of the OTFTs based on conducting polymers were several orders of lower than ~ 1 cm^2/Vs because of the poor crystalline structure. However, the solution solubility of conducting polymers has been considered as the advantage over inorganic semiconductors and other non-soluble organic semiconductors, because it can be processed by simple methods such as spin-casting or drop-casting, which is desirable for large area electronics. For some organic electronic applications, such as organic based display, however, the low mobility of conducting polymers is still concerned.

The improved mobilities have been found in small-molecular-size organic semiconductors, which are made up of only a few or a few dozens of repeat units. It is well known that these small molecular materials, such as pentacene and thiophene tend to align in the same direction when they are deposited on the substrates in elevating temperature, and even form a single crystalline structures [95, 122]. As shown in the lower half of Fig. 8.2, single molecules stacked in the Herringbone structure usually show higher mobilities because of improved molecular orderings and decreased distance between adjacent molecules, which causes increased π-π^* molecular orbital overlap. In our studies, we have chosen pentacene as a active organic semiconducting layer not only because it has shown one of the highest charge carrier mobilities [123], but also it is chemically stable under the ambient conditions.

8.3 Motivations for Studying Few-layer Pentacene

Among several key elements to determine charge transport behaviors through OTFTs, grain boundaries formed within a conducting channel have been known as one of the major bottlenecks in charged-carrier flow [124, 125]. Since charge transport through OTFTs mainly occurs at the first few layers of organic semiconductors from a gate-insulating material, it is almost impossible to correlate the experimental observations with structural factors such as grain boundaries in typical OTFTs. Most of the studied OTFTs have several orders of $\sim$ nm film thickness, and the conducting channel is placed deep inside the organic films in those devices. Besides grain boundaries, we can directly associate measured charge transport behaviors with other device factors, such as the interactions with gate-insulating material, metal contacts and ambient conditions, when we are allowed to access the conducting channels in OTFTs. Thus, single molecular layer represents the ideal model for studying charge transport behavior in OTFTs, which will eventually elucidate the basic transport mechanism through OTFTs.

Chapter 9

Fabrication of Ultrathin Pentacene Field-Effect Transistors and Measurements

9.1 Introduction

The device structure of organic thin-film transistors (OTFTs) is illustrated in Fig. 9.1. There are source and drain electrodes, and the Si/SiO$_2$ substrate will be utilized as a gate electrode. Pentacene film is grown by the physical vapor deposition (PVD) method on top of oxidized highly doped silicon substrates. In this chapter, we will first discuss the methods of pentacene single-layer film growth by the PVD method, and present the fabrication process for a silicon nitride membrane shadow mask, which will be used for source and drain electrode fabrication. We will also briefly describe the experimental techniques and measurement methods.

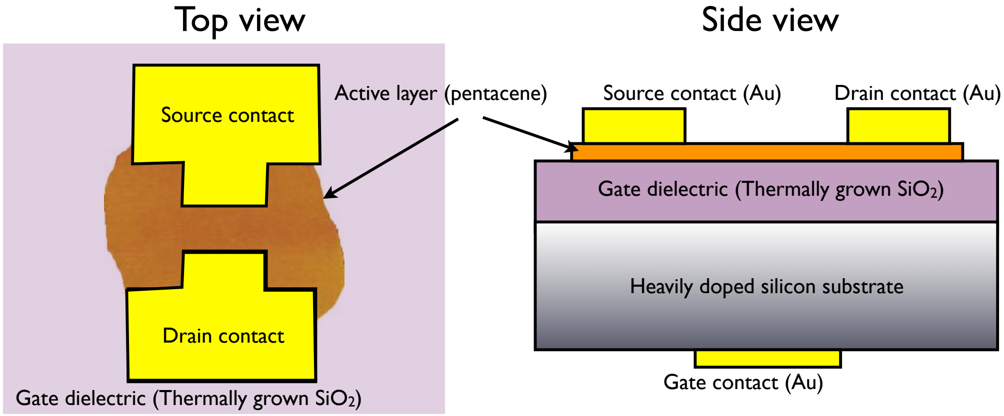

Figure 9.1: Schematic diagrams of pentacene thin film transistors.

9.2 Growth of Pentacene Few layers

The starting pentacene source is purchased from Sigma-Aldrich, and purified several times before the actual film growth [126, 122]. Figure. 9.2 (a) shows a schematic diagram of the temperature gradient sublimation system for purifying pentacene source. The 1-inch diameter, 15-inch long glass tube with one end closed (tube #2) is placed inside an approximately 2-inch in diameter, 40-inch long glass tube (tube #1). The closed end of the tube #2 is positioned at the middle of the tube #1, and the open end is placed to face the closed end of the tube #1, as shown in Fig. 9.2 (a). A small glass boat holding the starting pentacene source is placed at the closed end of the tube # 2, which is positioned at the middle of a three zone furnace. The additional 0.5-inch in diameter 5-inch in length glass tube (tube #3) is placed at the other end of the tube #2 to collect sublimated pentacene molecules. Since the position of the tube #3 is just outside the heating zone, sublimated pentacene molecules from the source condenses on both the outside and the inside the collection tube #3. The whole sublimation tube assembly is evacuated with a turbo pump. Once the vacuum reaches base pressure, the furnace is slowly heated up from room temperature to 350 °C, and maintained at 350 °C until the

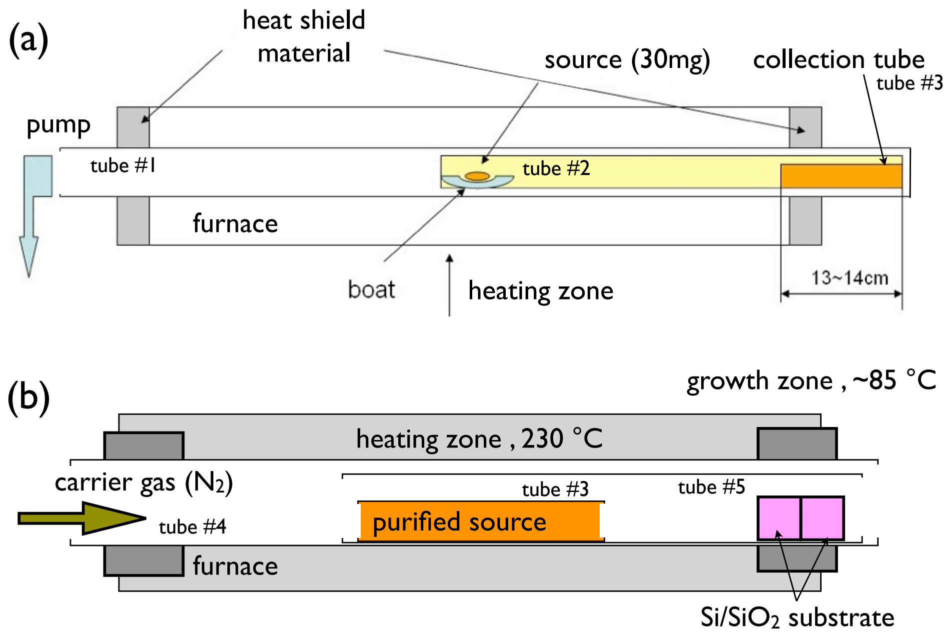

Figure 9.2: Schematic diagrams of organic pentacene film growth. (a) Material purification setup. (b) Phase vapor deposition setup.

source material is completely sublimated. We usually use $\sim$ 30 mg of pentacene for the starting material, and the collected pentacene source is purified a couple of times more followed by the same vacuum sublimation method to ensure the purity of pentacene source.

The wet-oxidized highly doped silicon substrate is diced to 7×7 mm^2, and thoroughly cleaned ultrasonically in fuming nitric acid, acetone and isopropanol for 20 minutes each. Subsequent high temperature annealing at 900 $^\circ C$ in a mixture of 1:1 ratio of H_2:Ar helps reduce nucleation centers. In addition, high temperature annealing also improves the surface flatness of Si/SiO_2 substrate. The annealing in the ambient of H_2 further helps reduce trap density at the interface of Si and SiO_2 [64].

Figure 9.2 (b) shows a schematic diagram of the PVD method for pentacene film growth. The 0.5-inch diameter collection tube (tube #3) covered with multiple-times-purified pentacene molecues is positioned in the middle of a 1-inch diameter glass tube (tube #4) placed in a horizontal tube furnace. In between tube #3 and #4, an additional 0.7-inch diameter glass tube (tube #5) is inserted to stabilize carrier gas (N_2) flow. At first, high purity (99.95%) nitrogen is flown for a few hours to dispense air and moisture from the growth tube. After that, the source material is heated up slowly, first up to 200 °C at a rate of 2 °C/min, then to 230 °C at 5 °C/min. The sublimated molecules are carried by the nitrogen gas flowing at a 50 sccm rate, and deposited on the Si/SiO_2 substrate placed downstream of the gas flow at a temperature of $\sim$ 85 °C. By controlling the growth time and substrate distance from the source material, we can control the size and coverage of pentacene thin film.

Figure 9.3 displays tapping mode atomic force microscopy (AFM) images of pentacene thin films showing the variations of both coverage and grain size. Since pentacene molecules are stacked perpendicularly to the substrate maintained at elevating temperature [95], and the height of individual layer determined by the height profile of the AFM scan is consistent with the 1.6 nm length of single pentacene molecules, the pentacene films shown in Fig. 9.3 are indeed composed of single molecular layer of pentacene.

9.3 Fabrication of Shadow Masks

To realize OTFTs, the grown pentacene single-layer needs to be electronically contacted by source and drain metal electrodes. The first plausible way is to directly evaporate metal films through shadow masks placed on top of the petacene-deposited substrate. Even though the size of single grain pentacene film is up to several μm, it is not large enough to be contacted by commercially available shadow masks, whose dimension is more than $\sim$ 20 μm source and drain electrodes spacing. Thus, we need to fabricate home-made shadow masks to reduce electrode spacing down to

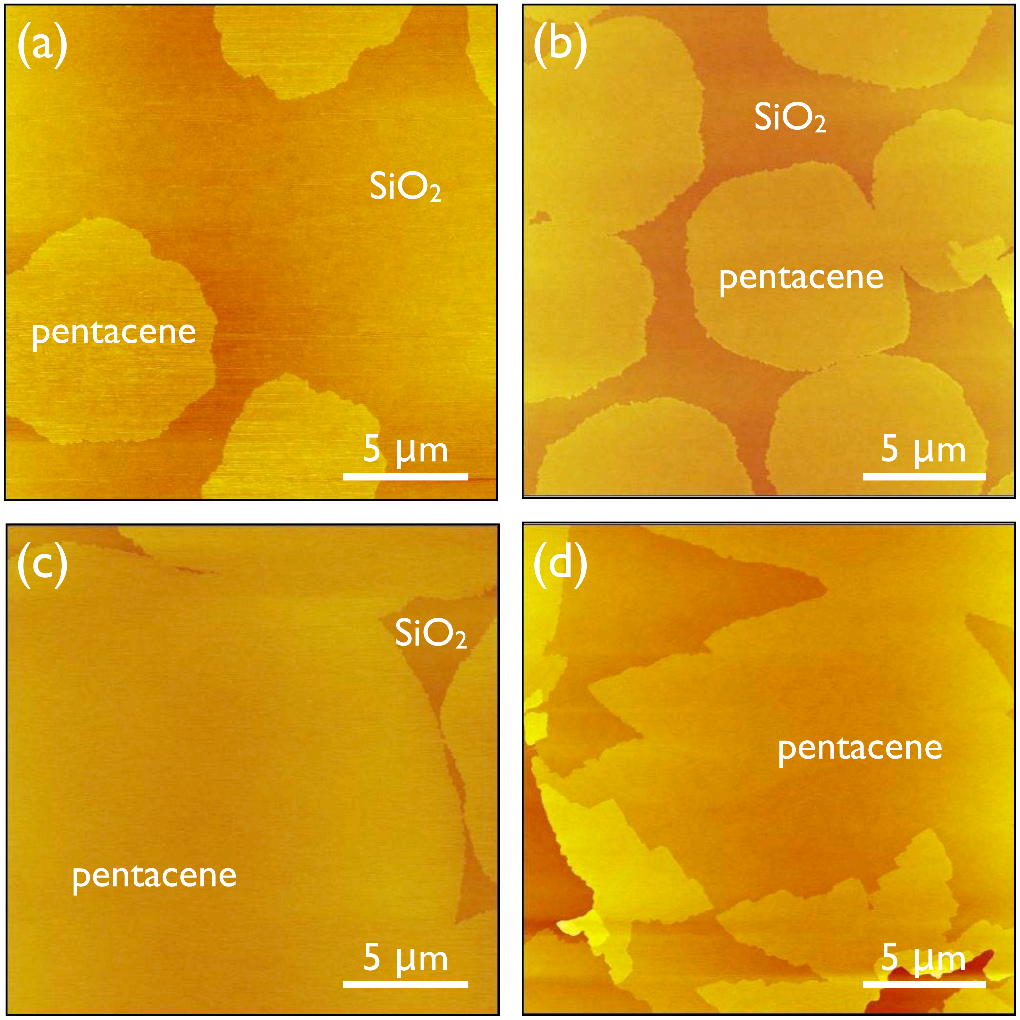

Figure 9.3: Tapping mode AFM images of varying pentacene thin film coverage

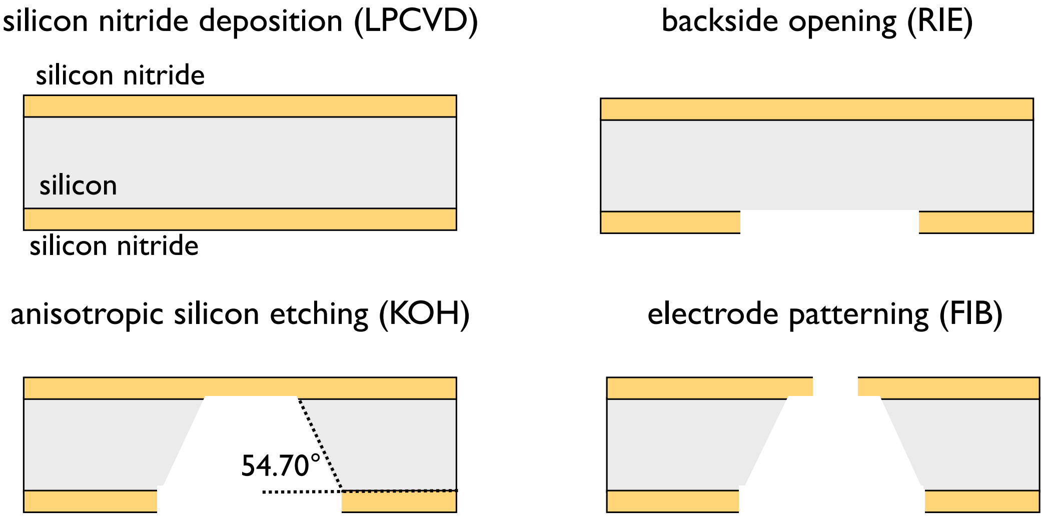

Figure 9.4: Schematic diagrams of fabrication of silicon nitride membrane shadow mask.

$\leq 5\ \mu m$.

Figure 9.4 shows the overall fabrication processes of silicon nitride membrane shadow masks. A 4-inch silicon wafer is thoroughly cleaned by piranha and RCA cleaning methods, and 80 nm thick low-stress silicon nitride (SiN_x) is then deposited on both sides of the silicon substrate by the low-pressure chemical vapor deposition (LPCVD) method. Optical lithography is used to pattern opening holes on the back side of the Si/SiN_x wafer. First, the back side of the Si/SiN_x wafer is coated with hexamethyldisilizane (HMDS), which promotes the adhesion of photoresist to the wafer. Next, PR 5214 photoresist is spin-coated, and baked on a hot plate at 90 °C for 2 minutes. During this process, the front side of the substrate must be protected from unexpected damage. After exposure to ultraviolet (UV) light, patterns are developed in an AZ 726 developer for 60 seconds, and rinsed with water. The substrate is then post-baked in a convection oven at 120 °C for 8 minutes.

The silicon nitride patterns opened by optical lithography is then removed by reactive ion etching (RIE). Gases used for etching silicon nitride films are tetrafluo-

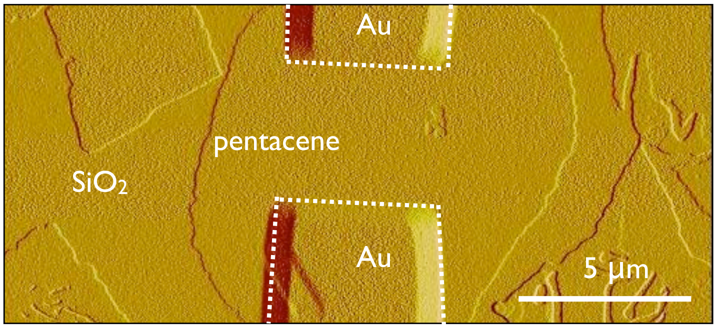

Figure 9.5: AFM image of a pentacene single-layer OTFT.

romethane CF_4, and oxygen O_2. The area covered by photoresist is protected, and the silicon nitride opened by optical lithography is etched by RIE.

Heated ($\sim$ 80°C) potassium hydroxide (KOH) solution is used for preferential crystallographic ethching of the silicon wafer. The etching angle of the silicon <100> substrate is 54.7 ° from the surface, and the etching rate is determined by the temperature and concentration of the KOH solution. The higher temperature and concentration gives the faster etching, but fast etching will degrade the etching angle and the flatness of etched silicon surface. The etching is finished by cleaning the substrate in heated IPA solution to remove remaining KOH residue.

The resultant silicon nitride membrane is patterned with a focused ion beam (FEI Strata DB235 SEM/FIB). The dimensions of the source and drain electrodes are usually 5 μm in width and 20 μm in length. These electrodes are connected to 120×120 μm^2 size of bonding pads. We use $\sim$ 500 pA ion-beam current to pattern source and drain electrodes, and 20 nA to fabricate bonding pads.

9.4 Fabrication of Pentacene Field-Effect Transistors

Pentacene OTFTs are completed by thermally evaporating Au film through the shadow mask fabricated in a suspended silicon nitride membrane. A representative petacene single-layer OTFT is shown in Fig. 9.5. The ~ 50 nm thickness Au film is evaporated at a slow rate, ≤ 0.2 $\mathring{A}$/s, to avoid heat damage on the pentacene film in $\sim 2.0 \times 10^{-7}$ Torr vacuum. A mechanical scratch on the back side of the substrate is applied with a diamond scriber to remove SiO_2 to make electric contact for the gate electrode. The final sample is mounted on a 28-pin chip carrier as shown in Fig. 3.5 (d). After bonding Al wires to the Au bonding pads, the sample is mounted on a dip-stick type cryostat for measurements.

9.5 Electric Measurements

Charge transport measurements with pentacene OTFTs are mostly performed with a dip-stick type cryostat in vacuum and in darkness. The measurement methods and instruments are almost identical to those in SWCNT measurements except for high voltage measurements. Since the voltage output from the DAC is limited to ±10 V, a Keithley 6517 A electrometer and a Valhalla Scientific 2701C are used for bias and gate voltage sources in high voltage measurements up to 100 V. Both instruments are controlled by a computer through GPIB communications. For a temperature-dependent measurement, a Lakeshore Temperature Controller is used.

Chapter 10

Organic Field-Effect Transistors with Single and Double Pentacene Layers

10.1 Introduction

Improving the performance of organic field-effect transistors (OFETs) has been a challenging to the development of the emerging organic electronics. Recent work has focused on OFETs based on single crystals [127]. While such studies are useful to elucidate the fundamental transport mechanism and the ultimate performance limit in organic semiconductors, practical devices are mostly based on thin films where the film morphology and the organic-insulator interface play an important role in device performance. It has been shown that accumulated charge carriers in thin-film OFETs are restricted to a few layers of organic molecules at the interface with the gate insulator [6, 5]. Thus investigating of the charge transport process at the level of a few molecular layers and a few crystalline grains represent a most direct way to understand the effect of microstructures and the gate-insulator interface on the transport properties. Frisbie *et al.* have fabricated OFETs with single grains of sexithiophene a few molecular layers in thickness [128]. Charge mobilities in these devices were a few orders of magnitude lower than bulk thin-film devices, which is attributed to the poor bottom contact which forms the bottleneck to charge transport. Dinelli *et al.* have studied the carrier mobility in ultrathin sexithienyl FETs as a function of film coverage and found that the mobility is dominated by the first two organic layers at the interface [129]. However, their devices consist of many grains and the effect of grain boundaries was not separated out.

In this chapter, we report on the fabrication and characterization of top-contact FETs based on individual grains of single and double pentacene layers grown on silicon dioxide using physical vapor deposition. The charge carrier mobility at room temperature extracted from the FET measurement is $0.01-0.04$ and $0.10-0.20$ cm^2/Vs for single- and double- layer devices with 560 nm thickness of SiO_2 gate oxide, respectively. The field-effect mobility from a single pentance film is improved to ~ 0.5 cm^2/Vs by utilizing a ~ 110 nm thickness gate oxide. The mobility increases with increasing gate voltage and shows a thermally activated form as a function of temperature, which are consistent with the multiple trapping and release model [114].

10.2 Device Fabrications and Measurements

Ultrathin pentacene films are deposited on silicon dioxide thermally grown on highly doped silicon wafers, which are employed as gate electrodes in FET measurements. Before deposition, the substrates are ultrasonically cleaned in nitric acid, acetone, and isopropanol, and subsequently annealed in a flow of Ar and H_2 at 900 °C for 30 min. Thorough cleaning is necessary to reduce nucleation centers promoting growth of large pentacene islands, whereas the H_2 annealing is known to reduce trap density at the Si/SiO_2 interface [64]. The pentacene source material is purified multiple times by temperature gradient sublimation. Figure 10.1 (a) shows a schematic of our growth setup. The physical vapor deposition is carried out in a 1-inch diameter glass tube placed in a horizontal tube furnace using nitrogen as a carrier gas. Nitrogen is

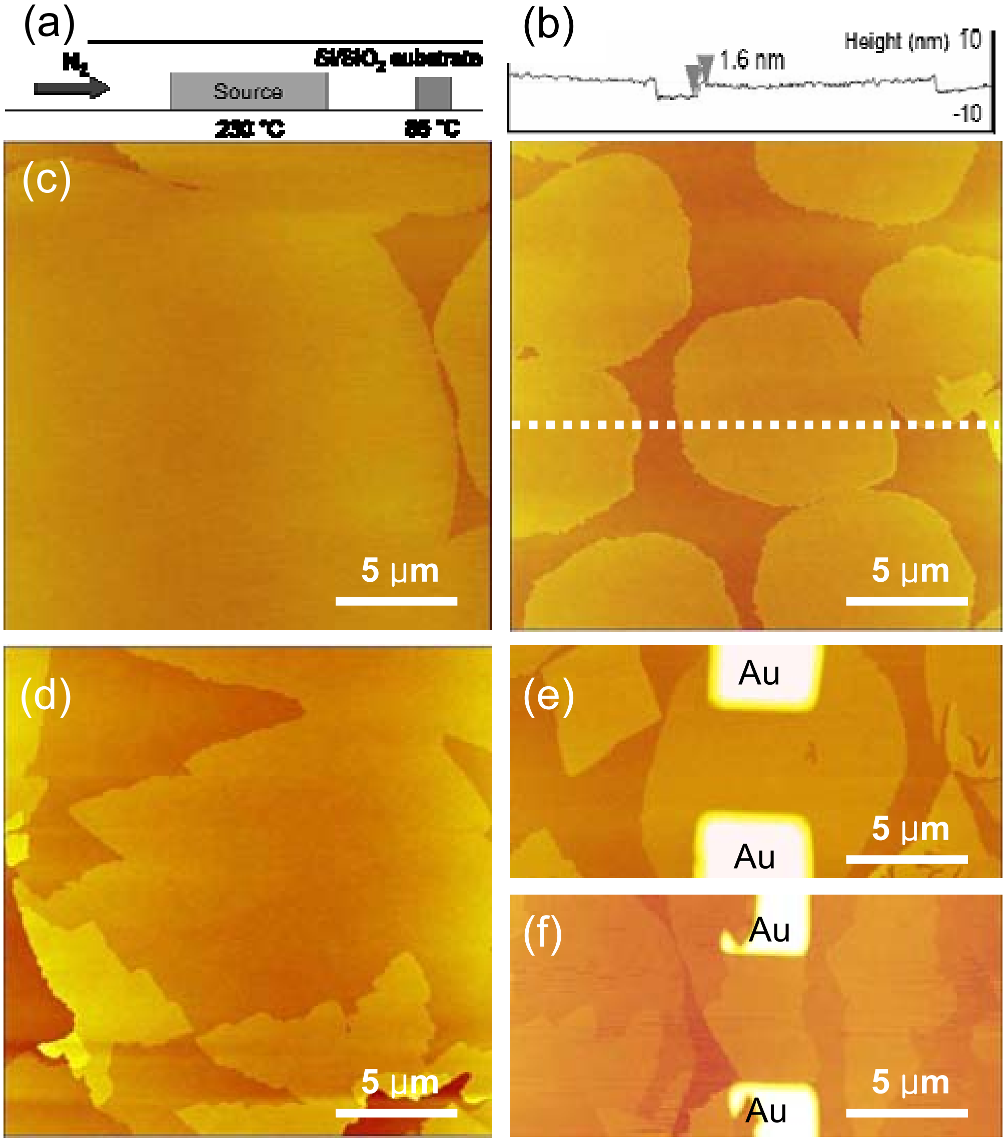

Figure 10.1: (a) Schematic diagram of physical vapor deposition setup. (b) AFM image of a pentacene single layer sample and a line scan height profile. (c),(d) AFM images of pentacene films with almost complete single-layer and double-layer coverage. (e),(f) AFM images of typical single- and double-layer devices

first flown for a few hours to dispense air and moisture from the growth tube. The source material is then heated up slowly, first to 200 °C at 2 °C/min, then to 230 °C at 5 °C/min. The sublimed molecules are carried by the nitrogen gas (flow rate 50 sccm) and are deposited on the substrates placed downstream at a temperature $\sim$ 85 °C. By controlling the growth time and the distance of the substrates to the source, we can fully control the size of the pentacene grains and the coverage of the thin films.

Figure 10.1 (b) displays a tapping mode atomic force microscopy (AFM) image of a sample with submonolayer coverage showing micron-size islands. It is well known that small rod-like molecules including pentacene stack almost perpendicularly to silicon oxide when deposited at elevated temperatures. The height of the islands as determined by the AFM line scan is consistent with the 1.6 nm length of the pentacene molecule, suggesting that these islands indeed consist of single layers of pentacene. The morphology of our samples is overall similar to the single crystalline single layers grown by vacuum sublimation by Fritz *et. al* [130]. By increasing the growth time, we can increase the coverage of pentacene in a layer-by-layer fashion. Figures 10.1 (c) and (d) show one sample with almost complete single-layer coverage and another with partial second layer coverage (which also has some third and fourth layers nucleated on top), respectively. The ability to control the growth of these ultrathin pentacene films offers the possibility to systematically investigate the charge transport characteristics as a function of the number of organic layers. The FET devices are fabricated by thermally evaporating $\sim$ 30 nm Au electrodes at a rate less than 0.5 $\mathring{A}$/s onto the thin films thorough a shadow mask fabricated in a suspended silicon nitride membrane. Figures 10.1 (e) and (f) are the AFM images of typical devices consisting of single and double pentacene layers, respectively. Although the devices have a channel width to length ratio of only $0.6 - 1.5$, the effect of fringe currents flowing outside the channel on the FET characteristics can be neglected as the size of the grains is comparable to the width of the channel. All the transport measurements are carried out in vacuum and darkness (unless specified) in a variable temperature cryostat.

10.3 Characterizations of Devices with Thick Gate Oxide

Figure 10.2 (a) shows room-temperature measurement of a single-layer device with 2.9 μm width and 4.9 μm length exhibiting well-behaved p-type FET characteristics including the linear regime at small source-drain voltage $|V_{sd}|$ and the saturation regime at $|V_{sd}|$ greater than the gate voltage $|V_g|$. The latter indicates that the contact resistance and fringe currents do not dominate the transport. Figure 10.2 (b) shows the transfer characteristic of the current I_{sd} as a function of V_g with a small V_{sd} of -10 V. The on-off ratio of this device is $\sim 10^5$. Following the standard FET model, the current in the linear regime obeys the following equation :

$$I_{sd} = \frac{W}{L} C_i \mu \left(V_g - V_t\right) V_{sd}, \tag{10.1}$$

where W and L are channel width and length, respectively, C_i the gate capacitance per unit area, μ the effective field-effect mobility, and V_t the threshold voltage [121]. Thus the field-effect charge carrier mobility can be obtained from the transconductance of the slope of the transfer characteristic. This procedure yields a field-effect mobility that increases monotonically with the gate voltage, as shown by the lower curve in Fig. 10.2 (c). Such gate-voltage-dependent mobility has been observed previously in thin film organic thin film transistors (OTFTs) and is attributed to trapping mechanisms [114]. Compared with previous results, the mobility in these devices does not saturate up to 100 V, the highest gate voltage that we have applied, presumably because of the thick gate oxide in these devices ($d_{ox} \simeq 560$ nm) [6, 131].

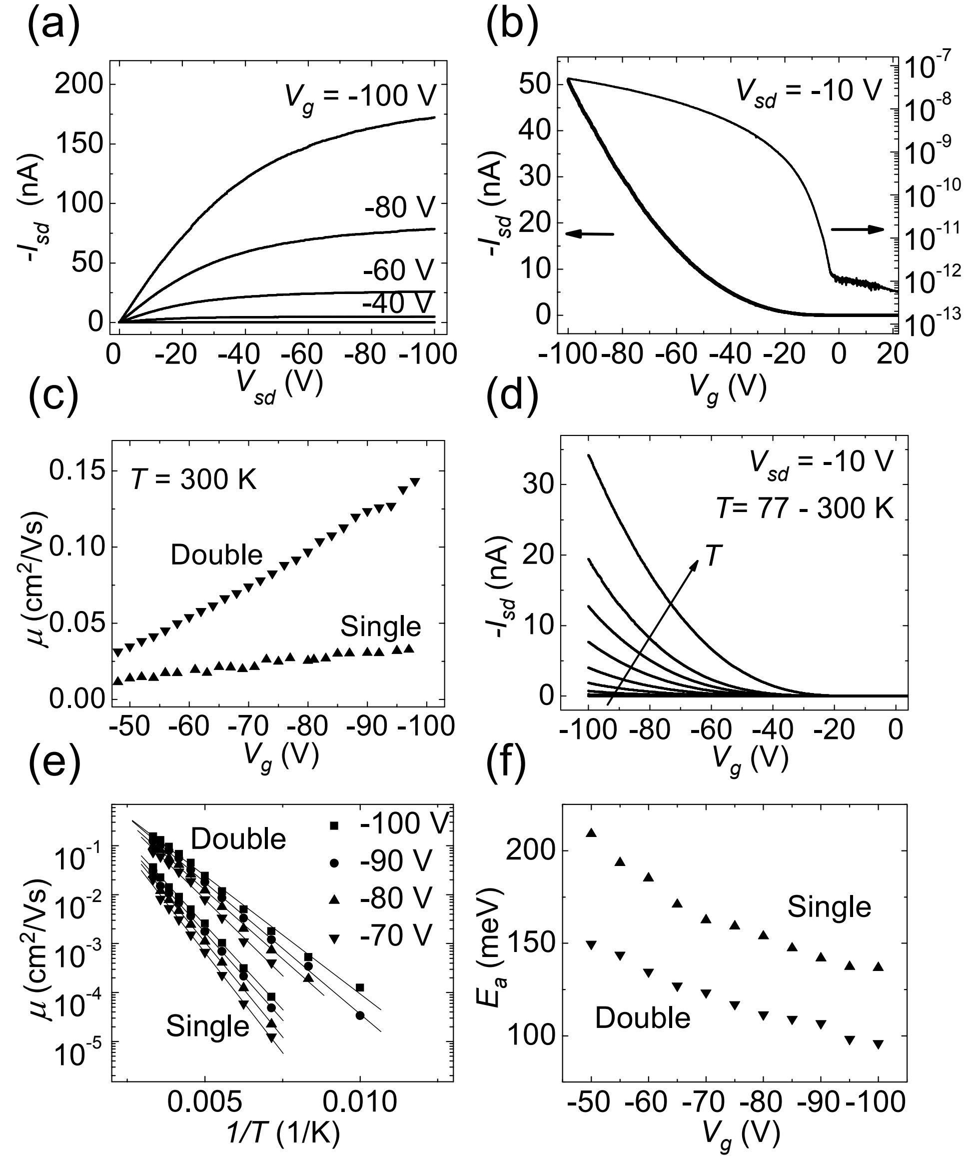

Figure 10.2: (a) I_d vs V_{sd} at various V_g for a pentacene single layer FET. (b) Plot of I_d vs V_g at a fixed $V_{sd} = -10$ V on both linear (left axis) and log (right axis) scales for a single layer device. (c) Mobilities vs V_g for typical single- and double-layer devices. (d) Plots of I_d vs V_g at a fixed $V_{sd} = -10$ V at different temperature from 77 to 300 K for the single layer device. (e) Mobilities vis inverse temperature at different V_g for single- and double-layer devices. Solid lines are fitting to Arrhenius' equation. (f) Activation energy at different V_g for single- and double-layer devices

The saturation behavior of a field-effect mobility is observed from other devices with a thin gate oxide ($d_{ox} \simeq 110$ nm). The detailed electric transfer characteristics for thin gate oxide OTFTs will be discussed at the later section in this chapter.

The mobility extracted at $V_g = -100$ V is 0.033 cm^2/Vs and is almost two orders of magnitude lower than the value for the best pentacene thin film devices [132]. Interestingly, double-layer devices show consistently higher mobilities. An example of gate-dependent mobility for a double-layer devices is shown in Fig. 10.2 (c) with the mobility approaching 0.145 cm^2/Vs at $V_g = -100$ V. We have studied more than 15 single-layer devices and 10 double-layer devices fabricated on the same silicon oxide (some consisting of channels partially covered by the second layer). The mobility at $V_g = -100$ V is $0.01 - 0.04$ cm^2/Vs for single-layer devices and is $0.05 - 0.20$ cm^2/Vs for devices with complete or partial double layers.

To gain more insight into the charge transport mechanism, we have characterized the carrier mobility as a function of temperature. Figure 10.2 (d) shows the transfer characteristic of a single-layer device measured at $V_{sd} = -10$ V between 77 K and room temperature. The current decreases monotonically as decreasing temperature. Qualitatively similar behavior has been observed in all measured devices. The extracted mobility as a function of both temperature and gate voltage is plotted in Fig. 10.2 (e) for representative single- and double-layer devices. The data can be fit well with Arrhenius' equation:

$$\mu = \mu_0 \exp\left(-\frac{E_a}{k_B T}\right), \tag{10.2}$$

where E_a represents the activation energy and k_B is Boltzmann's constant. The activation energy obtained from fitting is in the range range of $137 - 210$ meV for the single-layer device and $96 - 150$ meV for the double-layer device. At the same gate voltage, the activation energy of the double-layer device is ~ 40 meV lower than that of the single-layer device.

10.4 Data Analyses and Discussions

10.4.1 Multiple Trapping and Release Model

Our results can be understood by the multiple trapping and release (MTR) model [114]. MTR has been used to explain similar gate-voltage-dependent mobility observed in hydrogenated amorphous silicon [133, 134]. This model assumes a distribution of trap states in the forbidden energy gap above the valence band edge. At low gate voltage, most of the holes injected from the source become trapped in the localized states and do not contribute to charge transport. As the gate voltage is increased, more traps are filled and the Fermi energy E_F gradually move closer to the valence band edge E_V. The density of free carriers thermally released from the trap states to the valence band is steadily increased accordingly. Thus the effective carrier mobility is the free carrier mobility reduced by the fraction of charged carriers that are trapped and therefore shows an Arrhenius-type form for the temperature dependence.

10.4.2 Calculation of Density of Trap States

To gain more insight on trapped states in single- and double-layer OFETs, we quantitatively analyze localized states formed inside the forbidden energy gap. We followed the method developed by Le Comber for amorphous silicon [135] and Horowitz for the organic semiconductor sexithiophene [136].

In MTR, all induced charges are assumed to be trapped at localized states in the forbidden energy gap. Therefore, the total surface charge σ is expressed by

$$\sigma = \sigma_t + \sigma_f \approx \sigma_t \approx C_i V_g \; , \tag{10.3}$$

where σ_t and σ_f are trapped and free surface charges, respectively. From the Boltzmann statistics, the free surface charge σ_{f} is expressed by

$$\begin{aligned}\sigma_f &= \sigma_{fo}\exp\left(\frac{eV_s}{k_BT}\right) = eN_v\exp\left(-\frac{E_{fo}-E_v}{k_BT}\right)\exp\left(\frac{eV_s}{k_BT}\right) \\ &= eN_v\exp\left(-\frac{E_{fo}-E_v-eV_s}{k_BT}\right) = eN_v\exp\left(-\frac{E_f-E_v}{k_BT}\right).\end{aligned} \tag{10.4}$$

Here σ_{fo} is the free surface charge at $V_g = 0$ V, and N_v is the surface density of states at the valence band edge. V_s represents the potential at the interface between gate insulator and organic semiconductor. E_v is the valence band energy, and E_{fo} is the quasi Fermi energy level at equilibrium. The modified quasi Fermi level E_f is expressed by a function of the surface potential V_s :

$$E_f = E_{fo} - eV_s. \tag{10.5}$$

The field-effect mobility measured in electric FET experiments is limited to the free charges carriers. Therefore, only a part of gate-induced charges contributes to charge transport. The field-effect mobility (μ_{FET}) can be expressed by the ratio of total charges and free carriers :

$$\mu_{\mathrm{FET}} = \mu_o\frac{\sigma_f}{\sigma_t+\sigma_f} \approx \mu_o\frac{\sigma_f}{\sigma_t} = \mu_o\frac{\sigma_f}{C_iV_g}. \tag{10.6}$$

Combining Eq. (10.4) and (10.6), the quasi Fermi level with respect to the valence band edge is expressed by

$$E_f - E_v = k_BT\ln\left(\frac{eN_v\mu_o}{\mu_{\mathrm{FET}}C_iV_g}\right). \tag{10.7}$$

The total trapped charges are connected to the surface density of localized states

N_t by

$$\sigma_t = e\int_{-\infty}^{+\infty} N_t(E)f(E)dE = C_iV_g, \tag{10.8}$$

and in the case of a slowly varying function like $N_t(E)$, it can be approximated by

$$N_t(E) \approx \frac{1}{e}\frac{d\sigma_t}{dE} \approx \frac{1}{e}\frac{C_i\Delta V_g}{\Delta E}. \tag{10.9}$$

With the help of Eq. (10.7) and (10.9), the density of trapped states can be obtained. The field-effect mobility expressed in Eq. (10.6) can be written as Arrhenius' equation form :

$$\mu_{\mathrm{FET}} = \mu_o\frac{\sigma_f}{\sigma} = \mu_o\frac{eN_v}{C_iV_g}\exp\left(-\frac{E_f - E_v}{k_BT}\right) = \mu_o^{'}\exp\left(-\frac{E_a}{k_BT}\right), \tag{10.10}$$

where activation energy is defined by $E_a = E_f - E_v$, and free carrier mobility μ_o is obtained by $\mu_o = \mu_o^{'}(C_iV_g/eN_v)$. The activation energies and modified free carrier mobilities ($\mu_o^{'}$) can be extracted from temperature-dependent measurements, as shown in Fig. 10.2 (e). Experimentally determined activation energies are further compared with calculated values from Eq. (10.7) using $N_v\mu_o$ as a fitting parameter :

$$E_a = E_f - E_v = k_BT\ln\left(\frac{eN_v\mu_o}{\mu_{\mathrm{FET}}C_iV_g}\right). \tag{10.11}$$

The density of localized states in both amorphous silicon [133] and organic semiconductor sexithiophene [6] is often represented by a double exponential distribution. The form of an exponential trap distribution is expressed by

$$N_t(E) = \frac{N_{to}}{k_BT_c}\exp\left(-\frac{E - E_v}{k_BT_c}\right), \tag{10.12}$$

where N_{to} is the total surface density of localized states, and T_c is the element representing the steepness of trap distribution. Accordingly, the total trapped charge density can be obtained by

$$\begin{aligned} \sigma_t &= e\int_{E_f}^{+\infty} \frac{N_{t0}}{k_B T_c} \exp\left(-\frac{E-E_v}{k_B T_c}\right) dE \\ &= \sigma_{t0} \exp\left(\frac{eV_s}{k_B T_c}\right), \end{aligned} \tag{10.13}$$

where σ_{to} is the trapped charge density at equilibrium ($V_g = 0$ V). Finally, the field-effect mobility as a function of gate voltage is analytically expressed by

$$\begin{aligned} \mu_{\text{FET}} &= \mu_0 \frac{N_v}{N_{t0}} \exp\left[-(E_{f0} - E_v - eV_s)\left(\frac{1}{k_B T} - \frac{1}{T_c}\right)\right] \\ &= \mu_0 \frac{N_v}{N_{t0}} \left(\frac{\sigma_t}{eN_{t0}}\right)^{(T_c/T-1)} = \mu_0 \frac{N_v}{N_{t0}} \left(\frac{C_i V_g}{eN_{t0}}\right)^{(T_c/T-1)}. \end{aligned} \tag{10.14}$$

10.4.3 Distribution of Trap States in Single- and Double-Layer Pentacene Devices

Figure 10.3 shows the analytical results for both single-layer (sample I) and double-layer (sample II) devices. The capacitance per unit area is $C_i = 6.16 \times 10^{-9}$ F/cm^2 considering $d_{ox} \simeq 560$ nm gate oxide thickness. For analytical calculations, the additional turn on gate voltage V_{on} is introduced to compensate for the FET off-states. Below V_{on}, all induced charges are trapped deep inside the localized states. In this regime, the electronic signals from thermally released charges are extremely small, so that they are masked by noises such as the leakage current through the gate oxide. The effective gate voltage is given by $V_g' = V_g - V_{on}$, where V_{on} for single- and double-layer devices is -12 V and -6 V, respectively.

The field-effect charge carrier mobility is obtained from the transconductance of the transfer characteristic in the linear regime ($V_{sd} \ll V_g$). In addition, activation energies E_a at different gate voltages can be extracted from temperature dependent

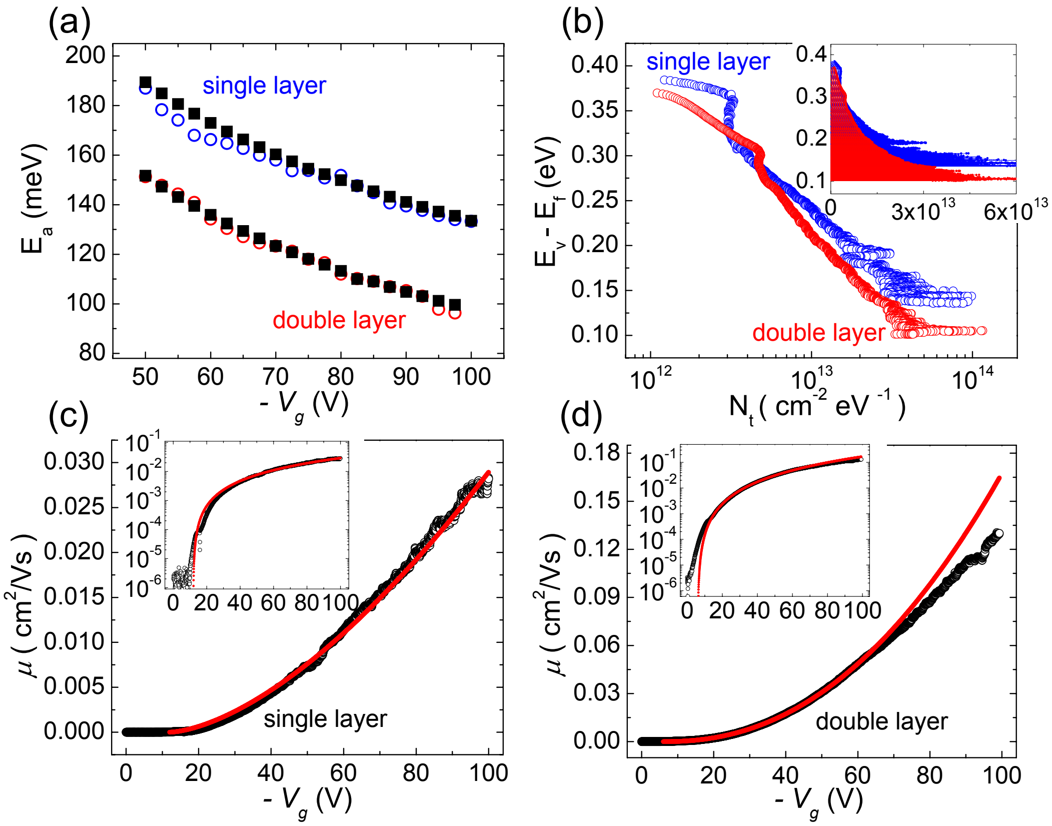

Figure 10.3: (a) Activation energies of single- and double-layer devices as a function of gate voltage. Open circles represent experimental data and closed black squares represent analytical calculation. (b) Calculated density of trap states of single- and double-layer devices.(inset) Same density of trap states plot as a linear scale of trap density. (c), (d) field-effect mobility as a function of gate voltage extracted from both experimental data (black open circles) and analytical calculation (red lines) for single- and double-layer devices. (inset) Same plots as a log scale of field-effect mobilities.

measurements performed in the range 80 K $\leq T \leq$ 300 K. The extracted mobilities can now be fitted by Arrhenius's equation as a function of temperature, and the activation energies at different gate voltages are obtained from the fitting. The activation energy can also be analytically calculated from Eq. (10.11) using μ_{FET} measured at a fixed temperature (T=300 K) with an adjustable parameter, $\mu_o N_v$.

The best agreement between activation energies extracted from temperature measurements and analytical results is obtained with $\mu_o N_v = 1.7 \times 10^{13}$ V^{-1}s^{-1} for sample I (single-layer), and $\mu_o N_v = 2.2 \times 10^{13}$ V^{-1}s^{-1} for sample II (double-layer). The open circles in Fig. 10.3 (a) represent data from temperature measurements and closed black squares from the theoretical calculations.

Once we find the adjustable parameter $\mu_o N_v$, we can calculate the density of trap states inside the forbidden energy gap using Eq. (10.9). The density of trap states for sample I and II are plotted in Fig. 10.3 (b). Both trap states can be represented by exponential trap distributions as expressed in Eq. (10.12). The total surface density of trap states N_{to} is 2.2×10^{13} for the single- and 1.1×10^{13} cm^{-2}eV^{-1} for the double-layer device. In addition, the double-layer device exhibits a narrower distribution of traps than the single-layer device. The characteristic temperatures for the trap distribution formed in the single- and double-layer device are $k_B T_c = 83.6$ meV and $k_B T_c = 67.2$ meV, respectively.

The field-effect mobilities plotted in Fig. 10.3 (c) and (d) show that the analytical expression obtained from the multiple trapping and release model can successfully represent the experimental data for both single- and double-layer devices. The black open circles are for the mobilities extracted from the transfer characteristic relation in Eq. (10.1) at 300 K, and the red line is from the direct calculation with the analytical solution of the mobility Eq. (10.14). The key parameters for the single- (sample I) and double-layer (sample II) devices are summarized in the Table 10.1.

The fact that the double-layer device has a smaller density of trap states and narrower distribution can explain the consistent higher mobility. The origins of the traps in pentacene OTFTs have not been well established. They are believed to be mainly caused by structural imperfections and chemical impurities. Since our devices are made within single pentacene islands, grain boundaries are unlikely to be the source of traps. Once grain boundaries are formed, however, the effect is quite conspicuous, and it is confirmed by electronic force microscopy (EFM) studies in Chapter 11. The difference in the trap densities for single- and double-layer devices points to the effects of the gate oxide and exterior conditions. Considering that the highest mobility is obtained from the device with chemically treated gate electrodes [113, 137], and double-layer FETs have smaller trap states than single-layer, we can claim that the interface of $\mathrm{SiO_2}$/pentacene is responsible for the localized trap states in pentacene OTFTs. The second layer of double-layer devices is expected to have better molecular ordering, so it could have less structural defects and vacancies.

In addition, the effects from metallization process and ambient conditions are believed to be partly responsible for the localized states. Since the conduction channel is directly exposed to exterior environments for our ultrathin layer OTFTs, the localized states induced from structural imperfections and chemical reactions are easily introduced to the conduction channels. The effects from metal contacts are directly observed by EFM studies, and it has been found that metal contacts are as equally responsible for the trap states as gate oxide interface.

Table 10.1: Key parameters for single- and double-layer devices

	V_{on} (V)	$\mu_o N_v$ ($\mathrm{V^{-1}s^{-1}}$)	$k_B T_c$ (meV)	N_{to} ($\mathrm{cm^{-2}eV^{-1}}$)
Sample I (single)	-12	1.7×10^{13}	67.2	2.5×10^{13}
Sample II (double)	-6	2.2×10^{13}	83.6	1.1×10^{13}

10.5 Characterizations of Devices with Thin Oxide

10.5.1 Current-Voltage Characteristics

In the MTR model, the field-effect mobility increases with increasing gate voltage, as shown in samples I and II. As more trap states are filled, however, the field-effect mobility is expected to saturate to a certain value. We can access that saturation regime by improving the gate couplings in OTFTs. One way to achieve this is to introduce high dielectric gate insulators. Several OTFTs incorporated with high-dielectric materials have been studied [131, 138]. Alternatively, one can also decrease the thickness of the gate insulator [131, 139]. Since our ultrathin pentacene film is sensitive to the choice of gate insulator, the second way is the more suitable choice to improve gate coupling for our device.

We prepared a new batch of devices with $d_{ox} \simeq 110$ nm gate oxide. By doing this, we can improve the gate coupling of the OTFTs by five times. The electric measurements shown in Fig. 10.4 and 10.5 are from the device whose channel is partially covered with double-layer film with 4.82 μm width and 4.78 μm length. Since the coverage of double-layer film is no more than 7 % of the channel area, the electric transport behavior is expected to be the same as that of single-layer devices, and the extracted trap distribution and activation energy are consistent with those from the single-layer device (sample I). The detailed analysis is presented later, and we refer to this thin oxide device as sample III.

Figure 10.4 (a) shows room-temperature measurements of sample III exhibiting well-behaved p-type FET characteristics. At small V_{sd}, the I_{sd} follows the linear transfer characteristic given by Eq. (10.1). Figure 10.4 (b) shows the I-V transfer characteristic as a function of V_g with a V_{sd} of -2 V. The on-off ratio of this thin-oxide FET is improved by a factor of $\sim 10^6$ compared with thick oxide devices. When V_{sd} is greater than the gate voltage V_g, the I_{sd} enters the saturation regime.

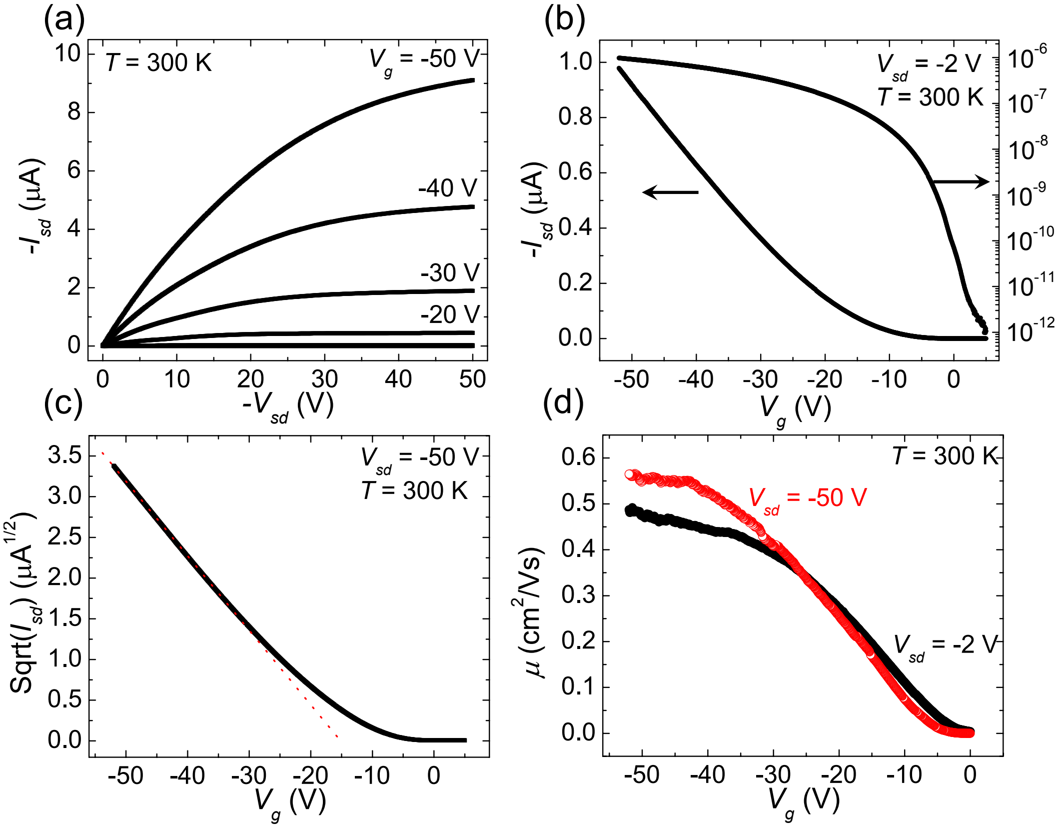

Figure 10.4: (a) I_{sd} vs V_{sd} at various V_g for a pentacene OTFT. (b) Plot of I_{sd} vs V_g at a fixed $V_{sd} = -2$ V in both linear (left axis) and log (right axis) scales. (c) $\sqrt{I_{sd}}$ vs V_g at the saturation regime, $V_{sd} = -50$ V.(d) Field-effect mobility μ vs V_g extracted from both the linear regime (black dots, $V_{sd} = -2$ V) and the saturation regime (red dots, $V_{sd} = -50$ V).

The current in the saturation regime can be expressed by

$$I_{sd,sat} = \frac{W}{2L} C_i \mu \left(V_g - V_t\right)^2 . \tag{10.15}$$

The threshold voltage V_t can be directly extracted from the current measured in the saturation regime. As shown in Fig. 10.4 (c), V_t for sample III is -15 V, obtained from the slope of $\sqrt{I_{sd,sat}}$.

The black circles in Fig. 10.4 (d) represent field-effect mobility extracted from Eq. (10.1) in the linear regime. In addition, the field-effect mobility can be obtained from the *I*-*V* characteristics in the saturation regime :

$$\mu_{\mathrm{FET}} = \frac{2L}{W} \frac{1}{C_i} \left(\frac{\partial \sqrt{I_{\mathrm{sd,sat}}}}{\partial V_g} \right)^2 . \tag{10.16}$$

The mobility calculated in the saturation regime is displayed as red circles in Fig. 10.4 (d). Since the current at higher gate voltage, $V_g \geq -40$V with $V_{sd} = -50$ V as a bias voltage, is in the transition regime between the linear and the saturation regimes, the mobility extracted from the saturation regime is usually higher than the value from the linear regime, but they are reasonable agreed with each other at lower gate voltage, as shown in Fig. 10.4 (d).

As expected from the MTR, the field-effect mobilities in both linear and saturation regimes monotonically increase with increasing gate voltage. However, the mobilities start showing quasi-saturation behavior at high gate voltage, and the measured highest mobility is close to ~ 0.5 cm^2/Vs, which is similar to the highest mobility ~ 1.0 cm^2/Vs measured from bulk pentacene films [113, 137].

10.5.2 Temperature Dependence and Data Analyses

We further characterized the transfer characteristics of sample III as a function of temperature. Figure 10.5 (a) shows the transfer characteristic curves in the linear

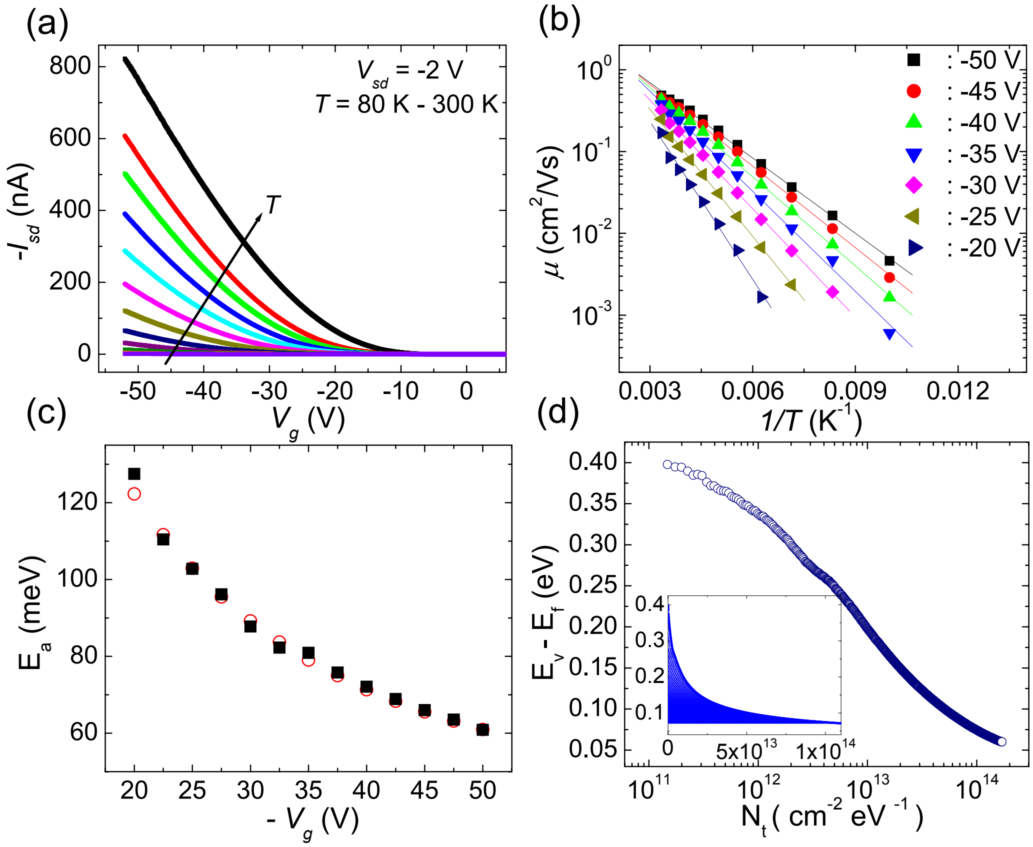

Figure 10.5: (a) Plots of I_{sd} vs V_g at a fixed $V_{sd} = -2$ V at different temperatures from 80 to 300 K for sample III. (b) Mobilities vs inverse temperature at different V_g. Solid lines are fitting to Arrhenius$'$ equation. (c) Activation energy at different V_g. Open red circles are from experimental data and closed black squares are for analytical fitting results. (d) Calculated density of trap states of sample III. (inset) Same plot as a linear scale of trap density.

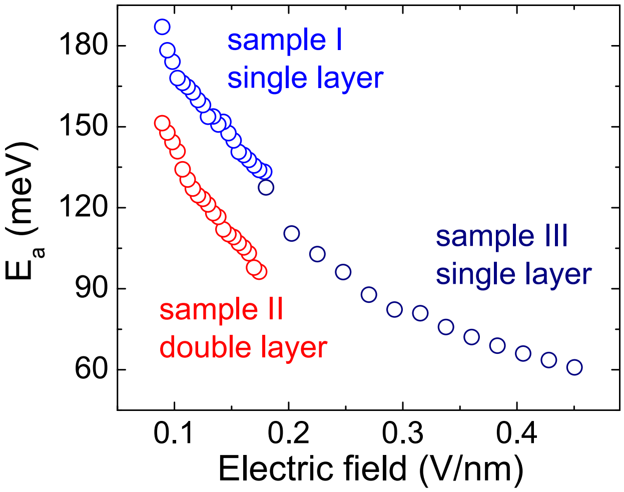

Figure 10.6: Activation energy as a function of gate electric field for single-layer devices (samples I and III) and double-layer device (sample II).

regime between 80 K and room temperature. The field-effect mobilities extracted at different gate voltages and temperatures are plotted in Fig. 10.5 (b), and they are well fitted to Arrhenius' equation. The activation energies obtained from the fitting are plotted in Fig. 10.5 (c) as red open circles, and the analytically calculated values using Eq. (10.11) with a fitting parameter $\mu_o N_v = 5.3 \times 10^{13}$ $\mathrm{V}^{-1} s^{-1}$ are presented as closed black squares. Both experimental and theoretical calculation data are in good agreement across measured gate voltage range. Figure 10.5 (d) shows the calculated density of localized states in the forbidden gap for sample III, and the characteristic temperature $k_B T_c$ is 66.4 meV, which is close to 67.2 meV for the single-layer device with thick oxide. Thus, the origin of traps formed at sample III is similar to that of the single-layer device I. We plot activation energies obtained from samples I, II and III as a function of gate electric field, as shown in Fig. 10.6. Sample III indeed shows an extended regime of the single-layer device, sample I, which is another confirmation that the trap states in sample III have the similar origins with sample I.

By improving the gate coupling, we can access the transport regime of bulk film OTFTs with the single-molecular layer of pentacene film, and this is the direct observation that gate-induced charges are indeed accumulated in the first layer of bulk films [6, 5].

10.6 Summary

In summary, we have characterized OTFTs based on individual grains of single and double pentacene molecular layers grown on silicon oxide. Field-effect mobility exhibits gate voltage dependence and thermally activated form in the temperature dependence. The behavior can be understood from a multiple trapping and release model. Double-layer devices show consistently higher mobilities and lower activation energies than single-layer devices, and the localized states formed at single-layer films show deeper and steeper distributions in the forbidden energy gap. It is proposed that the structural disorders induced from the gate insulator and metallization process in the molecular layers is partly responsible for the traps. The field-effect mobility shows saturation behavior at high gate electric field when the majority of trap states are filled. The highest mobility from the single layer pentacene device is measured to be ~ 0.5 cm^2/Vs.

Chapter 11

Electric Force Microscopy Studies of Charge Transport in Few Layer Pentacene Transistors

11.1 Introduction

A useful method to characterize charge transport behaviors in pentacene organic field-effect transistors (OTFTs) is to monitor charge distribution along the conduction channel when OTFTs are in active. The surface potential profile of pentacene OTFTs has been reported by Puntambekar *et al.* [140], utilizing the Kelvin probe force microscopy (KFM) technique. In their report, the importance of metal contact to pentacene film has been pointed out. Most of the voltage drop occurred at contact areas for the bottom-contacted device, but the applied voltage was linearly decreased across the conduction channel for the top-contacted device. In bulk film devices as in Ref. [140], however, the actual transport channel is placed deep inside the organic film [6, 5]. Therefore, it is impossible to directly correlate the KFM signals with the device parameters, such as metal contacts, grain boundaries, and surface morphology of the real conducting channel. In addition, different numbers

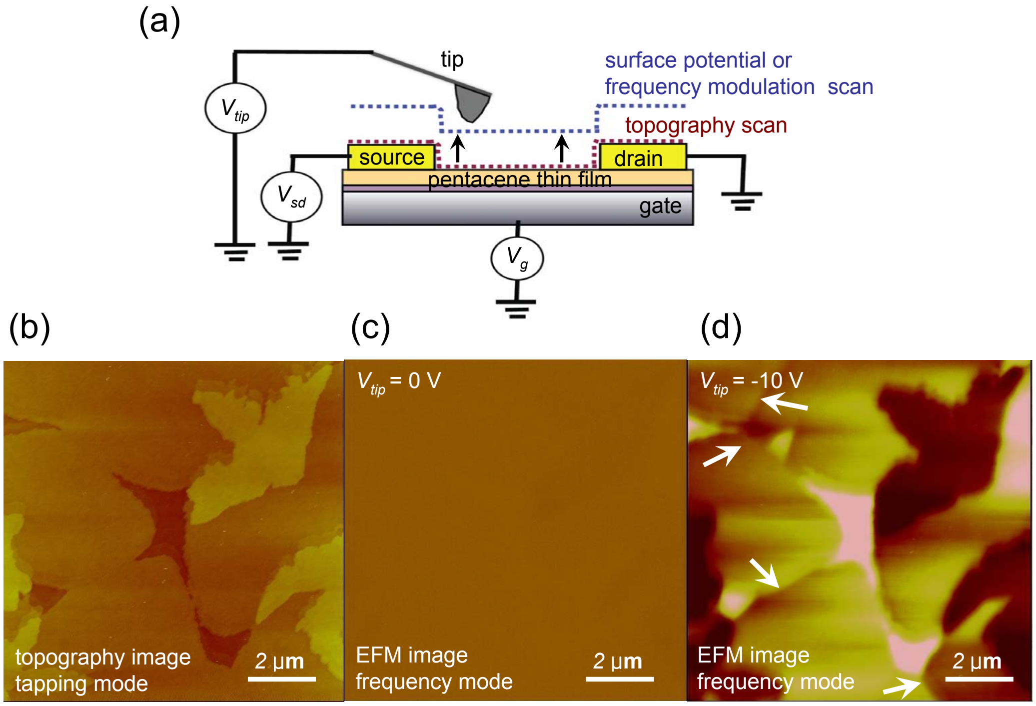

Figure 11.1: (a) Schematic diagram of EFM scan of organic field effect transistors. (b) Topological AFM image of pentacene thin film in tapping mode. EFM images of pentacene thin film with a conducting tip biased at (c) $V_{\text{tip}} = 0$ V and (d) $V_{\text{tip}} = -10$ V in frequency mode.

of organic semiconducting layers in OTFTs has been demonstrated to show different transport characteristics [128, 117]. From this perspective, our single- and double-layer pentacene OTFTs are excellent candidates for surface imaging studies, since we can directly relate observed signals to the device structures of pentacene OTFT conducting channels.

11.2 Electric Force Microscopy Studies of Pentacene

11.2.1 Electric Force Microscopy

Figure 11.1 (a) shows a schematic diagram of a pentacene thin film field-effect transistor (FET) with an electric force microscopy (EFM) setup. EFM is performed by either electric field gradient (frequency or phase mode) or KFM mode of a Digital Instruments (DI) Multimode AFM equipped with a signal access and a extender electronic module. We use either Cr/Au coated or bare silicon tips. First, the topography information of ultrathin pentacene OTFTs is obtained in tapping mode as shown in Fig. 11.1 (b). After finishing each line scan, the tip is lifted by a pre-defined height and rescans the same line. This process is called lift-mode. In lift-mode, the feedback control is used to maintain the height at a predefined value ($\leq$ 100 nm) to remove topological information. New sets of data such as the frequency or phase shift of the tip oscillation, which is proportional to the electric force in between tip and sample, is recorded during the lift-mode scan. The surface potential of the sample can be directly imaged by the feedback controller as well. In KFM mode, the feedback controller adjusts the voltage on the tip to keep the amplitude of tip oscillation zero. Since the tip oscillation depends on the voltage difference between the tip and the sample, the surface potential profile of the sample can then be obtained. All of our EFM studies are performed in air at room temperature.

In phase mode, the EFM signal does not show any topography information of either film or silicon dioxide when the voltage on the tip is biased at zero as shown in Fig. 11.1 (c). The topological AFM image of the pentacene thin film exhibiting single- and double-layer coverage is shown in Fig. 11.1 (b). However, the phase difference starts showing up when the tip voltage is increased. As shown in Fig. 11.1 (d), the clear difference between the single- and double-layer coverage of pentacene film is recognizable. Since there are no gate-voltage-induced charges in the films with zero gate voltage, the EFM signal difference is attributed to the static charges in pentacene films, which suggests the electronic states in single- and double-layer films are different even in equilibrium. More interestingly, grain boundaries are prominently visible in the EFM measurement. Most grain boundaries, indicated by white arrows in Fig. 11.1 (d) are not visible in the topography AFM image. Thus, the outright EFM signals from the grain boundaries suggest that the electronic properties at grain boundaries are also different from those inside pentacene single grains. To gain more insight on the effect from grain boundaries to charge transport, we performed EFM measurements with the devices whose conducting channel is formed with a couple of grains.

11.2.2 Effect of Grain Boundary on Charge Transport

Figure 11.2 shows the dramatic effect of a grain boundary on the charge transport through pentacene thin film (sample I). As indicated by a white arrow in the AFM topography image displayed in Fig. 11.2 (a), a grain boundary is formed within the conduction channel. The EFM signals shown in Fig. 11.2 (b) and (c) are recorded in frequency mode with $V_{tip} = 1$ V. The surface potential profile displayed in Fig. 11.2 (c) and (d) are the converted data from the raw frequency modulations. The frequency shift is proportional to the electric force on the tip, which is a function of the surface potential of the sample V_{sample}, and a tip voltage :

$$\Delta f \propto \left(V_{tip} - V_{sample} + \Delta\Phi\right)^2 , \tag{11.1}$$

where $\Delta\Phi$ is the potential difference in equilibrium ($V_{sample} = V_{tip} = 0$). Thus, we can obtain the surface potential of the sample by comparing the measured frequency shift at the source and drain electrodes with the applied voltages on them, i.e., -5 V at the source electrode, and 0 V at the drain as shown in Fig. 11.2 (a).

As shown in Fig. 11.2 (b), when there is no current flowing through the channel, no conspicuous effect is appeared except background modulations. However, the

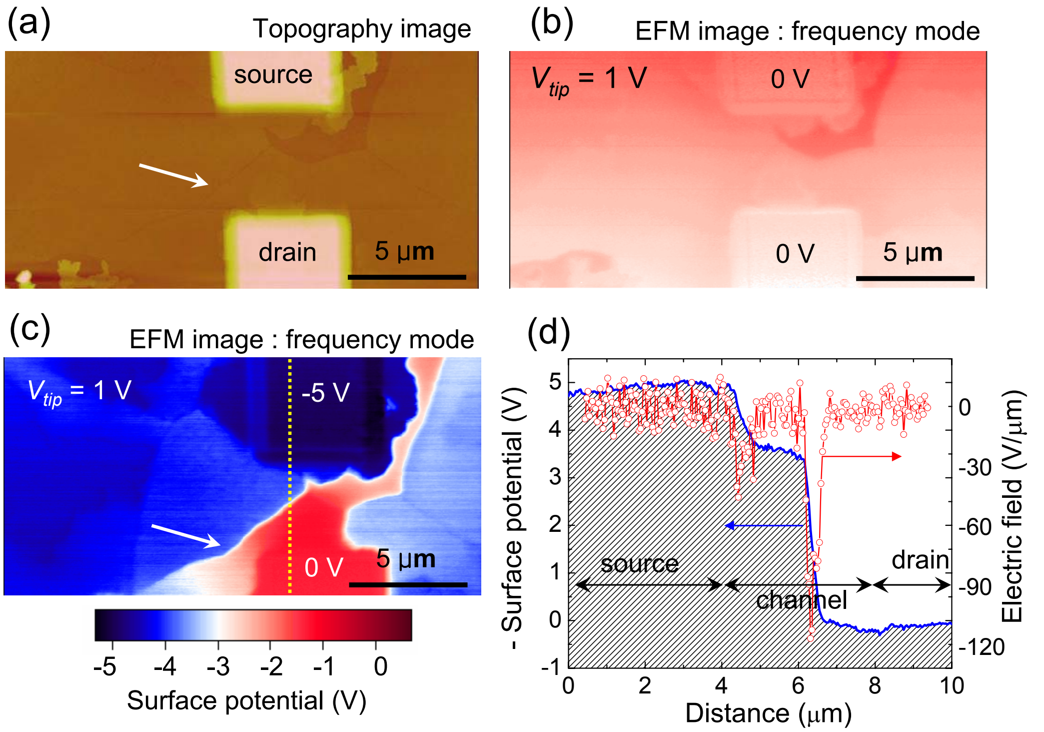

Figure 11.2: (a) Topological AFM image of the single-layer device (sample I) with a grain boundary in the conducting channel. Grain boundary is indicated by a black arrow. (b), (c) EFM images in frequency mode. (d) The profile of converted surface potential and electric field across the grain boundary marked by a yellow dotted line.

effect of the grain boundary goes prominent when the current through the device is increased. The current through the channel is ~ 1 nA when the source electrode is biased with $V_{sd} = -5$ V. As shown in Fig. 11.2 (d), $\sim 80\%$ of the applied voltage is measured to drop at the grain boundary, which means the grain boundary is responsible for the $\sim 80\%$ of device resistance. There is also a noticeable resistance development at the area of source metal contact, but it is fairly small compared to the voltage drop at the grain boundary. The effect of grain boundaries on charge transport in OTFTs was studied previously from the current-voltage ($I - V$) characteristics with organic semiconductor sexithiophene (6T) by Chwang *et al.* [110], and they also showed that charge transport through OTFTs was severely limited by the grain boundary. By probing the OTFT conducting channel, i.e., single-layer pentacene film, with EFM, we can further confirm that grain boundaries are by far the most dominant resistance sinks in OTFTs.

Once OTFT conduction channels are free from grain boundaries, more than half of the biased voltage is observed to drop at the metal contacts. Figure 11.3 (a) shows the AFM image of the device (sample II) whose conducting channel is made up with double-layer pentacene films without grain boundaries. Figures 11.3 (b) and (c) show the surface potential profiles of sample II obtained in KFM mode in DI Multimode SPM. The upper electrode is biased at $V_{sd} = -10$ V in Fig. 11.3 (b), and the lower electrode is biased at $V_{sd} = -10$ V in 11.3 (c). The surface potential profiles shown in Fig. 11.3 (b) and (c) turn out almost identical notwithstanding the polarities of bias voltage. The measured KFM signal is scaled down by $\sim 40\%$ of actual applied voltage to the device because of the convolution effect of the tip. As plotted in Fig. 11.3 (e), $\sim 70\%$ of the bias voltage is dropped at the metal contacts. In reversed current, the same amount of voltage drop is observed at the contact areas as shown in Fig. 11.3.

Interestingly, our observation is different from the previous report by Pun-

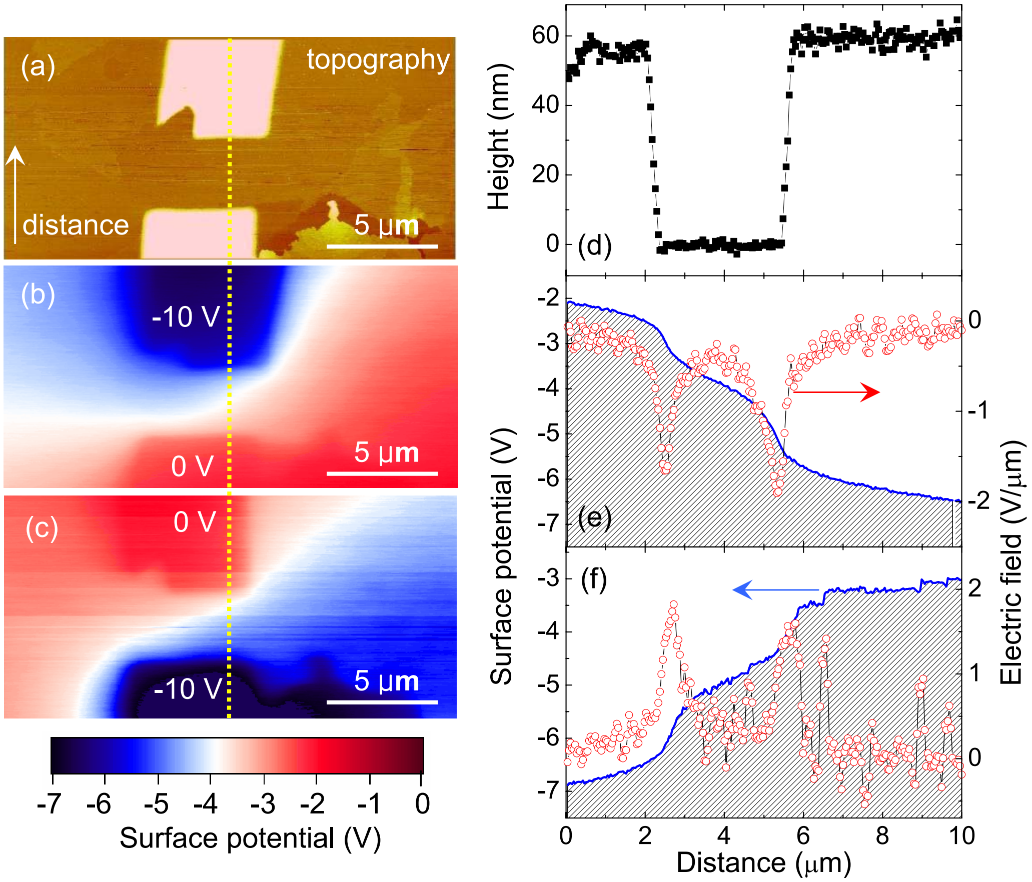

Figure 11.3: (a) Topological AFM image of the double-layer device (sample II) without grain boundaries. (b), (c) Surface potential images with biased $V_{\rm sd} = -10$ V at the top or bottom electrode, respectively. (d) Height profile scanned across the channel. Surface potential and calculated electric field profiles across the channel following the yellow dotted line biased at (e) upper electrode and (f) lower electrode, respectively.

tambekar *et al.* [140]. In their observations, negligible voltage was dropped at the metal contact areas when the contacts were made on top of organic films, i.e., top-contact scheme, as in our devices. On the contrary, the surface potential profiles of sample II look similar to their measurements with the device where the organic film was deposited on top of pre-fabricated metal electrodes, i.e., bottom-contact scheme. We believe that in their top-contact scheme, even though the contact was made on top of the deposited pentacene films with 30 $\sim$ 50 nm in thickness, the first few pentacene layers on top of the gate oxide, in which most of charge transport occurs, are not affected by the metal contacts. This is likely the reason for negligible voltage drop at the metal contacts in their top-contact measurements. On the contrary, the conduction channel is directly affected by the presence of the metal contacts in their bottom-contact devices, and this is exactly what happens in our ultrathin pentacene layer devices, even though we employed top-contact schemes.

It is interesting to point out that among $\sim$ 70% voltage drop at the metal contacts, the drop at the area of source electrode is measured to be bigger than that at the drain electrode. As shown in Fig. 11.3 (e), almost $\sim$ 45% of the applied voltage is dropped at the upper electrode at which $V_{sd} = -10$ V is applied, and the rest $\sim$ 25% out of 70% is dropped at the lower electrode. When the polarity of biased voltage is reversed as shown in Fig. 11.3 (f), $\sim$ 40% of the bias voltage is dropped at the lower electrode contact, which now serve as a source electrode. The remaining $\sim$ 30% is dropped at the grounded upper electrode. Similar anisotropic voltage drops at the source and drain electrodes are also seen in the bottom-contact device in Ref. [140], which suggests injecting charged carriers to the OTFT channel is easier than extracting from the channel. More studies are necessary to address the detailed physical mechanisms of charged carrier injection and extraction in between OTFTs and metal electrodes.

In these observations, it is apparent that charge transport through organic films is contact limited. It is not difficult to imagine the physical damage on pentacene molecular layers during the metal electrode fabrication. Even though the evaporation rate of Au is maintained very low at $\leq 0.5\mathring{A}/s$, the structural damages from metal particle intrusion and heat damages from the thermal evaporation method cannot be avoided. The electrode fabrication with soft-printing techniques could be implemented to resolve the problems from metal contacts [141, 142].

11.2.3 Double Layer vs Single Layer

In the previous electric measurements (Chapter 10), we showed that charge transport behaviors through single- and double-layer pentacene OTFTs are different in terms of field-effect mobility and density of trap states. The different electronic properties is mainly ascribed to different localized states formed in the single- and double layer devices. Figure 11.4 shows the EFM measurement in the surface potential mode of a device whose channel is mostly covered with double-layer pentacene film (sample III). However, the contact from the upper electrode is only through the single layer, and the lower electrode is made on top of the double layer. The topological profile displayed in Fig. 11.4 (d) shows where the boundary between single and double layer is. The dotted line is used for a guide to eye.

In the previous measurements of sample II, the voltage drop at the source electrode is larger than that at the drain electrode. Interestingly, sample III shows that the voltage drop at the single-layer contact is consistently larger than that at the double-layer contact, even the single-layer contact is utilized as the drain electrode, as shown in Fig. 11.4 (c). The surface potential profile measured with biased single-layer contact (i.e., source electrode) is shown in Fig. 11.4 (b). When the upper electrode is biased at $V_{sd} = -5$ V, $\sim 45\%$ of voltage is dropped at the single-layer contact, and only $\sim 20\%$ is dropped at the double-layer contact. In reversed polarity, the single-layer contact is still responsible for the $\sim 40\%$ voltage

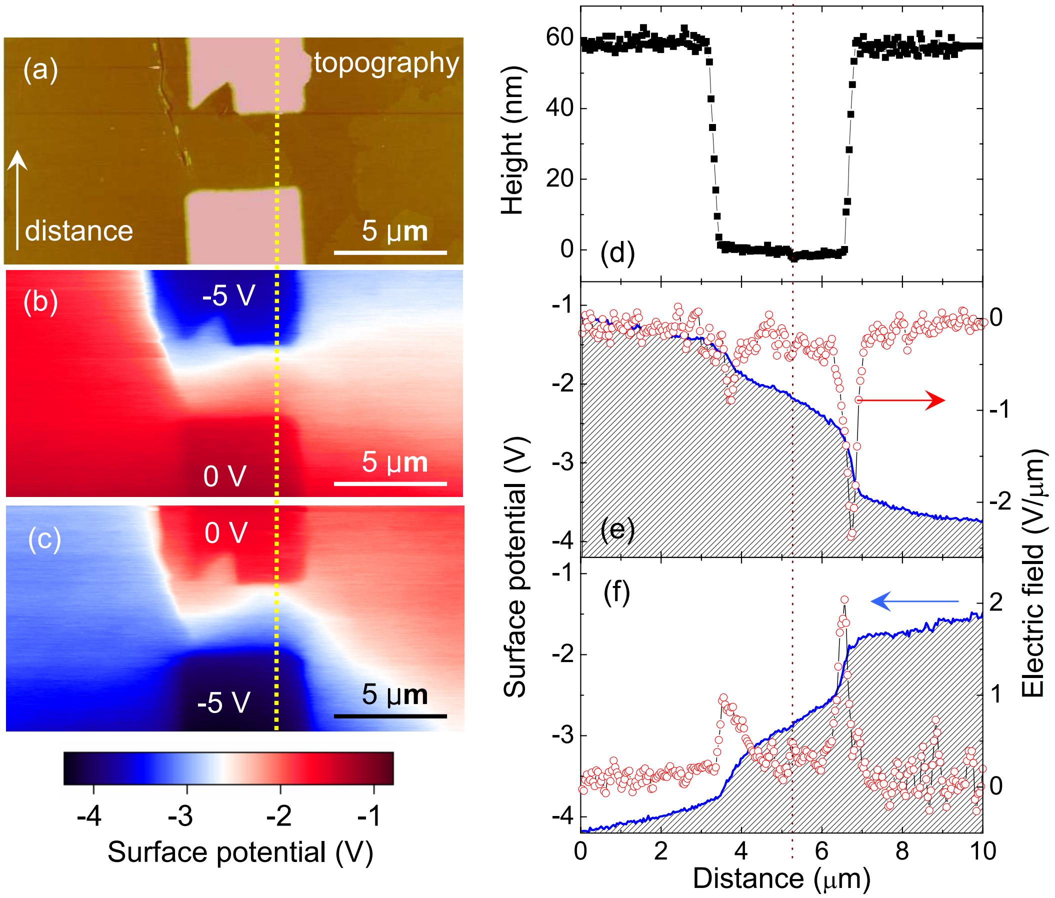

Figure 11.4: (a) Topological AFM image of the ultrathin layer device (sample III) whose majority of channel is covered with double-layer film. (b), (c) Surface potential images in biased at $V_\mathrm{b} = -5$ V at the top or bottom electrode, respectively. (d) Height profile scanned across the channel. Surface potential and calculated electric field profiles across the channel following the yellow dotted line biased at (e) upper electrode and (f) lower electrode, respectively.

drop even after it is changed to the drain, and $\sim 25\%$ of the voltage is dropped at the lower electrode. These contrasting observations between sample II and sample III suggest the different effects of metal contacts on the single- and double-layer pentacene films. During the metal electrode fabrication, it is easy to imagine that the conduction channel composed of the double-layer film is less affected by the metal contacts than single-layer film. Thus, the more localized states are expected at the single-layer contact, which may account for the observed larger voltage drop.

Figure 11.5 (a) shows the surface potential profile of sample II. Besides the voltage drops at the metal contacts, the surface potential monotonically decreases across the channel. The slope of the potential drop indicated by the red line shows a single slope, which can be attributed to the equally distributed localized states along the conducting channel. However, there exists two slopes when conduction channels are composed of single- and double-layer films (sample III), as shown in Fig. 11.5 (b). The slope from the single-layer coverage is measured to be ~ 2 times steeper than that from the double-layer film. Figure 11.5 (c) shows another data set from a single-layer device (sample IV) whose channel is also partially covered with double-layer film. The voltage drop along the conduction channel of sample IV also shows two slopes at the single- and double-layer film coverage, respectively. This observations suggest that charged carriers transport through the double-layer film easier than single layer, and this may be attributed to the different localized states formed in the single- and double-layer films due to the pentacene film interactions with gate insulator or ambient conditions.

11.3 Summary

In summary, the charge transport behaviors through single- and double-layer pentacene OTFTs are studied with EFM measurements. We have found that grain boundaries are the most dominant factors to limit charge transport. Metal contacts

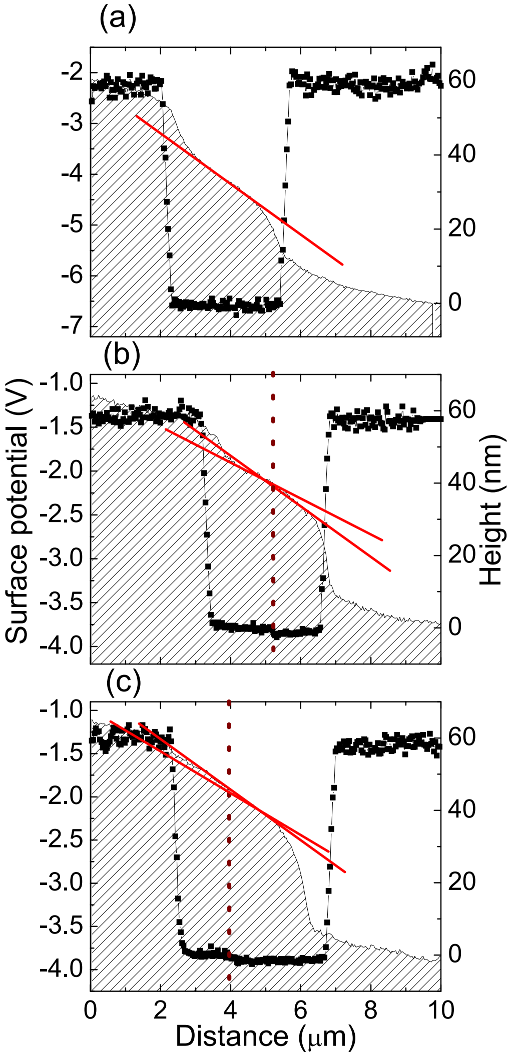

Figure 11.5: Surface potential profiles for devices comprised of (a) double-layer (sample II) only, and (b), (d) single and double-layer films (sample III, sample IV). The red lines represent the steepness of voltage drop across the channel.

are also responsible for the majority of localized states, and produce more trapped states at single-layer films than double layer.

Chapter 12

Summary and Conclusions

We have experimentally demonstrated spin transport through ferromagnet-contacted individual single-walled carbon nanotubes (SWCNTs), which exhibit several quantum transport behaviors at low temperature. The spin transport is observably correlated with its counterpart charge transport, and needs different frameworks to understand magnetoresistance (MR) features in varying from non-interacting Fabry-Perot interference regime to highly correlated Kondo and Coulomb blockade regimes.

In the Fabry-Perot (FP) interference regime, MR reveals the in-phase oscillatory behaviors to quantum interference modulations, accompanied by positive and negative MR sign change. MR is equally dependent on both gate and bias voltages, and observed MR features can be well understood by the double-channel mixing FP interference model in the condition of highly transparent metal contacts to SWCNTs. The double-channel mixing, introduced to reflect the intrinsic electronic structures of metallic SWCNTs has found to be essential for negative MR switchings observed in the FP interference regime.

Kondo effect is expected to be suppressed in the presence of spin-unbalanced ferromagnetic electrodes. However, it has been found that Kondo effect can still dominate charge transport through SWCNT quantum dots defined by ferromagnetic electrodes, under the condition of the strong Kondo effect and the weak ferromagnetism. Positive MR switching at zero-bias and in-phase MR evolution deep inside the Kondo ridges are explained by a Fermi liquid picture of the Kondo correlated state considering small electrode polarization and strong Kondo effect. The observed mirror symmetry in the mixed valence regime can be understood by the particle-hole symmetry.

We have observed several convincing evidences of magneto-Coulomb effects (MCE) in the Coulomb blockade regime in ferromagnet-contacted two-probe SWCNT devices. It has been found that the MCE is accountable for (i) large MR $\geq 100\%$ switching, (ii) absence of particle-hole symmetry across two- and four-fold Coulomb oscillations, (iii) single-step staircase switching, and (iv) the presence of MR switching in FM-SWCNT-NM devices.

Utilized with a four-probe non-local geometry, we can isolate the spin transport through a SWCNT QD exhibiting four-fold Coulomb oscillations from other secondary effects including anomalous magnetoresistance (AMR), spin-Hall effects, tunneling anisotropic magnetoresistance- like effects, and the MCE. The non-local spin signals show clear correlations with the Coulomb oscillations in the QD at low temperature, and becomes gate-voltage-independent when the Coulomb blockade effect is suppressed at high temperature.

In the second half of this thesis, we have discussed charge transport behaviors observed in ultrathin organic semiconductor pentacene field-effect transistors. The charged carrier mobilities form single- and double-layer pentacene film transistors increase as gate voltage increases, and decrease as temperature decreases. The gate-voltage and temperature-dependent mobilities are consistent with the multiple trapping and release model (MTR). The observed mobilities from double-layer devices are consistently higher than those from single-layer devices, which is further supported by different trap densities calculated from the MTR model. The field effect mobilities show saturation behavior as most trapped states are filled with induced charges, and the highest mobility from the single-layer device is measured up to ~ 0.5 cm^2/Vs. The effects of grain boundaries, metal contacts, and different number of pentacene layers on charge transports are studied with an electric force microscopy (EFM) technique, and they are consistent with the observations in the electric transport measurements.

Bibliography

[1] G. A. Prinz, Science **282**, 1660 (1998).

[2] P. L. McEuen, Phys. World **6**, 31 (2000).

[3] K. Tsukagoshi, B. W. Alphenaar, and H. Ago, Nature **401**, 572 (1999).

[4] S. Sahoo et al., Nature Phys. **2**, 99 (2005).

[5] A. Dodabalapur, L. Torsi, and H. E. Katz, Science **268**, 270 (1995).

[6] G. Horowitz, M. E. Hajlaoui, and R. Hajlaoui, J. Appl. Phys. **87**, 4456 (2000).

[7] S. Iijima, Nature **354**, 56 (1991).

[8] S. Iijima and T. Ichihashi, Nature **363**, 603 (1993).

[9] D. S. Bethune et al., Nature **363**, 605 (1993).

[10] A. Krishnan, E. Dujardin, T. W. Ebbesen, P. N. Yianilos, and M. M. J. Treacy, Phys. Rev. B **58**, 14013 (1998).

[11] C. T. White and J. W. Mintmire, Nature **394**, 29 (1998).

[12] M. Bockrath et al., Nature **397**, 598 (1999).

[13] Y. Saito et al., Nature **389**, 554 (1997).

[14] S. S. Wong, E. Joselevich, A. T. Woolley, C. L. Cheung, and C. M. Lieber, Nature **394**, 52 (1998).

[15] J. Kong et al., Science **287**, 622 (2000).

[16] J. Zhao, A. Buldum, J. Han, and J. Ping Lu, Phys. Rev. Lett. **85**, 1706 (2000).

[17] P. Kim and C. M. Lieber, Science **286**, 2148 (1999).

[18] S. J. Tans, A. R. M. Verschueren, and C. Dekker, Nature **393**, 49 (1998).

[19] S. J. Wind, J. Appenzeller, R. Martel, V. Derycke, and P. Avouris, Appl. Phys. Lett. **80**, 3817 (2002).

[20] C. Zhou, J. Kong, E. Yenilmez, and H. Dai, Science **290**, 1552 (2000).

[21] J. Kong, J. Cao, H. Dai, and E. Anderson, Appl. Phys. Lett. **80**, 73 (2002).

[22] Z. Yao, H. W. C. Postma, L. Balents, and C. Dekker, Nature **402**, 273 (1999).

[23] M. S. Dresselhaus, G. Dresselhaus, and P. Avouris, *Carbon Nanotubes: Synthesis, Structure, Properties, and Applications*, Springer, New York, 2001.

[24] R. Saito, M. Fujita, G. Dresselhaus, and M. S. Dresselhaus, Appl. Phys. Lett. **60**, 2204 (1992).

[25] N. Hamada, S.-i. Sawada, and A. Oshiyama, Phys. Rev. Lett. **68**, 1579 (1992).

[26] S. J. Tans et al., Nature **386**, 474 (1997).

[27] W. J. Liang et al., Nature **411**, 665 (2001).

[28] J. Nygard, D. H. Cobden, and P. E. Lindelof, Nature **408**, 342 (2000).

[29] H. T. Man and A. F. Morpurgo, Phys. Rev. Lett. **95**, 026801 (2005).

[30] W. G. van der Wiel et al., Science **289**, 2105 (2000).

[31] D. Goldhaber-Gordon et al., Phys. Rev. Lett. **81**, 5225 (1998).

[32] M.-S. Choi, D. Sánchez, and R. López, Phys. Rev. Lett. **92**, 056601 (2004).

[33] J. Martinek et al., Phys. Rev. Lett. **91**, 247202 (2003).

[34] J. Martinek et al., Phys. Rev. Lett. **91**, 127203 (2003).

[35] B. E. A. Saleh and M. C. Teich, *Fundamentals of Photonics*, Jone Wiley and Sons Inc, 1991.

[36] H. I. Jorgensen, K. Grove-Rasmussen, T. Novotny, K. Flensberg, and P. E. Lindelof, Phys. Rev. Lett. **96**, 207003 (2006).

[37] H. T. Man, I. J. W. Wever, and A. F. Morpurgo, Phys. Rev. B **73**, 241401 (2006).

[38] R. Meservey, P. M. Tedrow, and P. Fulde, Phys. Rev. Lett. **25**, 1270 (1970).

[39] P. M. Tedrow and R. Meservey, Phys. Rev. Lett. **26**, 192 (1971).

[40] J. Soulen, R. J. et al., Science **282**, 85 (1998).

[41] M. Ziese, Rep. Prog. Phys. **65**, 143 (2002).

[42] A. E. Berkowitz and K. Takano, J. Magn. Magn. Mat. **200**, 552 (1999).

[43] F. J. Jedema, A. T. Filip, and B. J. van Wees, Nature **410**, 345 (2001).

[44] M. Julliere, Phys. Lett. A **54**, 225 (1975).

[45] J. S. Moodera, L. R. Kinder, T. M. Wong, and R. Meservey, Phys. Rev. Lett. **74**, 3273 (1995).

[46] S. Datta and B. Das, Appl. Phys. Lett. **56**, 665 (1990).

[47] E. I. Rashba, Sov. Phys. Solid State **2**, 1109 (1960).

[48] A. Cottet, T. Kontos, W. Belzig, C. Schonenberger, and C. Bruder, Eur. Phys. Lett. **74**, 320 (2006).

[49] C. T. White and T. N. Todorov, Nature **393**, 240 (1998).

[50] B. Zhao, I. Monch, T. Muhl, H. Vinzelberg, and C. M. Schneider, J. Appl. Phys. **91**, 7026 (2002).

[51] S. Sahoo, T. Kontos, C. Schonenberger, and C. Surgers, Appl. Phys. Lett. **86**, 112109 (2005).

[52] L. E. Hueso et al., Nature **445**, 410 (2007).

[53] J.-R. Kim, H. M. So, J.-J. Kim, and J. Kim, Phys. Rev. B **66**, 233401 (2002).

[54] A. Jensen, J. R. Hauptmann, J. Nygrd, and P. E. Lindelof, Phys. Rev. B **72**, 035419 (2005).

[55] B. Nagabhirava, T. Bansal, G. U. Sumanasekera, B. W. Alphenaar, and L. Liu, Appl. Phys. Lett. **88**, 023503 (2006).

[56] C. Schonenberger, Observation of an oscillating magnetoresistance with gate voltage in carbon-nanotube based tmr devices, Technical report, Spintronics, Kavil Institue for Theoretical Phyics, UCSB, 2006.

[57] N. Tombros, S. J. van der Molen, and B. J. van Wees, Phys. Rev. B **73**, 233403 (2006).

[58] S. J. van der Molen, N. Tombros, and B. J. van Wees, Phys. Rev. B **73**, 220406 (2006).

[59] D. D. Awschalom and M. E. Flatte, Nature Phys. **3**, 153 (2007).

[60] C. Gould et al., Phys. Rev. Lett. **93**, 117203 (2004).

[61] L. Balents and R. Egger, Phys. Rev. Lett. **85**, 3464 (2000).

[62] L. Balents and R. Egger, Phys. Rev. B **6403**, 035310 (2001).

[63] J. Kong, H. T. Soh, A. M. Cassell, C. F. Quate, and H. Dai, Nature **395**, 878 (1998).

[64] S. Wolf and R. N. Tauber, *Silicon Processing for the VLSI Era*, Lattice, Sunset Beach, CA, 1986.

[65] B. Zheng et al., Nano Lett. **2**, 895 (2002).

[66] S. Datta, *Electronic Transport in Mesoscopic Systems*, Cambridge University Press, Cambridge, United Kingdom, 1995.

[67] A. T. Hindmarch, C. H. Marrows, and B. J. Hickey, Phys. Rev. B **72**, 060406 (2005).

[68] A. T. Hindmarch, C. H. Marrows, and B. J. Hickey, Phys. Rev. B **72**, 100401 (2005).

[69] A. N. Pasupathy et al., Science **306**, 86 (2004), J. Nygard, W. Koehl, N. Mason, L. DiCarlo, and C. Marcus, cond-mat/0410467 (unpublished).

[70] A. C. Hewson, *The Kondo Problem to Heavy Fermions*, Cambridge University Press, Cambridge, 1993.

[71] L. Kouwenhoven and L. Glazman, Phys.World **14**, 33 (2001).

[72] A. Cottet et al., Semicond. Sci. Technol. **21**, S78 (2006).

[73] A. Cottet and M.-S. Choi, Phys. Rev. B **74**, 235316 (2006).

[74] S. Braig and P. W. Brouwer, Phys. Rev. B **71**, 195324 (2005).

[75] F. D. M. Haldane, Phys. Rev. Lett. **40**, 416 (1978), Erratum: *ibid*, 911 (1978).

[76] T. A. Costi, A. C. Hewson, and V. Zlatic, J. Phys.: Condens. Matter **6**, 2519 (1994).

[77] K. Ono, H. Shimada, and Y. Ootuka, J. Phys. Soc. Jpn. **66**, 1261 (1997).

[78] K. Ono, H. Shimada, and Y. Ootuka, J. Phys. Soc. Jpn. **67**, 2852 (1998).

[79] M. M. Deshmukh et al., Phys. Rev. Lett. **87**, 226801 (2001).

[80] L. W. Liu et al., Phys. Rev. B **74**, 245429 (2006).

[81] H. Shimada, K. Ono, and Y. Ootuka, J. Phys. Soc. Jpn. **67**, 1359 (1998).

[82] I. Zutic, J. Fabian, and S. Das Sarma, Rev. Mod. Phys. **76**, 323 (2004).

[83] S. Takahashi and S. Maekawa, Phys. Rev. Lett. **80**, 1758 (1998).

[84] W. J. Liang, M. Bockrath, and H. Park, Phys. Rev. Lett. **88**, 126801 (2002).

[85] B. Babic, T. Kontos, and C. Schonenberger, Phys. Rev. B **70**, 235419 (2004).

[86] Y. Oreg, K. Byczuk, and B. I. Halperin, Phys. Rev. Lett. **85**, 365 (2000).

[87] H. Shimada and Y. Ootuka, Phys. Rev. B **64**, 235418 (2001).

[88] M. N. Baibich et al., Phys. Rev. Lett. **61**, 2472 (1988).

[89] F. J. Jedema, H. B. Heersche, A. T. Filip, J. J. A. Baselmans, and B. J. van Wees, Nature **416**, 713 (2002).

[90] X. Lou et al., Nature Phys. **3**, 197 (2007).

[91] M. Johnson and R. H. Silsbee, Phys. Rev. Lett. **55**, 1790 (1985).

[92] S. A. Crooker et al., Science **309**, 2191 (2005).

[93] A. Javey, J. Guo, Q. Wang, M. Lundstrom, and H. Dai, Nature **424**, 654 (2003).

[94] D. Voss, Nature **407**, 442 (2000).

[95] C. D. Dimitrakopoulos and D. J. Mascaro, IBM Jour. Res. Dev. **45**, 11 (2001).

[96] R. Wisnieff, Nature **394**, 225 (1998).

[97] K. M. Vaeth and J. Dicillo, J. Poly. Sci. B **41**, 2715 (2003).

[98] M. Granstrom et al., Nature **395**, 257 (1998).

[99] P. Peumans, S. Uchida, and S. R. Forrest, Nature **425**, 158 (2003).

[100] M. S. Shur, S. L. Rumyantsev, and R. Gaska, Int. J. High Speed Elec. Sys. **12**, 371 (2002).

[101] G. H. Gelinck et al., Nature Mat. **3**, 106 (2004).

[102] B. Crone et al., Appl. Phys. Lett. **78**, 2229 (2001).

[103] W. Clemens, W. Fix, J. Ficker, A. Knobloch, and A. Ullmann, J. Mat. Res. **19**, 1963 (2004).

[104] P. Andersson et al., Adv. Mat. **14**, 1460 (2002).

[105] G. W. Neudeck and A. K. Malhotra, Sol. Stat. Elec. **19**, 721 (1976).

[106] D. J. Gundlach, J. A. Nichols, L. Zhou, and T. N. Jackson, Appl. Phys. Lett. **80**, 2925 (2002).

[107] A. L. Briseno et al., Adv. Mat. **18**, 2320 (2006).

[108] V. Podzorov, S. E. Sysoev, E. Loginova, V. M. Pudalov, and M. E. Gershenson, Appl. Phys. Lett. **83**, 3504 (2003).

[109] P. V. Necliudov, M. S. Shur, D. J. Gundlach, and T. N. Jackson, J. Appl. Phys. **88**, 6594 (2000).

[110] A. B. Chwang and C. D. Frisbie, J. Appl. Phys. **90**, 1342 (2001).

[111] Z. T. Zhu, J. T. Mason, R. Dieckmann, and G. G. Malliaras, Appl. Phys. Lett. **81**, 4643 (2002).

[112] D. J. Wold and C. D. Frisbie, J. Am. Chem. Soc. **122**, 2970 (2000).

[113] B. Stadlober et al., Appl. Phys. Lett. **86**, 242902 (2005).

[114] G. Horowitz, Adv. Mat. **10**, 365 (1998).

[115] A. Tsumura, H. Koezuka, and T. Ando, Appl. Phys. Lett. **49**, 1210 (1986).

[116] D. Knipp, R. A. Street, and A. R. Volkel, Appl. Phys. Lett. **82**, 3907 (2003).

[117] S. Y. Jung and Z. Yao, Appl. Phys. Lett. **86**, 083505 (2005).

[118] K. C. Dickey, J. E. Anthony, and Y. L. Loo, Adv. Mat. **18**, 1721 (2006).

[119] C. Kim, P. E. Burrows, and S. R. Forrest, Science **288**, 831 (2000).

[120] C. D. Dimitrakopoulos and P. R. L. Malenfant, Adv. Mat. **14**, 99 (2002).

[121] S. M. Sze, *Physics of Semiconductor Devices*, New York, 1981.

[122] M. E. Gershenson, V. Podzorov, and A. F. Morpurgo, Rev. Mod. Phys. **78**, 973 (2006).

[123] D. B. Thomasson and T. N. Jackson, IEEE Elec. Dev. Lett. **18**, 397 (1997).

[124] B. Servet et al., Chem. Mater. **6**, 1809 (1994).

[125] G. Horowitz and M. E. Hajlaoui, Syn. Met. **122**, 185 (2001).

[126] G. Horowitz, Adv. Mat. **2**, 287 (1990).

[127] R. W. I. de Boer, M. E. Gershenson, A. F. Morpurgo, and V. Podzorov, Phy. Stat. Sol. A **201**, 1302 (2004).

[128] E. L. Granstrom and C. D. Frisbie, J. Phy. Chem B **103**, 8842 (1999).

[129] F. Dinelli et al., Phys. Rev. Lett. **92**, 116802 (2004).

[130] S. E. Fritz, S. M. Martin, C. D. Frisbie, M. D. Ward, and M. F. Toney, J. Am. Chem. Soc. **126**, 4084 (2004).

[131] C. D. Dimitrakopoulos, S. Purushothaman, J. Kymissis, A. Callegari, and J. M. Shaw, Science **283**, 822 (1999).

[132] Y. Y. Lin, D. J. Gundlach, S. F. Nelson, and T. N. Jackson, IEEE Elec. Dev. Lett. **18**, 606 (1997).

[133] M. Shur and M. Hack, J. Appl. Phys. **55**, 3831 (1984).

[134] M. Shur, M. Hack, and J. G. Shaw, J. Appl. Phys. **66**, 3371 (1989).

[135] P. G. Le Comber and W. E. Spear, Phys. Rev. Lett. **25**, 509 (1970).

[136] G. Horowitz, R. Hajlaoui, and P. Delannoy, J. Phy. III **5**, 355 (1995).

[137] F. D. Angelis, S. Cipolloni, L. Mariucci, and G. Fortunato, Appl. Phys. Lett. **86**, 203505 (2005).

[138] A. Facchetti, M. H. Yoon, and T. J. Marks, Adv. Mat. **17**, 1705 (2005).

[139] S. Y. Yang, S. H. Kim, K. Shin, H. Jeon, and C. E. Park, Appl. Phys. Lett. **88**, 173507 (2006).

[140] K. P. Puntambekar, P. V. Pesavento, and C. D. Frisbie, Appl. Phys. Lett. **83**, 5539 (2003).

[141] Y. L. Loo et al., Proc. Natl. Acad. Sci. U.S.A. **99**, 10252 (2002).

[142] Y. L. Loo, R. L. Willett, K. W. Baldwin, and J. A. Rogers, Appl. Phys. Lett. **81**, 562 (2002).

Vita

Suyong Jung was born in Anyang, Gyunggi, Republic of Korea on May 23, 1976, as the first son of Sang-Yeol Jung and Sang-Im Kim. After spending his whole childhood in Anyang, he went to the Seoul National University in Korea to follow his early dream to be a scientist in 1994. There he spent the most exciting and energetic two years in his life while in participating at several activities, which were dedicated to maintain and succeed the traditional Korean folk music, 'PungMul'. After fulfilling the 26-month mandatory military service as the special agent in cryptography, he went back to school to finish his degree. He graduated with a B.S. while majoring in Physics in the late February, 2001, and entered the Graduate School at the University of Texas at Austin in August 2001 to pursue the Ph. D. He is expected to finish his graduate studies in the summer of 2007 after spending five years under the supervision of Prof. Zhen Yao.

Permanent Address: 1408 Gwangmyung Bd. 401 Gwanyang 1-dong
Dongan-gu, Anyang, Gyunggi 431-061
Korea (Republic of)

This dissertation was typeset with LaTeX 2_ε[1] by the author.

---

[1] LaTeX 2_ε is an extension of LaTeX. LaTeX is a collection of macros for TeX. TeX is a trademark of the American Mathematical Society. The macros used in formatting this dissertation were written by Dinesh Das, Department of Computer Sciences, The University of Texas at Austin, and extended by Bert Kay, James A. Bednar, and Ayman El-Khashab.